UNIVERSITAT ROVIRA I VIRGILI

LAYERED DOUBLE HYDROXIDES FOR APPLICATIONS IN CATALYSIS AND ELECTROLUMINESCENT DEVICES.

Elena Pérez Barrado

Dipòsit Legal: T 276-2015

Elena Pérez Barrado

LAYERED DOUBLE HYDROXIDES FOR APPLICATIONS IN CATALYSIS AND ELECTROLUMINESCENT DEVICES

Doctoral thesis

Supervised by

Dr. Lluís F. Marsal Garví
Dr. Maria Cinta Pujol Baiges
Dr. Pilar Salagre Carnero

Department of Physical and Inorganic Chemistry

Engineering of Materials and Micro/Nanosystems (EMaS)

UNIVERSITAT ROVIRA I VIRGILI

Tarragona

2015

UNIVERSITAT ROVIRA I VIRGILI

I STATE that the present study, entitled **"Layered double hydroxides for applications in catalysis and electroluminescent devices"**, presented by Elena Pérez Barrado for the award of the degree of Doctor, has been carried out under my supervision at the Department of Physical and Inorganic Chemistry of this university, and that it fulfils all the requirements to be eligible for the European Doctor distinction award.

Tarragona, 24th November 2014

Doctoral Thesis Supervisors

Dr. Lluís F. Marsal Garbí

Dr. Maria Cinta Pujol Baiges

Dr. Pilar Salagre Carnero

Acknowledgements

I would like to express my deepest gratitude to my PhD supervisors, Prof. Lluís Marsal, Dr. Cinta Pujol and Dr. Pilar Salagre for their guidance, knowledge, advices, caring and patience through the thesis period. I feel that there's been an excellent atmosphere during this time.
I would also like to acknowledge Prof. Magdalena Aguiló, Prof. Yolanda Cesteros, Prof. Francesc Díaz and Prof. Josep Pallarès for their guidance and help.

My sincere thanks also go to the staff at *Servei de Recursos Científics* of the university, especially Dr. Francesc Gispert, Dr. Rita Marimon, Dr. Mariana Stefanova, Mrs. Mercè Moncusí, Dr. Lukas Vojkuvka and Mr. Antonio de la Torre.

This work has been developed in three research groups: *Greencat*, *Ficma-Ficna* and *Nephos*. Working in three different groups can be challenging at times, since each group has a different organization of their work. Since my *basement* was located at the *Greencat* facilities for most of the thesis time, I would like to especially acknowledge Dr. Pilar Formentín, Dr. Maria Méndez, Mrs. María Alba and Dr. Josep Ferré (from *Nephos*) and Mr. Agustí Montero, Mrs. Laura Escorihuela, Mrs. Nicolette Baker, Dr. E. William Barrera and Dr. M. Usman Qadri (from *Ficma-Ficna*) for their great help, advice and eagerness to teach me how to use the different instrumentation located at those facilities. Special thanks to Mr. Peilin Han for performing cathode deposition on my devices and to Mrs. Pinkie Jacob for her advices.

Also, many thanks to doctors Tatiana Sánchez, Dolores González, Isabel Sánchez, Xavier Cardó and Mrs. Susana Domínguez for their help and advice at the *Greencat* facilities. Sincere thanks to Mrs. Raquel Rivas for her help and useful advices.

I would like to thank to all former and present staff members of *Greencat*, *Ficma-Ficna* and *Nephos* groups.

My gratitude goes to Dr. Isabel Parreu, from Emas Research Center.

I would like to thank the staff of *Catheter* group, especially for all those moments when I needed a reagent, laboratory glassware or a piece of advice.

I would also like to thank Universitat Rovira i Virgili and Emas Research Center for the PhD grant.

Desidero ringraziare il Prof. Leonardo Marchese per gli insegnamenti ricevuti, per l'aiuto e la disponibilità datami. Inoltre, ringrazio il Dr. Fabio Cucinotta per il suo costante aiuto, e per le sue brillanti idee che sempre mi ha trasmesso. Vorrei anche ringraziare la Dr.ssa Chiara Bisio, il Dr. Giorgio Gatti, il Dr. Gianluca Croce, e anche il Dr. Nello Li Pira, del Centro da Ricerca Fiat, Orbassano, Torino. In questo soggiorno Italiano ci sono state persone che mi hanno fatto vivere una grande esperienza, non solo in laboratorio ma anche al di fuori. Ai colleghi del ufficio: Fabio, Alberto, Ilaria B. e Ilaria Z… Alle belle conversazione avute con Valentina e per il tempo compartito con Antonio e Dayane. Ciascuno di loro ha contribuito a far si che fosse una bella esperienza.

Quisiera agradecer a mis padres y a toda mi familia por su apoyo durante este periodo y por todo. A mi hermano Pablo y a Gemma, que además me han regalado unos bonitos sobrinos. También quisiera acordarme de mis abuelos, por su ternura y por las valiosas lecciones que he aprendido de ellos. Sin duda, los abuelos son de las mejores cositas de este mundo. Ik zou graag mijn kleine Boerma willen bedanken voor alles, bovenal voor het deel uitmaken van mijn leven. Ook wil ik de Boerma's en de Darwinkel's bedanken voor de hechte en aardige familie die jullie voor mij betekenen. Ten slotte wil ik onze vrienden bedanken voor alle mooie momenten die wij samen hebben meegemaakt.

A mis amistades por tantos años de momentos compartidos y por los momentos que quedan por compartir. Especialmente a mis niñas de *Escolàpies* por toda una vida de amistad. A los amigos de la uni. A Sílvia e Inma por tantas cosas maravillosas y por ser como familia pero sin el cómo. A Sandra, l'amiga viatgera que tothom necessita. A Natalia por las risas. A mis nenes del *Erasmus* porque me demuestran siempre que las distancias no existen.

Cambiar las calles del *Clot* y el *Poblenou* por las de la *Part Alta* ha sido una gran aventura gracias a las personas con las que he compartido este tiempo en Tarragona. He vivido con una muy buena representación de las dos Castillas durante gran parte del doctorado, Luís y María, con los que además he compartido innumerables momentos. Momentos en los que nos han acompañado Susana, Raquel, Tatiana, Álex, Dolores, Isa, Adriana, Marta, Óscar, Dragos, Dana, Vero, Ana, Maria, Caterina y Carla. Gracias también a Fish, Judith y Bea.

¡Y gracias también a las patatas *meneás* y a los piononos!

Si la rutina te aplasta,
dile que ya basta
de mediocridad.
Hoy puede ser un gran día
date una oportunidad.

Joan Manuel Serrat,
lyrics from *Hoy puede ser un gran día.*

To my grandparents Juan Manuel and Manuela

Table of Contents

Table of Contents

CHAPTER 1

Introduction

1. Introduction.

The motivation of this thesis is the application of layered double hydroxides (LDHs) in the fields of heterogeneous catalysis, hybrid materials synthesis and light-emitting diodes. The catalytic reaction studied in this work is the etherification of glycerol towards low-chain polyglycerols using calcined layered double hydroxides. When layered double hydroxides are delaminated, the positively charged nanoplatellets can be used for composite & hybrid materials purposes. Finally, in delaminated form they can embed thiol-capped CdTe nanoparticles and form the emissive layer for light-emitting diodes.

The topics covered in this Introduction chapter are:

- Layered double hydroxides (LDHs).
- Glycerol and its revalorization reactions.
- Quantum dots nanoparticles.
- LED devices.

1.1 Layered double hydroxides (LDHs).

1.1.1 Hydrotalcite- and hydrocalumite-like compounds (HTlcs and HClcs).

Hydrotalcite-like compounds, also named layered double hydroxides, have general formula $(M^{2+}_{1-x}M^{3+}_{x}(OH)_2)^{x+}(A^{m-}_{1/m})\cdot nH_2O$, where the divalent cation, M^{2+}, may be Mg^{2+}, Ca^{2+}, Zn^{2+} or Ni^{2+} and the trivalent cation, M^{3+}, Al^{3+}, Fe^{3+}, Cr^{3+}, …, and the compensation anions, OH^-, Cl^-, NO^-_3, SO^{2-}_4 and *x* can take, preferentially, values between 0,25 and 0,33. It is an alternating layered structure with positively charged brucite-like layers $(M^{2+}_{1-x}M^{3+}_{x}(OH)_2)^{x+}$ where M^{2+} cations are substituted by M^{3+} cations, and interlayers containing the charge-balancing anions and water molecules [Miyata 1975, Tichit *et al.* 1995].

Layered double hydroxides can be found in nature or synthesized in laboratory facilities. As a mineral, it was first discovered in Sweden around 1842. The first patent for a hydrotalcite-like compound was registered in 1970 [Brocker *et al.* 1970]. The formula for the most representative sample, called hydrotalcite, is $[Mg_6Al_2(OH)_{16}CO_3\cdot 4H_2O]$ [Manasse 1915].

For the particular case when the divalent metal is Ca^{2+}, a hydrocalumite subgroup arises from the layered double hydroxide family of materials. The most representative mineral is hydrocalumite, also called Friedel's salt, and has the following composition: $[Ca_2Al(OH)_6]Cl\cdot 2H_2O$ [Vieille *et al.* 2003]. As like HTlcs (hydrotalcite-like compounds), the composition of hydrocalumite-like compounds can be tuned regarding the trivalent metal and the anion. In the industry of cement these are well known materials and are also called AFm phases of cement [Taylor 1997]. The general formula for hydrocalumite-like compounds is $[Ca_2M^{3+}(OH)_6]^+[A^{n-}_{1/n}\cdot mH_2O]^-$.

Layered double hydroxides are also called anionic clays. Possible applications of LDHs are [Cavani *et al.* 1991]:

- catalysts: hydrogenation, polymerization, steam reforming…
- catalyst supports.
- Industry: flame retardant, molecular sieve, ion exchangers…
- Medicine: antiacid, antipeptin, stabilizer…
- Adsorbent: halogen scavenger, PVC stabilizer, wastewaters…

The applications in the field of medicine has increased the attention of researchers in the last years, because of the cost of anionic clays and the non-toxicity for humans. Some applications include the treatment of illnesses and drug-delivery [Choy *et al.* 2007, Del Hoyo 2007].

1.1.2 Calcined layered double hydroxides. Applications.

After the calcination of the layered double hydroxide, a mixture of oxides are obtained. Some of their properties are [Cavani *et al*. 1991]:

- high surface area.
- basic properties.
- small crystallite sizes, stable to thermal treatments which can be reduced to thermally stable metal crystallites.
- they have memory effect, which allows the reconstruction, under mild conditions, of the original layered double hydroxide structure when contacting the product of the thermal treatment with water solutions containing various anions.

Because of these properties they have many applications as heterogeneous catalysts and as ion absorbents for water purification [Hattori 1995, Tichit *et al.* 2003].

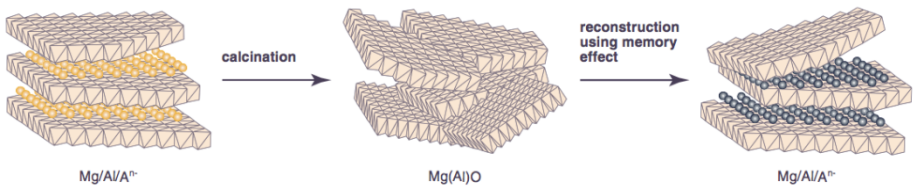

Figure 1.1 Simplified representation of calcination and reconstruction process [Tichit *et al.* 2003].

Figure 1.1 shows a simplified representation of the structure for a hydrotalcite-like compound, the calcination and the reconstruction process.

1.1.3 Delamination of layered double hydroxides.

Delamination of layered double hydroxides leads to the obtention of positively charged nanosheets [Ma *et al*. 2010].

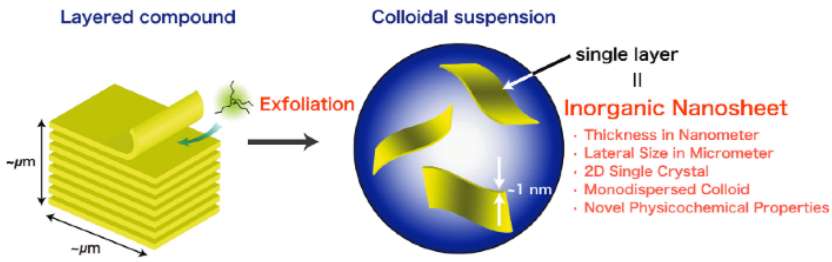

Figure 1.2 Schematic representation of the single nanoplatellets obtained after delamination [Wang *et al*. 2012].

These platelets or nanosheets can have direct applications and be an intermediate step to the intercalation of guests molecules or compounds in the interlayer region and obtain the layered structure. These nanoplatelets, also referred as (two-dimensional) 2D materials, can be used for electronic, photonic, mechanical and magnetic materials [Wang *et al.* 2012]. The thickness (around 1 nm) and the lateral size (from nanometers to micrometers) allows them to be used in quantum systems and as building blocks in the synthesis of functional solids [Ma *et al.* 2010]. The representation of the single nanoplatellets are shown in figure 1.2. The obtained thin platelets can be used as nanocomposites for polymers and for organic-inorganic or inorganic-inorganic nanomaterials [Qiu *et al.* 2005, Wu *et al*. 2005].

1.2 The glycerol challenge: transforming an inexpensive sub-product into attractive valued-added compounds.

1.2.1 Fossil fuels and biodiesel.

Traditional energy sources such as human power, wood, flowing water and wind were revolutionary changed about 300 years ago when stationary wind-power and water-technologies arose. Later on, they were replaced by fossil hydrocarbons: coal (XIX century), oil (XX century) and natural gas (with a remarkable increase in the last years) [Hall *et al*. 2003]. The reservoirs of fossil fuels are decreasing worldwide. The scarcity of petroleum reserves makes renewable energy sources necessary [Demirbas 2009].

Biodiesel is made from renewable biological sources like vegetable oils, animals fats and other sources, like microalgae [Ma et al. 1999, Dresselhaus *et al*. 2001, Wijffels *et al*. 2010]. In the early 30s and 40s of the XX century, vegetable oils were used as diesel fuels in emergency

situations. More recently, because the price of crude oil, the limitation of the reservoirs and the rising concern about environmental protection (especially global warming caused by CO_2 emissions) have turned the attention to biodiesel production [Ma *et al*. 1999].

Transesterification is usually the preferred route to obtain biodiesel. Biodiesel is a mono alkyl ester of long chain fatty acids that can be prepared from acyl-glycerol (usually triglyceride) in vegetable oils via transesterification with short chain alcohols. It gives glycerol as by-product. The typical feedstock to start the reaction divides into lipid feedstock and alcohol feedstock. Commonly used lipid feedstock are vegetable oils (from rapessed, soybean, sunflower seeds, palm, copra, peanut…) [Issariyakul *et al*. 2014].

1.2.2 Glycerol production.

The use and demand of biodiesel is growing exponentially. Figure 1.3 shows a graph with the world biodiesel production in the 2-decade period from 1991-2011 [García *et al*. 2014].

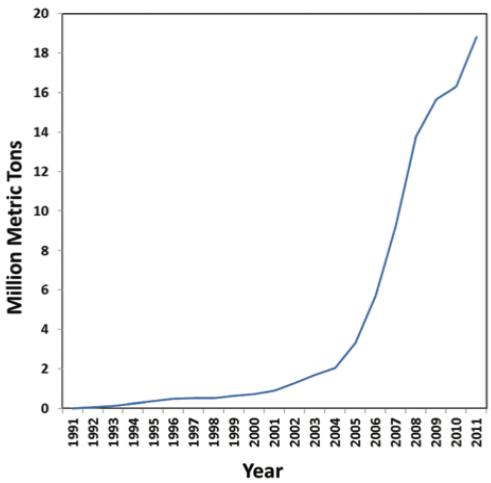

Figure 1.3 World biodiesel production, 1991-2011 [García *et al*. 2014].

Glycerol is produced as 10 wt% of the total biodiesel as by-product. Quantitatively, more than 2 t in the last years were produced of glycerol. The quantity that comes from biodiesel is more than 2/3 of the total outcome. Economically, the impact is non-negligible. This surplus means that prices of crude glycerol are decreasing. The same tendency occurs with glycerol used for pharmaceutical uses (called pharma glycerol, of 99,5% minimum purity) [García *et al*. 2014].

Glycerol has applications in different divisions of the industry, such as pharmaceutical, food, personal care, obtention of polyethers… [Pagliaro *et al*. 2007]. Figure 1.4 shows the applications of glycerol.

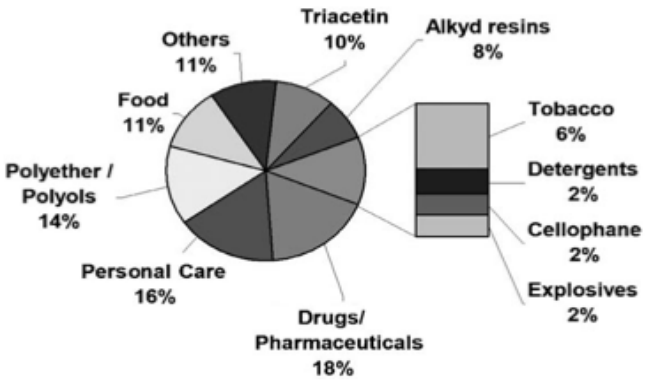

Figure 1.4 Applications of glycerol [Pagliaro *et al*. 2007].

Industrial plants are being closed in the last years because of the reduced price for glycerol. Because of this, several routes are being researched to transform glycerol into value-added products. This revalorization reactions are explained in the next section.

1.2.3 Glycerol revalorization reactions.

Glycerol is a highly functionalized molecule. Some transformations of glycerol, obtained from biomass, leads to products that were initially obtained from petroleum derivatives, such as glycidol and epichlorohydrin. Scheme 1.1 shows routes that can be obtained from petroleum and biomass for these two key compounds, glycidol and epichlorohydrin.

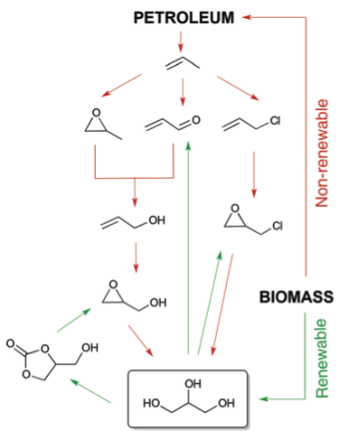

Scheme 1.1 Petroleum vs. biomass routes for the obtention of key compounds [García *et al*. 2014].

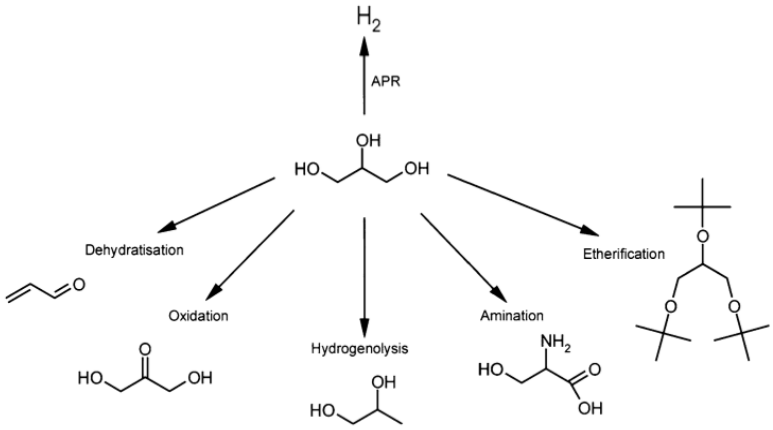

Scheme 1.2 Some transformations of glycerol into value-added products [Brandner *et al*. 2009].

Some of the main reactions that start from the use of glycerol are summarized in Scheme 1.2. Glycerol monoesters can be prepared by esterification of glycerol with carboxylic acids as well as by transesterification with their methyl esters. Glycerol carbonate is obtained by a multi-step process: first, ethylene oxide reacts with carbon dioxide to yield cyclic ethylene carbonate with then, reacts with glycerol to yield glycerol carbonate and ethylene glycol. Direct synthesis with CO_2 is a preferred path that is being studied. Glycerol alkyl ethers can be obtained by the condensation reaction between glycerol and an aliphatic alcohol under elimination of water.
Obtention of ketals or acetals can be done by reaction of glycerol with various aldehydes or ketones yielding five or six-membered cycles. The production of 1,2-propanediol can be done by direct hydrogenation of glycerol with high selectivity. Epoxides can be obtained by glycerol chlorination and further formation of the epoxide by the addition of sodium hydroxide. Obtention of polyglycerols by etherification is directly achieved with the appropriate catalyst. The scheme of this reaction is shown in Scheme 1.3.

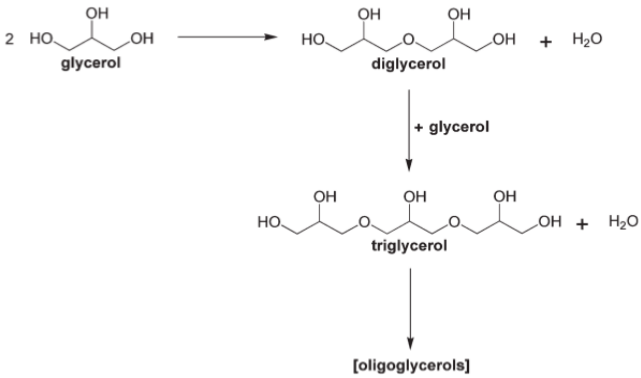

Scheme 1.3 Etherification of glycerol to polyglycerols [Behr *et al.* 2008].

Several reviews have been published in the last years explaining in depth the main reactions starting from glycerol that yield value-added compounds [Karinen *et al.* 2006, Pagliaro *et al.* 2007, Behr *et al*. 2008, Serrano-Ruiz *et al.* 2011, Zhou *et al.* 2013, Climent *et al.* 2014, Mizugaki *et al.* 2014]. In this thesis, we are interested in the transformation of glycerol to short-chain polyglycerols [Chapter 5].

1.3 Quantum dots (QDs).

In the 80s (XX century) scientists realized that at nanometer length scales, the color of semiconductor particles depended on their physical size. The concept of quantum confinement arose theoretically and experimentally. Quantum confinement in QDs gives rise to discrete electron and hole states that can be precisely tuned by varying the particle size of the semiconductor [Talapin *et al*. 2013].

Quantum dots comprise a small inorganic semiconductor core (1–10 nm in diameter), often a wider-bandgap inorganic semiconductor shell, and a coating of organic passivating ligands. The synthesis, usually involves pyrolysis of organometallic precursors injected into a hot organic coordinating solvent at temperatures of 393-633 K [Shirasaki *et al.* 2013]. Figure 1.5 shows colloidal solutions of different particle sizes (color-size properties).

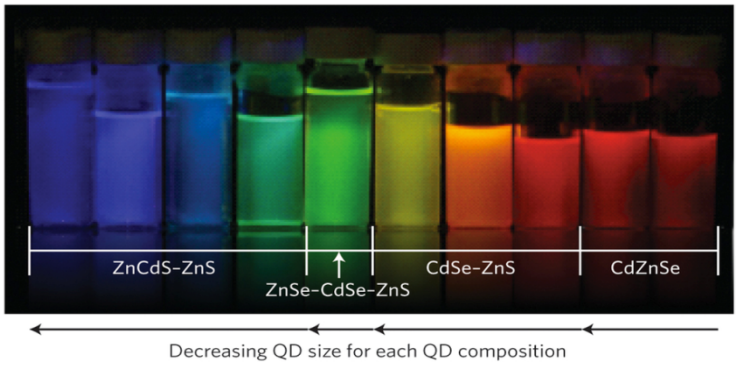

Figure 1.5 Colloidal solutions of QDS of different particle sizes [Anikeeva *et al*. 2009].

The size of the QDs can be controlled then by synthesis temperature and time. The synthesis procedures for some QDs are reviewed elsewhere [Peng *et al*. 2000, Gaponik *et al*. 2002, Burda *et al*. 2005, Wang *et al.* 2005, Das *et al*. 2009, Bimberg *et al*. 2011]. Usually they are composed of II-VI group or III-V group elements.

QDs have applications in different fields: optoelectronics, medicine, photovoltaic devices, image and sensing, telecommunications… [Gaponik *et al*. 2002, Deng *et al*. 2007, Resch-Genger *et al*. 2008, Kamat 2008, Kim *et al*. 2013].

1.4 Light emitting diodes (LEDs)

1.4.1 Organic LEDs (OLEDs), polymer LEDs (pLEDs) and quantum dot LEDs (QDLEDs).

Organic semiconductors have interesting properties: high absorption coefficients in the visible range that offer the possibility to prepare thin photodetectors and photovoltaic cells; emission strongly red-shifted, which implies no reabsorption losses in OLEDs and low indices of refraction. Organic semiconductors consist of molecular structures with saturated electron systems. Many chemical compounds can be used for these devices and most of them can be deposited at RT and are compatible with flexible substrates [Walzer *et al.* 2007]. Recent advantages and efficiencies regarding OLEDs can be found reported elsewhere [Chen *et al*. 2004, Kulkarni *et al*. 2004, Walzer *et al.* 2007, Xiao *et al*. 2011, Thejokalyani *et al.* 2014]. Green, blue and red OLEDs have been built with good efficiencies and they have been implemented in commercial displays fabricated by Philips, TDK, Nippon Seiki, Sanyo and Pioneer [D'Andrade *et al*. 2004].

Polymer LEDs have several advantages: low-cost of manufacturing, easy processability over large areas with spin-coating, compatible with flexible substrates, ink-jet printing, small amount of wasted materials…They are obtained by doping a large band gap polymer material with various low band gap dyes to achieved a balanced and broad emission [Misra *et al*. 2006]. More information can be found elsewhere [Blom *et al*. 2000, Wu *et al.* 2009, Duarte *et al*. 2011]. Polymer LEDs have attracted attention in industrial communities because of the potential applications in full-colour flat-panel electroluminescent displays, black-lighting sources for liquid-crystal displays and solid-state lighting sources [Wu *et al*. 2009].

The use of quantum dots in display technology has attracted attention of scientists. Some of their advantages include: possibility for inexpensive and solution-based device fabrication, and direct injection of carriers into QDs without energy losses during down-conversion, leading to higher efficiencies [Talapin *et al.* 2013]. They are very close to full-scale commercialization. Recent reports have demonstrated their efficiency and thus, competitiveness with other energy display and solid-state technologies. The main features to be resolved are stability and manufacturability [Talapin *et al.* 2013]. Recently, some companies are starting to provide QDs to important display multinational companies, therefore, it is possible to expect that their present in commercial displays is coming soon [Bourzac 2013]. More information regarding recent advantages and efficiencies can be found elsewhere [Sun *et al*. 2009, Shirasaki *et al.* 2013, Chen *et al.* 2014].

References for Chapter 1.

[Anikeeva *et al.* 2009] Anikeeva P. O., Madigan C. F., Halpert J. E., Bawendi M. G. and Bulović V. **2008**, *Electronic and excitonic processes in light-emitting devices based on organicmaterials and colloidal quantum dots*, *Phys. Rev. B*, 78, 085434.

[Behr *et al.* 2008] Behr A., Eilting J., Irawadi K., Leschinski J. and Lindner F. **2008**, *Improved utilisation of renewable resources: new important derivatives of glycerol*, Green Chem., 10, 13-30.

[Bimberg *et al.* 2011] Bimberg, D., Pohl U. W. **2011**, *Quantum dots: promises and accomplishments*, Mater. Today, 14, 388-397.

[Bisio *et al.* 2008] Bisio C., Gatti G., Boccaleri E., Marchese L., Superti G. B., Pastore H. O. and Thommes M. **2008**, *Understanding physico-chemical properties of saponite synthetic clays*, Micropor. Mesopor. Mater., 107, 90-101.

[Blom *et al.* 2000] Blom P. W. M., Vissenberg M. C. J. M. **2000**, *Charge transport in poly(p-phenylene vinylene) light-emitting diodes*, Mater. Sci. Eng., 27, 53-94.

[Bourzac 2013] Bourzac K. **2013**, *Quantum dots go on display*, Nature, 493, 283.

[Brandner *et al.* 2009] Brandner A., Lehnert K., Bienholz A., Lucas M. and Claus P. **2009**, *Production of biomass-derived chemicals and energy: chemocatalytic conversions of glycerol*, Top. Catal. 52, 278-287.

[Brocker *et al*. 1970] Brocker F. J. and Kainer L., **1970**, German Patent 2024282.

[Burda *et al*. 2005] Burda C. Chen X. Narayanan R. and El-Sayed M. A. **2005**, *Chemistry and properties of nanocrystalls of different shapes*, Chem. Rev., 105, 1025-1102.

[Cavani *et al.* 1991] Cavani F. Trifirò F. and Vaccari A. **1991**, *Hydrotalcite-type anionic clays: preparation, properties and applications*, Catal. Today, 11, 173-301.

[Chen *et al.* 2004] Chen C.-T. **2004**, *Evolution of red organic light emitting diodes: materials and devices*, Chem. Mater., 16, 4389-4400.

[Chen *et al.* 2014] Chen J., Zhao D., Li C., Xu F., Lei W., Sun L., Nathan A. and Sun X. W. **2014**, *All solution.processed stable white quantum dot light-emitting diodes with hybrid ZnO@TiO_2 as blue emitters*, Sci. Rep., 4, 4085.

[Choy *et al.* 2007] Choy J-H., Choi S-J, Oh J-M. and Park T. **2007**, *Clay minerals and layered double hydroxides for novel biological applications*, Appl. Clay Sci., 36, 122-132.

[Climent *et al*. 2014] Climent M. J., Corma A. and Iborra S. **2014**, *Conversion of biomass platform molecules into fuel additives and liquid hydrocarbon fuels,* Green Chem., 16, 516-547.

[D'Andrade *et al*. 2004] D'Andrade B. W. and Forrest S. R. **2004**, *White organic light-emitting diodes for solid-state lighting*, Adv. Mater. 16, 1585-1595.

[Das *et al.* 2009] Das S. K. and D'Souza F. **2009**, *Synthesis of CdTe quantum dots of different sizes and interactions with water soluble porphyrins*, Proceedings of the 5th Annual GRASP Symposium, Wichita State University, 88-89.

[Del Hoyo 2007] Del Hoyo, C. **2007**, *Layered double hydroxides and human health: an overview*, Appl. Clay Sci., 36, 103-121.

[Demirbas 2009] Demirbas A. **2009**, *Progress and recent trends in biodiesel fuels*, Energ. Convers. Manage., 50, 14-34.

[Deng *et al*. 2007] Deng Z., Zhang Y., Yue J., Tang F. and Wei Q. **2007**, *Green and orange CdTe quantum dots as effective pH-sensitive fluorescent probes for dual simultaneous and independent detection of viruses*, J. Phys. Chem. B., 111, 12024-12031.

[Dresselhaus *et al*. 2001] Dresselhaus M. S. and Thomas I. L. **2001**, *Alternative energy technologies*, Nature, 414, 332-337.

[Duarte *et al*. 2011] Duarte A., Pu K.-Y., Liu B. and Bazan G. C. **2011**, *Recent advances in conjugated polyelectrolytes for emerging optoelectronic applications*, Chem. Mater., 23, 501-515.

[Gaponik *et al*. 2002] Gaponik N., Talapin D. V., Rogach A. L., Hoppe K., Shevchenko E. V., Kornowski A., Eychmüller A. and Weller H. **2002**, *Thiol-capping of CdTe nanocrystals: an alternative to organometallic synthetic routes*, J. Phys. Chem. B, 106, 7177-7185.

[García *et al.* 2014] García J. I., García-Marín H. and Pires E. **2014**, *Glycerol based solvents: synthesis, properties and applications*, Green Chem., 16, 1007-1033.

[Hall *et al.* 2003] Hall C., Tharakan P., Hallock J., Cleveland C., Jefferson M. **2003**, *Hydrocarbons and the evolution of human culture*, Nature, 426, 318-322.

[Hattori 1995] Hattori H. **1995**, *Heterogeneous basic catalysis*, Chem. Rev., 95, 537-558.

[Issariyakul *et al.* 2014] Issariyakul T. and Dalai A. K. **2014**, *Biodiesel from vegetable oils*, Renew. Sust. Energ. Rev., 31, 446-471.

[Johnson *et al.* 2007] Johnson D. T. and Taconi K. A. **2007**, *The glycerin glut: options for the value-added conversion of crude glycerol resulting from biodiesel production*, Environ. Prog., 26, 338-348.

[Kamat 2008] Kamat P. V. **2008**, *Quantum dot solar cells. Semiconductor nanocrystals as light harvesters*, J. Phys. Chem. C, 112, 18737-18753.

[Karinen *et al*. 2006] Karinen R. S. and Krause A. O. I. **2006**, *New biocomponents from glycerol*, Appl. Catal A. ., 306, 128-133.

[Kim *et al*. 2013] Kim J. Y., Voznyy O., Zhitomirsky D. and Sargent E. H. **2013**, *25th Anniversary article: colloidal quantum dot materials and devices: a quarter-century of advances*, Adv. Mater., 25, 4986-5010.

[Kloprogge *et al*. 1999] Kloprogge J. T., Komarneni S. and Amonette J. E. **1999**, *Synthesis of smectite clay minerals: a critical review*, Clays Clay Miner., 47, 529-554.

[Kulkarni *et al*. 2004] Kulkarni A. P., Tonzola C. J., Babel A. and Jenekhe S. A. **2004**, *Electron transport materials for organic light-emitting diodes*, Chem. Mater., 16, 4556-4573.

[Ma *et al*. 1999] Ma F. and Hanna M. A. **1999**, *Biodiesel production: a review*, Biores. Technol., 70, 1-15.

[Ma *et al*. 2007] Ma R., Liu Z., Takada K., Iyi N., Bando Y. and Sasaki T. **2007**, *Synthesis and Exfoliation of Co^{2+}–Fe^{3+} Layered Double Hydroxides: An Innovative Topochemical Approach*, J. Am. Chem. Soc., 129, 5257-5263.

[Ma *et al.* 2010] Ma R. and Sasaki T. **2010**, *Nanosheets of oxides and hydroxides: ultimate 2D charge-bearing functional crystallites,* Adv. Mater., 22, 5082-5104.

[Manasse 1915] Manasse E. **1915**, Atti. Soc. Tosc. Sc. Nat. Pisa (Proc. Verb), 24, 92.

[Martin *et al*. 2011] Martin A. and Richter M. **2011**, *Oligomerization of glycerol - a critical review*, Eur. J. Lipid Sci. Technol. 113, 100-117.

[Misra *et al*. 2006] Misra A., Kumar P., Kamalasanan M. N. and Chandra S. **2006**, *White organic LEDs and their recent advancements*, Semicond. Sci. Technol., 21, R35.

[Miyata 1975] Miyata S. **1975**, *The Syntheses of Hydrotalcite-Like Compounds and Their Structures and Physico-Chemical Properties I: The Systems Mg^{2+}-Al^{3+}-NO^{3-}, Mg^{2+}-Al^{3+}-Cl^{-}, Mg^{2+}-Al^{3+}-ClO^{4-}, Ni^{2+}-Al^{3+}-Cl^{-} and Zn^{2+}-Al^{3+}-Cl^{-}*, Clays Clay Miner., 23, 369-375.

[Mizugaki *et al*. 2014] Mizugaki T., Arundhathi R., Mitsudome T., Jitsukawa K. and Kaneda K. **2014**, *Highly efficient and selective transformations of glycerol using reusable heterogeneous catalysts*, ACS Sustainable Chem. Eng., 2, 574-578.

[Pagliaro *et al.* 2007] Pagliaro M., Ciriminna R., Kimura H., Rossi M. and Della Pina C. **2007**, *From glycerol to value-added products*, Angew. Chem. Int. Ed., 46, 4434-4440.

[Peng *et al.* 2000] Peng X., Manna L., Yang W., Wickham J., Scher E., Kadavanich A. and Alivisatos A. P. **2000**, *Shape control of CdSe nanocrystals*, Nature, 404, 59-61.

[Qiu *et al.* 2005] Qiu L., Chen W. and Qu B. **2005**, *Structural characterisation and thermal properties of exfoliatedpolystyrene/ZnAl layered double hydroxide nanocomposites prepared via solution intercalation*, J. Polym. Degrad. Stab., 87, 433-440.

[Ray *et al.* 2003] Ray S. S. and Okamoto M. **2003**, *Polymer/layered silicate nanocomposites: a review from preparation to processing*, Prog. Polym. Sci., 28, 1539-1641.

[Resch-Genger *et al*. 2008] Resch-Genger U., Grabolle M., Cavaliere-Jaricot S., Nitschke R. and Nann T. **2008**, *Quantum dots versus organic dyes as fluorescent labels*, Nat. Methods, 5, 763-775.

[Rousselot *et al*. 2002] Rousselot I., Taviot-Guého C., Leroux F., Léone P., Palvadeau P. and Besse J.-P. **2002**, *Insights on the Structural Chemistry of Hydrocalumite and Hydrotalcite-like Materials: Investigation of the Series* $Ca_2M^{3+(}OH)_6Cl{\cdot}2H_2O$ *(*M^{3+}*:* Al^{3+}*,* Ga^{3+}*,* Fe^{3+}*, and* Sc^{3+}*) by X-Ray Powder Diffraction*, J. Solid State Chem., 167, 137-144.

[Serrano-Ruiz *et al.* 2011] Serrano-Ruiz J. C., Luque R. and Sepúlveda-Escribano A. **2011**, *Transformations of biomass-derived platform molecules: from high added-value chemicals to fuels via aqueous-phase processing*, Chem. Soc. Rev., 40, 5266-5281.

[Shirasaki *et al.* 2013] Shirasaki Y., Supran, G. J., Bawendi M. G. and Bulović V. **2013**, *Emergence of colloidal quantum-dot light-emitting technologies*, Nat. Photonics, 7, 13-23.

[Sun *et al*. 2009] Sun Q., Subramanyam G., Dai L., Check M., Campbell A, Naik R., Grote J. and Wang Y. **2009**, *Highly efficient quantum-dot light-emitting diodes with DNA-CTMA as a combined hole-transporting and electron-blocking layer*, ACS Nano, 3, 737-743.

[Talapin *et al*. 2013] Talapin D. V. and Steckel J. **2013**, *Quantum dot light-emitting devices*, MRS Bulletin, 38, 685-691.

[Taylor 1997] Taylor H. F. W. **1997**, *Cement chemistry*, 2nd ed.; Thomas Telford Publishing: London.

[Thejokalyani *et al*. 2014] Thejokalyani N. and Dhoble S. J. **2014**, *Novel approaches for energy efficient solid state lighting by RGB organic light emitting diodes - a review*, Renew. Sust. Energ. Rev., 32, 448-467.

[Tichit *et al*. 1995] Tichit, D., Lhouty M. H., Guida A., Chiche B. H., Figueras F., Auroux A., Bartalini D. and Garrone E. **1995**, *Textural properties and catalytic activity of hydrotalcites*, J. Catal., 151, 50-59.

[Tichit *et al.* 2003] Tichit D. and Coq B. **2003**, *Catalysis by hydrotalcites and related materials*, CATTECH, 7, 206-217.

[Trujillano *et al*. 2009] Trujillano R., Vicente M. A., Rives V., Korili S. A., Gil A., Ciuffi K. J. and Nassar E. J. **2009**, *Preparation, alumina-pillaring and oxidation catalytic performances of synthetic Ni-saponite*, Micropor. Mesopor. Mater., 117, 309-316.

[Vicente *et al*. 2010] Vicente I., Salagre, P., Cesteros Y., Medina F. and Sueiras J. E. **2010**, *Microwave-assisted synthesis of saponite*, Appl. Clay. Sci., 48, 26-31.

[Vieille *et al*. 2003] Vieille L., Rousselot I., Leroux F., Besse J.-P. and Taviot-Guého C. **2003**, *Hydrocalumite and its polymer derivatives. 1. Reversible thermal behaviour of Friedel's salt: a direct observation by means of high-temperature in situ powder X-Ray diffraction*, Chem. Mater., 15, 4361-4368.

[Walzer *et al.* 2007] Walzer K., Maennig B., Pfeiffer M. and Leo K. **2007**, *Highly efficient organic devices based on electrically layers*, Chem. Rev., 107, 1233-1271.

[Wang *et al*. 2005] Wang X., Zhuang J., Peng Q. and Li Y. **2005**, *A general strategy for nanocrystal synthesis*, Nature, 437, 121-124.

[Wang *et al*. 2012] Wang Q. and O'Hare D. **2012**, *Recent advances in the synthesis and application of layered double hydroxide (LDH) nanosheets*, Chem. Rev., 112, 4124-4155.

[Wijffels *et al.* 2010] Wijffels R. H. and Barbosa M. J. **2010**, *An outlook on microalgal biofuels*, Science, 329, 796-799.

[Wu *et al*. 2005] Wu Q., Olafsen A., Vistad O. B., Roots J. and Norby P. **2005**, *Delamination and restacking of a layered double hydroxide with nitrate as counter anion*, J. Mater. Chem., 15, 4695-4700.

[Wu *et al*. 2009] Wu H., Ying L., Yang W. and Cao Y. **2009**, *Progress and perspective of polymer white light-emitting devices and materials*, Chem. Soc. Rev., 38, 3391-3400.

[Xiao *et al*. 2011] Xiao L., Chen Z., Qu B., Luo J., Kong S., Gong Q. and Kido J. **2011**, *Recent progresses on materials for electrophosporescent organic light-emitting devices*, Adv. Mater., 23, 926-952.

[Zhang *et al*. 2010] Zhang D., Zhou C.-H., Lin C.-X., Tong D.-S. and Yu W.-H. **2010**, *Synthesis of clay minerals*, Appl. Clay Sci., 50, 1-11.

[Zhou *et al.* 2013] Zhou C. H., Zhao H., Tong D. S., Wu L. M. and Yu W. H. **2013**, *Recent advances in catalytic conversion of glycerol*, Catal. Rev., 55, 369-453.

CHAPTER 2

Aims of this thesis

2.1 Aims of this thesis.

The aim of this thesis is the synthesis of different layered double hydroxides and study their application in the fields of heterogeneous catalysis and in the assembly of light-emitting diodes based on thiol-capped CdTe nanoparticles. Their versatility allows them to be transformed in catalysts (mixed oxides) after their calcination. They can also be delaminated in positively charged nanosheets, with many applications for hybrid materials' synthesis and other functional applications. In delaminated form, they can be the matrix for quantum dot nanoparticles and form the emissive layer in light-emitting diodes.

In this thesis book, the experimental results are explained in chapters 4, 5 and 6.

Chapter 4 focuses in the synthesis and characterization of CaAl layered double hydroxides and on their reconstruction after their calcination. Delamination was tested for all synthesized and reconstructed layered double hydroxides. The aims of the chapter are the following:

- To synthesize several CaAl layered double hydroxides (CaAl-LDHs) with chloride as anion using different aging techniques, in order to study the effect over the crystallinity. In order to perform a cost-saving process in terms of energy consumption, microwave irradiation was used along with conventional heating, in either autoclaving or refluxing.
- To synthesize CaAl-LDHs with chloride and nitrate as anions in order to study their delamination behavior. Two delamination procedures were compared: in the presence of formamide using mechanical stirring and the other procedure using ultrasounds in repeated cycles. The CaAl-LDHs were calcined and reconstructed in aqueous media in the presence of one of the following salts: NaCl or $NaNO_3$. Delamination tests were also performed to reconstructed samples, following as well the two procedures mentioned above, using mechanical stirring and ultrasounds in the presence of formamide.
- To synthesize a hybrid material of CaAl-LDH and CdTe nanoparticles by rehydration of a calcined hydrocalumite.

Chapter 5 focuses in the etherification of glycerol towards polyglycerols using calcined MgAl and CaAl layered double hydroxides as heterogeneous catalysts.

The aim is chapter is to test a series of calcined layered double hydroxides for the etherification reaction of glycerol to short-chain polyglycerols. The catalytic results have been correlated to the acid and basic properties. The influence and the effect of several parameters were studied on the etherification reaction, such as the nature of the catalyst, the different hydrothermal treatments and the temperature of calcination:

- The precursors: MgAl-LDHs and CaAl-LDHs.
- The hydrothermal treatments: using microwave irradiation or conventional heating, in autoclave or refluxing.
- Calcining the catalysts at different temperatures: 723, 923 and 1073 K.

Chapter 6 focuses in the synthesis of several materials with luminescent properties and in the assembly of light-emitting diodes based on thiol-capped CdTe nanoparticles embedded in different inorganic matrixes. The aims of the chapter are the following:

- To synthesize and characterize hybrid materials with luminescent properties that could be candidates as emissive layers in optoelectronic devices. In our case, we were interested mainly in LEDs. These hybrid materials are layered double hydroxides and clays (hectorites and saponites) intercalated with capped-CdTe quantum dots.
- To synthesize and delaminate layered double hydroxides materials (with the following metals: CaAl and NiAl) to produce films that will be alternated with layers of capped-CdTe quantum dots, and later tested as candidates for emissive layers in optoelectronic devices.
- To build LEDs based on these emissive layers and characterize their electrical characteristics. In order to make a cost-effective process, the assembly was performed under air conditions (with humidity, RT and presence of dust) outside the glovebox.

In the assembly of the devices, four parameters were studied:

- Type of emissive layer matrix (delaminated layered double hydroxide or clay).
- Number of alternated depositions of the layers that form the emissive layer.
- Type of metal deposited as cathode (Al or Ca/Ag).
- Post-annealing (after the deposition of the capped CdTe quantum dots).

CHAPTER 3

Instrumentation & Characterization techniques

3.1 Instrumentation.

3.1.1 Microwave oven.

Microwaves are non-ionizing electromagnetic radiations that are in the range between 300 MHz-300GHz; upon interacting with liquid or solid materials, they produce dipole reorientation in dielectric materials and ionic conduction if there are ions which can be drifted under the field. In this way, it is possible to achieve a uniform bulk heating of the materials, reducing thermal gradients originated in conventional heating where energy is transferred by conduction, convection or radiation from the surface of the vessel. Figure 3.1 shows the microwave instrument used in this work with an autoclave carrousel inside.

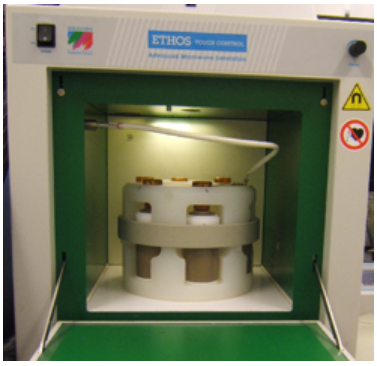

Figure 3.1. Microwave irradiation instrument.

In order to improve the crystallinity, a hydrothermal treatment is applied after complete addition of the salts when synthesizing materials such as layered double hydroxides and clays, among others. The use of microwave radiation as a source of heating not only reduces the aging time considerably but also enhances the kinetics of crystallization, apart from saving costs of time and energy during their preparation [Bergadà *et al.* 2007a, Bergadà *et al.* 2007b, Bergadà *et al.* 2007c].

The use of microwave irradiation during the aging treatment of inorganic materials reduces enormously aging times but also provides much more crystallinity in the final material, as observed when applied to the synthesis of zeolitic materials and hydrotalcites [Benito *et al.* 2006, Azzolina Jury *et al.* 2014, Bergadà *et al.* 2007, Meng *et al.* 2014, García Martínez *et al.* 2003] or in the preparation of clays (hectorites and saponites among others), where aging times have been remarkably decreased [Vicente *et al.* 2010, Sánchez*et al.* 2003].

In this work, the microwave oven (Milestone Ethos touch control) with temperature control and a maximum power used of 500 W, was used for the aging of layered double hydroxides and clays. It was located at the *Greencat* facilities.

Two modes of operation were used: by the use of autoclaves or by the use of reflux, with constant agitation in both cases, at a particular temperature. The desired ramp/s was/were

selected using a software. In order to avoid overpressure in the autoclaves, they cannot be filled more than 60% of their capacity. Also, the positions where the autoclaves are located need to be balanced inside the instrument in order to avoid instrument failure.

3.1.2 Ultrasounds bath.

Sonochemistry is a research area where molecules experience a chemical reaction because of the application of ultrasound radiation (20 kHz-10 MHz). The phenomenon responsible for the sonochemical process is acoustic cavitation, which can be defined as a processes composed by the following steps: creation, growth and collapse of a bubble that is formed in the liquid. The possible explanation for the creation of nanoparticles would be that the kinetics does not allow growth of the nuclei, and in each collapsing bubble a few nucleation centers are formed whose gorwth is limited by the short collapse. Sometimes the nanoparticles exhibit a high crystallinity. This could be related to the temperature in which this reaction takes place [Gedanken 2004].
Ultrasonic devices are used for a variety of applications [Hielscher website]:

- Homogenize the particle size for liquids and/or solids.
- Dispersing and deagglomeration of solids into liquids.
- Emulsifying.
- Grinding of particles.
- Cell disintegration, cellulosic material disintegration.
- Extraction of proteins and enzymes from cells.
- Chemical reactions and processes.

In this work the ultrasound bath (Ultrasons-H, P Selecta) was used for several applications: glassware cleaning, reconstruction of several calcined layered double hydroxides, deagglomeration and mixing of solutions used for clay synthesis and to provoke layered double hydroxide delamination. The ultrasound bath was located at the *Greencat* facilities.

3.1.3 Spinner.

Spin coating is a technique used for the deposition of thin films on a substrate. Firstly, the fluid is deposited in the center, then the substrate is spinned at high speed (typically from 500 to 5000 rpm). Because the centripetal acceleration, the fluid will spread to and off each edge of the substrate, leaving a thin film. The film thickness and other important properties depend on the nature of the fluid and the parameters of spin coating.
The following equation reflects the most important parameters for spin coating:

$$H \sim \omega^{-N} \quad \text{(eq. 3.1)}$$

where *H* is the film thickness, *ω* the spin speed and *N* the solvent factor. When there is no

evaporation, the film thickness varies with the spin speed and time (eq. 3.2):

$$H \sim \omega^{-1} t^{-0,5} \quad \text{(eq. 3.2)}$$

In most applications, the evaporation rate varies with the square root of the spin speed (eq. 3.3):

$$H \sim \omega^{-0,5} \quad \text{(eq. 3.3)}$$

The film thickness can be analyzed experimentally by the following equation (eq. 3.4):

$$H = \frac{(m_f - m_i)}{\rho \times A} \quad \text{(eq. 3.4)}$$

where m_f is the mass of processed wafer, m_i is the mass of bare wafer, ρ the density of dispensed fluid and A the surface area of wafer.

When operating with the instrument, it is important not to have air bubbles in the fluid, otherwise pinholes will appear in the film. If the film is not homogeneous, several possibilities would explain the reason: too high speed, fluid not dispensed appropriately at center or insufficient volume [Laurell Technologies Corporation website, Brewer Science website].

The main applications of spin coating are the deposition of photoresisting patterns, insulating layers, polymer layers, lubricants or suspension films…

In this work, the spin coating was used for the deposition of the films during the process of the light-emitting diode assembly. The particular experimental conditions for each device can be found in Chapter 6. The spinner instrument (Laurell) was located at the *Nephos* facilities and used nitrogen gas as protective environment and to provoke the vacuum. The instrument was used outside the glove box. During the stage at *Centro Nanosistemi*, in Alessandria, Italy, a spin coater (Laurell) was used for film optimization and assembly of the light-emitting diodes. It was located in a glove box filled with nitrogen gas.

3.1.4 Vacuum deposition chamber.

Resistive thermal evaporation is a very common metal deposition technique. It consists in vapourising a solid metal by heating it to high temperatures and re-condensing it onto a cooler substrate to form a thin film. The heating is accomplished by passing a large current through a filament container which has a finite electrical resistance. The filament is chosen according the evaporation temperature and its inertness to alloy the chemical reaction with the evaporate. When the metal is evaporated, the vapour undergoes collisions with the surrounding gas molecules inside the evaporation chamber. A fraction is then scattered within a given distance during their transfer through the ambient gas. Pressures lower than $1 \cdot 10^{-5}$ torr are needed for this phenomena to occur for a substrate-source distance of the range 10 to 50 cm. Appropriate vacuum is also useful to work in a pollution-free environment. In order to monitor the deposition,

several parameters should be known of the metal or metals to be deposited: density, Z (acoustic impedance), tooling factor and minimum current required for evaporate each metal [Chopra et al. 1983, Stuart 1983, Mbraun website, Bashar 1998]. Figure 3.2 shows a schematic representation of the evaporation chamber.

Main applications of vacuum deposition instruments are: deposition of metallic films, semiconductor films, solar cells, optical filters, mirrors, resistant coatings, protection coatings…

In this work, vacuum deposition was performed in an evaporation chamber (MBraun MB-ProVap-3) located inside the glove box (Mbraun Glove box workstation) at *Nephos* facilities. The pressure used was $1 \cdot 10^{-6}$ torr or less. The cathode was thermally evaporated for the light-emitting diodes using this instrument.

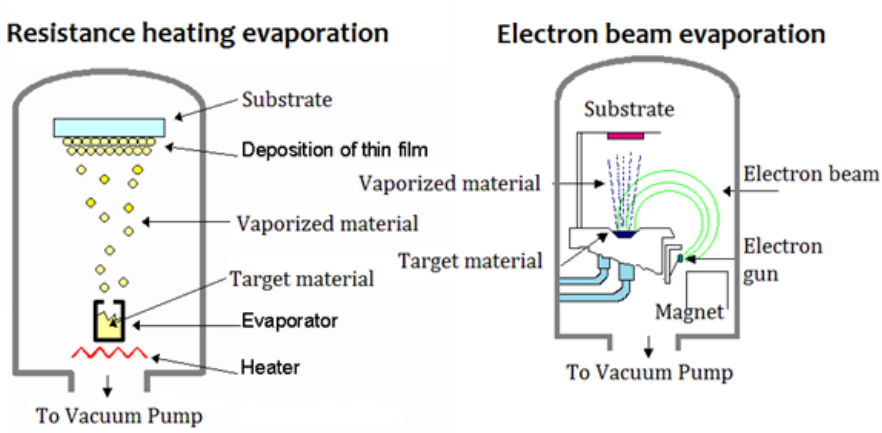

Figure 3.2. Schematic representation of the vacuum chamber. Extracted from www.hivatec.ca

3.2 Characterization techniques.

3.2.1 X-Ray Powder Diffraction (XRPD).

X-Ray powder diffraction is one of the most powerful tools for solid characterization in solid state chemistry and materials science. W.H. Bragg and his son W.L. Bragg developed a relationship to explain the cleavage faces of crystals that appeared to reflect X-ray beams at certain angles of incidence (θ). This lead them to determine the crystal structure of NaCl, ZnS and C (diamond). A crystal consists of a periodic arrangement of the unit cell into a lattice. The unit cell can contain a single atom or atoms in a fixed arrangement.

The following is the equation of Bragg's law (eq. 3.5):

$$n\lambda = 2d\sin\theta \qquad \text{(eq. 3.5)}$$

where *d* is the distance between atomic layer in a crystal, *λ* the wavelength of the incident X-ray beam, *n* an integer and *θ* the angle of incidence. The equation is an example of the X-Ray wave

interference, and evidenced the periodic atomic structure of crystals (Fig. 3.3).

With X-Ray diffraction it is possible to i) measure the average spacings between layers or rows of atoms, ii) determine the orientation of a single crystal or grain, iii) determine the crystal structure of an unknown material, iv) measure the size, shape and internal stress of small crystalline regions.
The International Center for Diffraction Data (ICDD) collects and updates a powerful database to identify crystal structures. The information is stored in single JCPDS (Joint Committee on Powder Diffraction Standards) cards. These cards show the information in an ordered structure, regarding the d-spacing determined from the angle of diffraction and the intensity (I), experimentally measured, along with the chemical formula, the mineral name, if appropriate, a unique identification number and a reference to the original source of the data.

The peak full width at half maximum (FWHM) of a 2θ peak position gives important information regarding the particle or gran size at a specific direction. The Scherrer equation (eq. 3.6) is used to determine the size of particles of crystals in the form of powder [Cullity 1979, Zur Loye 2013, Moore *et al.* 1997].

$$D = K\lambda/(\beta\cos\theta) \qquad \text{(eq. 3.6)}$$

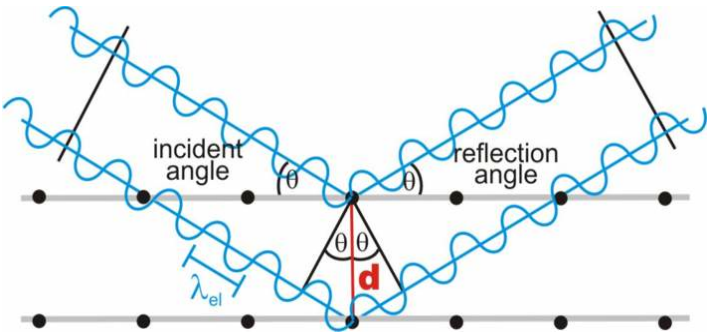

Figure 3.3. Bragg's law, constructive interference. Extracted from http://www.microscopy.ethz.ch/bragg.htm

In this thesis, XRPD measurements were made using a Siemens D5000 diffractometer (Bragg–Brentano parafocusing geometry and vertical–goniometer) fitted with a curved graphite diffracted-beam monochromator and diffracted-beam Soller slits, a 0.06º receiving slit, and scintillation counter as a detector. The instrument was located at *Servei de Recursos Científics* facilities of URV. The angular 2θ diffraction range was between 5º and 70º. Sample was dusted on to a low background Si(510) sample holder. The data were collected with an angular step of 0.05º at 3 s per step and sample rotation. CuK_{α} (1.541 Å) radiation was obtained from a copper X-ray tube operated at 40 kV and 30 mA. In order to compare the results, JCPDS files were used to identify the phases.
The JCPDS patterns used in this thesis are summarized in table 3.1:

Table 3.1. List of JCPDS files used in this thesis.

Compound	Formula	JCPDS #
Chloride CaAl-LDH	$Ca_2Al(OH)_6Cl{\cdot}_2H_2O$	035-0105
Carbonate CaAl-LDH	$Ca_4Al_2O_6CO_3{\cdot}11H_2O$	041-0219
Nitrate CaAl-LDH	$(Ca_4Al_2(OH)_{12})(NO_3)_2(H_2O)_4$	089-6723
Katoite	$Ca_3Al_2(O_4H_4)_3$	074-3032
Calcite	$CaCO_3$	072-1652
Periclase	MgO	089-4248
Lime	CaO	004-0777
Mayenite	$Ca_{12}Al_{14}O_{33}$	048-1882

3.2.2 Fourier transform infrared spectroscopy (FT-IR).

Infrared spectroscopy is an important technique based on the interaction of infrared radiation with matter used to identify the presence of certain functional groups in a sample. Infrared refers to that part of the electromagnetic spectrum between the visible and the microwave regions.

Energies in infrared radiation correspond to the energies involved in bond vibrations: IR is absorbed by molecules or solid structures and converted into energy of molecular vibration. When the radiant energy matches the energy of a specific vibration, absorption occurs. There are two main types of vibrations: stretching and bending.

IR region is divided into three regions: the near, mid and far IR. It is the mid region, between 4000 and 400 cm^{-1} that is more useful in materials science as it contains the vibration energies of the most common functional groups, and allows to identify pure compounds and to detect the presence of impurities.

Generally, a background spectrum must be acquired before sample analysis. This is a response curve of the spectrometer and takes into account of the combined performance of source, interferometer and detector. It also includes the contribution of any ambient water [Settle 1997, Larkin 2011, Cheng 2005, Font 2006].

In this work, FT-IR analysis was used for the identification of the main functional groups and anions in materials such as layered double hydroxides and clays. The exchange with quaternary salts with clays was also checked by FT-IR.

In this thesis, Infrared spectra were recorded on a Bruker-Equinox-55 FTIR spectrometer, located at the department of Inorganic and Physical Chemistry of URV. The spectra were acquired by accumulating 32 scans at 4 cm^{-1} resolution in the range of 400–4000 cm^{-1}. Samples were prepared by mixing the powdered solids with pressed KBr disks in a mass ratio of 1:250, and dried in an oven before measurements. Grinding and mixing is done using a mortar and pestle. The mixture is then pressed into a transparent disk at sufficient high pressure. The sample is ready to be analyzed.

3.2.3 Electron microscopy.

The interaction of a high energy electron beam with the specimen will produce various effects resulting in a range of signals being emitted. The incident electrons interact with the specimen atoms and are significantly scattered by them (rather than penetrating the sample in a linear way). Most of the energy of an electron beam will eventually end up heating the sample, however before the electrons come to rest, they undergo two types of scattering: elastic and inelastic. Elastic scattering is known as electron backscattering. Inelastic interactions produce different effects: secondary electrons, phonon excitation, cathodoluminescence, continuum radiation, characteristic X-Ray radiation, plasmon production and Auger electron production.

Transmission electron microscopy (TEM).

In TEM microscopy the image is obtained from a beam of electrons that are transmitted through a thin sample. These electrons interact with the sample as they pass through it. Therefore, samples should be thin in order to observe a good resolution in the micrographies.
In this work, TEM microscopy was used to characterize the morphology of the materials synthesized and to characterize the size and size distribution of the supplied thiol-capped CdTe nanoparticles.
In this thesis, Transmission electron microscope images were collected using a JEOL 1011 Transmission Electron Microscope operating at 80 kV and magnification values of 12–60k. The instrument was located at *Servei de Recursos Científics* facilities of URV. Samples were dispersed in ethanol, and a drop of resultant suspensions was poured on carbon coated-copper grids. They were introduced into the instrument using a two-specimen holder. Figure 3.4 shows a TEM instrument.

Figura 3.4. Jeol model 1011 microscope. Image extracted from http://www.eurl-mollusc.eu.

Scanning electron microscopy (SEM).

The main feature of SEM microscope is that it utilizes electron beams to produce high spatial resolution and high depth of field images of solid samples because of the secondary electrons. From those images, it is possible to get information regarding topography, chemical, magnetic and electronic state of the sample. As technology advanced, on later years several groups worked on improving the instrument. The signals under the stimulation of the beam are collected and detected by a detector, then amplified and used to modulate the brightness of the display tube. Magnification is obtained by decreasing the area scanned [Zhou et al. 2006, Hafner 2007, Vernon-Parry 2000].

In this work, SEM microscopy was used to characterize the morphology of the powder samples and of samples that were on glass substrates.

The scanning electron micrographs were obtained with a JEOL JSM-35 C scanning microscope operating at an accelerating voltage in the range 15–25 kV, work distance of 14 mm and magnification values between 3000 and 10000x. The instrument was located at *Servei de Recursos Científics* facilities of URV.

Two sample preparations have been used in this work: powder samples have been attached to a carbon label sticked to a metal stub. The excess of sample was removed using a compressed-air gun. Then, the sample was introduced directly into the instrument using a sample-holder or it was sputtered with a thin layer of gold to increase the conductivity and thus the quality of the screen-image.

For the case of glass-substrated samples, the opposite face was attached to a carbon label sticked to a metal stub and was always sputtered with a thin layer of gold. When the glass-substrated sample was not sputtered it could be used again for other characterization techniques.

Environmental scanning electron microscopy (ESEM).

The ESEM microscopy is an evolution of the SEM instrument, necessary in order to study samples that are not in the form of a powder or an easy-manipulated solid. In this way, live cell samples and geological specimens, for example, and in general, samples in its *natural* state can be analyzed to obtain electron micrographs.

The main difference between SEM and ESEM instruments are that for the case of ESEM a *false vacuum* is created by applying a gas into the sample chamber that creates a deteriorated or low vacuum. The electron column optics was specially designed in a way that the column is divided into different pressures zones separated by pressure limiting apertures.

The gas inside the chamber acts as an electrical charge conductor avoiding sample charging and facilitates signal detection. It also acts as a conditioning medium, preventing evaporation of liquids from a sample. This phenomenon allows the study of liquids, oils and samples that can even be observed on *in situ* evolutions [Danilatos 1981, Danilatos 1994, Bogner *et al.* 2007].

In this work, ESEM micrographs were recorded in order to characterize the optimization process for device assembly.
In this thesis, ESEM analysis was performed in a FEI QUANTA 200 at the facilities of *Centro Nanosistemi*, in Alessandria (Italy). Sample preparation was similar to that of SEM, which can be found in the previous section.

Selected area electron diffraction (SAED).

SAED and microdiffraction patterns of a crystal allow to obtain structural information of a sample: regarding the symmetry of its lattice and calculate the interplanar distances. A static beam of electrons at accelerating voltage illuminate a region of an electron transparent specimen which is immersed in the objective lens of the microscope. The transmitted and diffracted electrons are recombined by the objective lens to form a diffraction pattern in the back focal plane of that lens and a magnified image of the sample in its image plane. A number of intermediate lenses are used to project either the image or the diffraction pattern onto a fluorescent screen for observation [Williams *et al.* 2009, Koch 2006, Vernon-Parry 2001].
Diffraction contrast arises because the intensity of the diffracted beams is different in different regions of the specimen. These variations may arise because of changing diffracting conditions or because of differences in specimen thickness. On the images there will be spots, some of them faint spots; other times they will form large disks, which contain structure information. In the images of diffraction studies in TEM the position of the spot is crucial compared with their intensities [Bozzola *et al.* 1998, De Graef 2003].
In this work SAED images were obtained to have information of the crystallinity of particles that were previously characterized by TEM microscopy. The instrument was located at *Servei de Recursos Científics* facilities of URV.

Energy-dispersive X-Ray spectroscopy (EDX).

As explained in section 3.2.3, inelastic scattering is produced as a result of the interaction of the electron beam with the matter. This leads to emission of the characteristic X-Rays from the elements that are present in the sample. It is possible to identify the chemical composition of a sample. The phenomenon is explained by energetic electrons that transfer some of their energy to atoms along their trajectory by ionizing inner shell electrons. Because electrons are ionized, others of less energy occupy their position; the difference in energy is converted in photons that have λ in the range of X-Rays.
In this work, EDX was used in order to characterize the presence of particular elements in powder samples of the synthesized materials in order to establish the atomic ratio between these two elements [Garratt-Reed et al. 2003, Boothroyd 2010].
EDX microanalysis were recorded using a JEOL 6400 electron microscope (3.5 nm resolution at 30 kV) fitted with an energy-dispersive X-ray spectrometer (Inca-Energy, Oxford Instruments) and Si(Li) detector with 1.38 eV energy resolution. The instrument was located at *Servei de*

Recursos Científics facilities of URV. From the results, Cl/Al atomic ratio was determined for all catalysts. For EDX microanalysis, samples were not sputtered in order to avoid the interference of any metal in the results.

3.2.4 Atomic Force Microscopy (AFM).

The AFM instrument is a high-resolution type of atomic probe microscopy. It uses a sharp probe moving over the surface of a sample in a raster scan. The probe is a tip at the end of a cantilever which bends in response to the force between the tip and the sample.
When the tip is brought into proximity of a sample surface, forces between the tip and the sample lead to a deflection of the cantilever according to Hooke's law. Depending on the situation, forces that are measured in AFM include mechanical contact force, van der Waals forces, capillary forces, chemical bonding, electrostatic forces, magnetic forces… The instrument functions with-out optical focusing elements. Working with tapping mode, the oscillation amplitude is large and the position of the tip is close to the surface, in an area of repulsions. The tip brushes in each cycle the repulsive wall of the surface of the sample. The force applied to the surface is very small and almost no friction force occurs, and no time for adhesive effects arise [Pujol 2014]. The information in *z* axis provides information about the morphology of the sample.

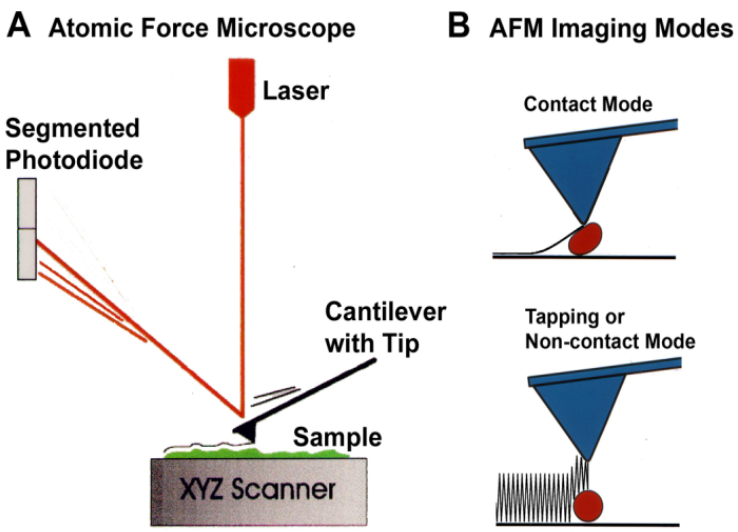

Figure 3.5. AFM working diagram. Image extracted from http://web.physics.ucsb.edu/~hhansma/biomolecules.htm

Figure 3.5 shows a typical working diagram for an AFM instrument. The lateral forces are reduced as the tip scans over the surface. Obtaining image contrast can be obtained with this mode [Meyer *et al.* 2003, Ortiz 2007, Jalili *et al.* 2004].

In this work, AFM microscopy was used to characterize the morphology and thickness of delaminated particles of layered double hydroxides.

In this work, an AFM-Pico Plus 2500 from Molecular Imaging is the instrument used, in tapping mode. The instrument was located at *Servei de Recursos Científics* facilities of URV.

Samples are deposited in a mica layer tapped to a small disk substrate. In order to treat the images, freeware software WsxM 5.0 was used to process the AFM images of the samples. The mode used in this work is the tapping mode.

3.2.5 N_2 Physorption.

When a gas molecule hits a solid surface, it can bounce off or remain fixed at the surface, which would be adsorption. The molecule may diffuse over the surface, stay fixed, react or dissolve in the solid, process known as absorption. The N_2 gas molecules remain united to the solid surface through Van der Waals forces at the temperature of 77 K. This fact explains the characteristics of physisorption: i) weak interaction, ii) exothermic process, iii) the physisorbed molecule does not react since the energy is not enough to break the bond, iv) there is no selectivity between adsorbate and adsorbant, v) physisorption is produced by multi-layers.

For the case of solids it is way easier to measure the quantity of adsorbed gas at a certain temperature as the pressure of the gas in the equilibrium with the solid changes. After repeating the experiment at different pressures it is possible to obtain the data to build the adsorption isotherm: quantity of adsorbed gas vs. gas pressure in the equilibrium at a certain temperature.

These N_2 adsorption isotherms are classified in 6 types (Fig. 3.6):

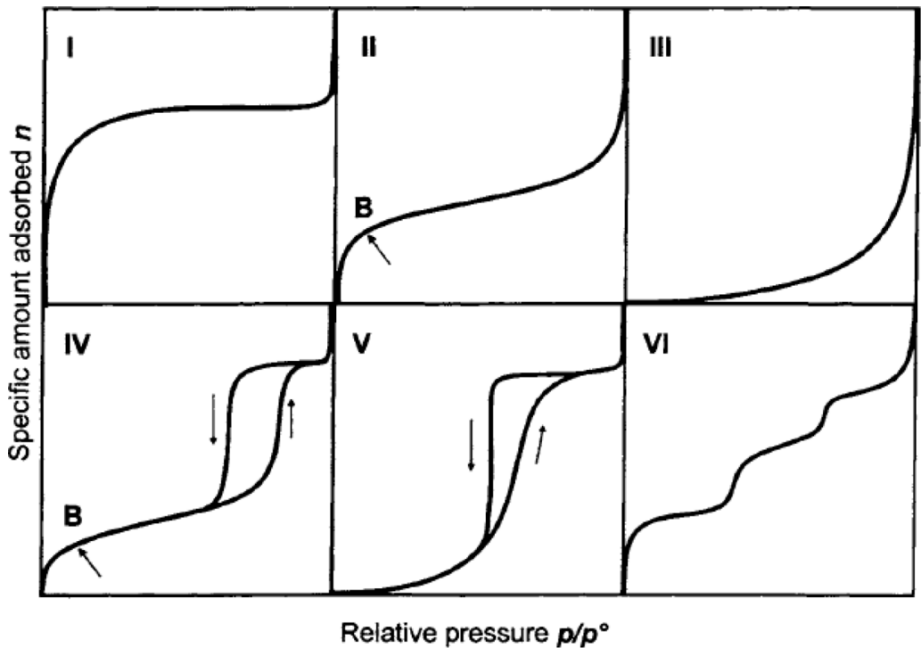

Figure 3.6. N_2 Physisorption isotherms. Figure extracted from www.mdpi.com

- Type I: it is called Langmuir's isotherm. It corresponds to adsorption as a monolayer. The adsorbed quantity increases with the pressure until it reaches a maximum value corresponding to the surface monolayer coating. This isotherm belongs to a chemisorption process. It is characteristic of microporous solids.
- Type II: it corresponds to a multilayer physical adsorption. The formation enthalpy of the first layer is higher (bigger negative number) than the rest of the layers. It is characteristic of macroporous solids or non-porous.
- Type III: it corresponds to a multilayer physical adsorption where the equilibrium constant of the first layer formation is the same for the following.
- Types IV and V: they correspond to multilayer adsorption for porous materials. They present hysteresis due to condensation because of the irregular form of the capillars. They are characteristic of mesoporous solids.
- Type VI: it is less common. It only occurs for solids with a non-porous uniform surface.

The classification of materials depending their pore size is: i) microporous (< 2 nm), ii) mesoporous (between 2 nm and 50 nm), iii) macroporous (>50 nm).

From the adsorption isotherm, several theories have been formulated in order to extract valuable information.

- BET (Brunauer Emmett and Teller) theory: The fundamental assumption is that the forces active in the condensation of gases also are responsible for the binding energy in multimolecular adsorption.
- t-plot theory: it can be used to evaluate the microporous contribution of a solid. It compares the isotherm with the isotherm of a non-porous standard solid. In the original method, the adsorbed quantity is represented vs. *t*, which is the thickness that corresponds to a multilayer calculated from the standard isotherm. The standard isotherm is obtained with a reference non-porous solid.
- BJH (Barrett Joyner and Halenda) method: it is used to determine the pore size distribution. The model assumes that pores have a cylindrical shape and that pore radius is equal to the sum of the Kelvin radius and the thickness of the film adsorbed on the pore wall.

In this work, physisorption analysis was used to determine the specific BET surface area of the materials synthesized. Before the analysis, sample is heated for some hours to clean the surface and eliminate adsorbed water. Vacuum is also used. During analysis, the sample is maintained at cryogenic temperature (that of liquid N_2). Gas usually is supplied at near ambient temperature and at precise pressures through a manifold having accurately known volume and temperature [Brunauer *et al.* 1983, Thomas 2006, Dabrowski 2001].

Brunauer-Emmet-Teller (BET) theory was applied to calculate total surface areas from the nitrogen adsorption isotherms at 77 K (Quantachrome Quadrasorb SI, sensitivity of the

instrument is 0.01 m^2/g.). Samples, between 0.2 and 0.3 g, were previously degassed under vacuum at 423 K (Quantachrome FloVac Degasser) for 24 h. The instrument was located at the *Greencat* facilities. Average pore size was calculated from BJH (Barrett-Joyner-Halenda) method. External surface area was calculated from t-plot (statistical Thickness) method.

3.2.6 Thermogravimetric analysis (TGA).

Thermogravimetric analysis is a technique in which the mass of a substance is monitored as a function of temperature or time as the sample is subjected to a controlled temperature program in a controlled atmosphere. The mass loss is used to study the decomposition process of a sample. The results can be presented as weight vs. temperature or rate of loss weight vs. temperature.

A correction has to be done with the empty crucible that will be used for the analysis: when the crucible is heated when empty, there is generally, an apparent change in weight with increasing temperature. This apparent change in weight can be caused by a variety of factors: air buoyancy, convection effects within the furnace, crucible geometry... It is necessary to record a blank of the crucible in the same conditions of the sample analysis and subtract the weight difference to the plot.

The sample has to be ground and the size of the particles should be as small as possible, in order to avoid foam.

Some of the applications include:

- thermal stability, material purity and determination of humidity.
- Corrosion studies, gasification processes and kinetic processes.

For the particular case of this thesis, the gas atmosphere has been inert, from N_2. This is because it does not take part in the reaction and it removes gaseous products away from crucible [Coats *et al.* 1963, Fröberg 2010, Metler Toledo website].

Thermogravimetric analyses were carried out in a Perkin Elmer TGA 7 microbalance equipped with a 273 – 1373 K programmable temperature furnace. The instrument was located at the *Greencat* facilities. The accuracy was 1 g. Each sample was heated in an N_2 flow (80 cm^3) from 298 K to 1000 K at 5 K/min.

The thermobalance can be also used to study the acidity of a compound where an acid substance has been chemisorbed to. The temperature desorption is monitored and offers a powerful tool to study the acidity of a compound.

In this thesis, surface acidity was determined through cyclohexylamine adsorption followed by thermogravimetric analyses [Mokaya *et al.* 1997]. All samples were stored in a desiccator to avoid water adsorption. 100 mg of the catalyst were placed in a crucible. Cyclohexylamine was dropped with a Pasteur pipette until the liquid covered the solid particles. The crucible was sealed with parafilm but for a small overture and kept overnight inside a fume hood. Then, the mixture was heated in a furnace muffle at 523 K for 2 h 50 mg of the mixture were then analyzed by thermogravimetric analysis (Setaram, Labsys TG DTA/DSC) from 303 to 1123 K at 10 K/min

under N_2 flow. The same test, without cyclohexylamine, was performed for every calcined sample, in order to subtract any weight loss due to decomposition. The weight loss can be associated to the chemisorbed cyclohexylamine. Results were indicated as mmol of cyclohexylamine chemisorbed per gram of catalyst. The temperature of cyclohexylamine desorption was calculated from the first derivative graph and used to compare the acidity strength of the samples.

3.2.7 Temperature Programmed Desorption (TPD).

Chemical adsorption isotherms provide information of the active surface of catalysts and enhances catalyst evaluation. This information can lead to optimize catalyst design. In contrast to physical adsorption, chemical adsorption is a much more stronger union. Due to the bond strength, chemical adsorption is not easy to reverse. Chemisorption is more selective than physical adsorption and it is a single layer process, most of the times.

In this thesis, flowing gas techniques were used. After the sample was cleaned at 723 K, the sample was saturated with a flow of CO_2 (in order to study the basicity of catalysts). TPD was then recorded increasing the temperature at a constant rate until a certain temperature in order to study the different basic sites strength.

During all the analysis a carrier gas (argon in our case) flows in a stream trough the sample. A TCD monitors the signal which is proportional to the quantity of molecules desorbed as thermal energy. The graph usually is represented as TCD signal vs. temperature [Webb 2003, Geng 2009, Yeung 2004].

In catalysis, one of the main applications of TPD analysis is the study of basic and/or acid sites of catalysts. For the particular case of this thesis work, TPD analyses were performed in order to study the basicity of the catalysts [Chapter 5].

TPD analysis (Belcat-M, Bel Japan Inc) was performed after activating the sample (0.08 g) at 723 K for 1 h to eliminate adsorbed water. The instrument was located at the *UPC* facilities, in Barcelona (Spain). The desorption was recorded from 313 K to the temperature at which they were previously calcined, at 10 K/min after saturation of the sample with CO_2. Argon was used as carrier gas during activation and desorption steps. TPD tests were also performed without previous adsorption of CO_2 for comparison.

3.2.8 Inductively coupled plasma (ICP).

The technique uses a plasma as the atomization and excitation source. A plasma is an electrically neutral, highly ionized gas that consists of ions, electrons and atoms. Most analytical plasmas operate with argon or helium. Plasmas are characterized by their temperature, electron and ion densities. They operate in the range of 600 to 8000 K.

The energy that keeps the plasma is derived from an electric or magnetic field. Most ICP instruments use an induction coil to produce a magnetic field. It is wrapped two or three times around the ICP torch and has water flowing through it for cooling purposes.

Analytical atomic spectroscopy identifies elements and quantifies concentrations in various media. In order to have accurate results, interferences must be detected. Any chemical or physical process that affects the measurements of the radiation can be classified as interference. Those can come from sample preparation or at the plasma operating conditions (I.e. formation of undesired species). Spectral interferences can be minimized using a high resolution system by using several analytical lines for the detection of a single element [Manning *et al.* 1997, Meyers 2012].

The main applications of ICP analysis is that it can detect samples in concentrations of ppb of numerous metals in solutions. The samples can be analyzed in diluted solutions where the metals may be attacked by acids or even microwaves digestion. The most common type of analysis is the analysis of metal cations in an aqueous solution.

In this thesis, Mg/Al and Ca/Al ratios were analyzed in an ICP-OES analyzer (Induced Coupled Plasma – Optical Emission Spectroscopy) from Spectro Arcos. The instrument was located at the *Servei de Recursos Científics* of URV facilities. Calcined samples powders (50 mg) were solubilised with HNO_3 of 60 wt % (2 ml), heated if necessary, brought to 25 ml volume and finally 1 ml of the solution was diluted into 25 ml. Standards were used to perform calibration curves. All samples were analyzed by triplicate.

3.2.9 Sourcemeter for the characterization of I-V characteristics.

Intensity-Voltage measurements are acquired using sourcemeters, which are instruments that basically are able to source and measure at the same time.

For the particular case of light-emitting diodes (LEDs), plotting the ideal I-V characteristics of a diode, one would see zero current when V_D (diode voltage) is negative and infinite current when V_D tries to go positive. Ideally, a diode is a device that allows current to flow in one direction only. In practice, they allow large amounts of forward current to flow when the positive voltage across them reaches a small threshold. There is a small saturation current and a breakdown region in which a large amount of current will flow in the opposite direction when a large negative voltage is applied.

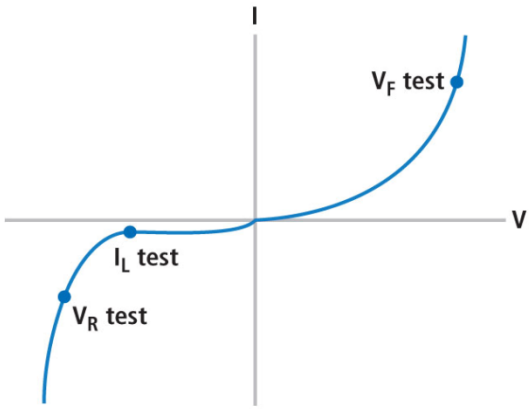

Figure 3.7. Typical LED I-V characteristics graph. V_R is the reverse voltage, V_F is the forward voltage and I_L is the minimum intensity at the *Zener* breakdown region. Image extracted from http://www.ledsmagazine.com

The diode equation is a good representation of the I-V characteristics (eq. 3.7):

$$i_D = I_S\,(e^{\wedge}(V_D/nV_T) - 1) \qquad \text{(eq. 3.7)}$$

where I_s is the saturation current, usually measured in micro or nanoA. V_D is the direct voltage, V_T is the thermal voltage and *n* is an arbitrary parameter which depends on construction. Figure 3.7 is a representative I-V graph for a LED. [Yu *et al*. 2010, Enderlein *et al.* 1997].

One of the main applications of sourcemeters is to test the electrical behaviour of devices. In order to test optoelectronic devices, it is useful to plot the voltage across the diode vs. the current through the diode. Electronic engineers determine basic parameters of a device and even to model an electrical circuit. The most simple I-V plot would be that of the transistor.

In this thesis, I-V characteristics were analyzed using a Keithley 2400 series Sourcemeter. The instrument was located at the *Nephos* facilities. The devices were analyzed using a sample holder, where up to 4 samples can be inserted. The metallic contacts are selected using a position wheel (each device sample has 4 diodes to be analized). A second position wheel selects the appropriate diode. The sample holder was connected to the sourcemeter. The instrument is used from a computer, attached to the instrument, with an appropriate software. The values that had to be chosen were: start voltage, stop voltage, step value, compilance, trigger delay and timeout. From the plot of the graph log *I* vs. log *V*, it is possible to determine the main conduction mechanism.

3.2.10 Light emission in semiconductors.

Band-to-band transitions in semiconductors.

In semiconductors, the process of light emission is called radiative recombination. In an excited semiconductor there will be holes near the top of the valence band and electrons near the bottom of the conduction band. Due to the presence of holes in the valence band, the electrons in the conduction band are in an unstable high-energy state. The holes in the top of the valence band constitute empty lower energy states that the electrons can fill; consequently electrons in the conduction band can release their extra energy and fill the vacancies in the valence band, recombining with the holes. The transition from a higher to a lower energy level results in an energy loss equal to the difference in energy of these levels (E_g fundamental transition). When this energy is released in the form of a photon, the process is called radiative recombination [Gallardo 2006].

Absorption and Photoluminescence in semiconductors.

The absorption spectra of nanocrystals are determined by the energy spectrum of electron-hole pairs. In nanocrystals with radii *a* smaller than the bulk exciton Bohr radius a_{exc}, these spectra are described by the transitions between quantum size levels of holes and electrons. Coulomb electron-hole interaction only shifts to the red at the energies of these transitions [Ekimov *et al*. 1993, Yu *et al.* 2010, Gauglitz*et al.* 2003, Méndez 2013].
In absorption spectrometry, the sample is illuminated with (quasi) monochromatic light of known intensity. This light interacts with the sample and the resulting intensity is collected and measured. The difference between the intensities before and after the interaction measures how much light was absorbed at the given wavelength. This measurement is then repeated for all wavelengths within the surveyed range. In semiconductors, there is an increase in absorption when the excitation energy approaches the value of the bandgap, because of the creation of electron-holes pairs. For exciting photons with an energy close to the ground excitation, the energy bandgap can be related to the measured absorption.
In photoluminescence spectrometry, the sample is excited with monochromatic light with a wavelength shorter than that associated with the first exciton. The material absorbs photons by creating electron-hole pairs. When the excitation is removed, the excitons relax, and a number of them release energy radiatively. The energy distribution of this emission constitutes the photoluminescence spectrum. A strong peak is detected at the first exciton energy, giving a direct measurement of the bandgap [Gallardo 2006].
In this work, optical measurements were made in order to detect the emission peak of the thiol-capped CdTe nanoparticles in the hybrid materials synthesized with optical properties and in the emissive layer of the light-emitting diodes. Also, the quantum dots were characterized in their solution form to determine their emission and absorption peaks.
Absorption measurements were performed using a Cary 5000, located at *Ficma-Ficna* facilities.

In this thesis, two fluorimeter instruments were used. At *Nephos* facilities, the instrument used was PTI Quantamaster 40, whilst at *Centro Nanosistemi* the instrument used was Fluorolog 3 Horiba Jobin-Yvon IBH-FL 322, with 450 W Xenon lamp and photomultiplayer R928 (Hamamatsu).

Samples were analyzed in 3 forms:

- liquid samples in a cubete.
- powder samples using a special powder-holder sample (at *Centro Nanosistemi*).
- glass substrates.

To record emission spectra the excitation wavelength was set and the emission spectra recorded between an appropriate range. A correction was applied to the spectra.

References for Chapter 3.

[Azzolina Jury *et al.* 2014] Azzolina Jury F., Polaert I., Estel L. and Pierella L. B. **2014**, *Enhancement of synthesis of ZSM-11 zeolite by microwave irradiation*, Micropor. Mesopor. Mater., 198, 22-28.

[Bashar 1998] Bashar S. A. **1998**, *Study of Indium tin oxide (ITO) for novel optoelectronic devices*, PhD Thesis, University of London, London, United Kingdom.

[Benito *et al.* 2006] Benito P., Labajos F.M., Rocha J. and Rives V. **2006**, *Influence of microwave radiation on the textural properties of layered double hydroxides*, Micropor. Mesopor. Mater., 94, 148-158.

[Bergadà *et al.* 2007] Bergadà O., Vicente I., Salagre P., Cesteros Y., Medina F. and Sueiras J.E. **2007**, *Microwave effect during aging on the porosity and basic properties of hydrotalcites*, Micropor. Mesopor. Mater., 101, 363–373.

[Bergadà *et al.* 2007b] Bergadà O., Salagre P., Cesteros Y., Medina F. and Sueiras J.E. **2007**, *Effective catalysts, prepared from several hydrotalcites aged with and without microwaves, for the clean obtention of 2-phenylethanol*, Appl. Catal. A Gen., 331, 19-25.

[Bergadà *et al.* 2007c] Bergadà O., Salagre P., Cesteros Y., Medina F. and Sueiras J.E. **2007**, *Adsorption of Carbon Dioxide in Several Aged Hydrotalcites and Calcined Hydrotalcites: Influence of Microwave Irradiation during the Ageing Step on their Basic Properties*, Adsorpt. Sci. Technol., 25, 143-154.

[Bogner *et al.* 2007] Bogner A., Jouneau P.-H., Thollet G., Basset D. and Gauthier C. **2007**, *A history of scanning electron microscopy developments: towards "wet-STEM" imaging*, Micron, 38, 390-401.

[Boothroyd 2010] Boothroyd C.B. **2010**, *Microanalysis in the electron microscope*, lecture notes at Technical University of Denmark.

[Bozzola *et al.* 1998] Bozzola J.J and Russell L.D. **1998**, *Electron Microscopy*, Jones & Bartlett Publishers, 2nd edition.

[Brewer Science websites] http://www.brewerscience.com/spin-coaters

[Brunauer *et al.* 1938] Brunauer S, Emmett P.H and Teller E. **1938**, *Adsorption of gases in multimolecular layers*, J. Am. Chem. Soc, 60, 309-319.

[Cheng 2005] Cheng J.-X. **2005**, *FTIR spectroscopy and imaging*, lecture notes at Purdue University.

[Coats *et al.* 1963] Coats A.W and Redfern J.P. **1963**, *Thermogravimetric Analysis*, Analyst, 88, 906-924.

[Chopra *et al.* 1983] Chopra K. L. and Kaur I. **1983**, *Thin film device applications*, Plenum Press, New York.

[Cullity 2001] Cullity, B.D and Stock, S.R. **2001**, *Elements of X-Ray diffraction*, Prentice Hall, 3rd edition.

[Dabrowski 2001] Dabrowski A. **2001**, *Adsorption - from theory to practice*, Adv. Coll. Inter. Sci., 93, 135-224.

[Danilatos 1981] Danilatos G.D. **1981**, *Design and construction of an atmospheric or environmental SEM (part 1)*, Scanning, 4, 9-20.

[Danilatos 1994] Danilatos G.D. **1994**, *Environmental scanning electron microscopy and microanalysis*, Microchim. Acta, 114/115, 143-155.

[De Graef 2003] De Graef M. **2003**, *Introduction to conventional transmission electron microscopy*, Cambridge Solid State Science Series, Cambridge University Press.

[Enderlein *et al.* 1997] Enderlein R. and Horing N.J.M. **1997**, *Fundamentals of semiconductor physics and devices*, World Scientific Pub Co Inc.

[Ekimov *et al*. 1993] Ekimov A.I., Kudryavtsev I. A, Efros A. L., Yazeva T. V., Hache F., Schanne-Klein M. C., Rodina A. V., Ricard D. and Flytzanis C. **1993**, *Absorption and intensity-dependent photoluminescence measurements on CdSe quantum dots: assignment of the first electronic transitions*, J. Opt. Soc. Am. B, 10, 100-107.

[Font 2006] Font M. **2006**, *La espectroscopía de Infrarrojo*, lecture notes at Universidad de Navarra.

[Fröberg 2010] Fröberg L. **2010**, *Thermal analysis TGA/DTA*, lecture notes at Åbo Akademi University.

[Gallardo 2006] Gallardo D. E. **2006**, *Dynamic effects in CdTe quantum-dot LEDs*, PhD thesis, Cranfield University, Cranfield, United Kingdom.

[García Martínez *et al.* 2003] García Martínez J. and Pérez Pariente J. **2003**, *Materiales zeolíticos: síntesis, propiedades y aplicaciones*, Textos Docentes, Publicaciones Universidad de Alicante.

[Garratt-Reed 2003] Garratt-Reed A.J and Bell D.C **2003**, *Energy-dispersive X-ray analysis in*

the electron microscope, Microscopy Handbooks, Garland Science.

[Gauglitz *et al.* 2003] Gauglitz G. and Vo-Dinh T. **2003**, *Handbook of spectroscopy* (2 vols), Wiley-VCH, 1st edition.

[Gedanken 2004] Gedanken A. **2004**, *Using sonochemistry for the fabrication of nanomaterials*, Ultrason. Sonochem., 11, 47-55.

[Geng 2009] Geng B. et al **2009**, *Temperature programmed desorption - an application to kinetic studies of CO desorption at electrochemical interfaces*, J. Phys. Chem. C, 113, 20152-20155.

[Hafner 2007] Hafner B. **2007**, *Scanning electron microscopy primer*, lecture notes at University of Minnesota.

[Hielscher website] www.hielscher.com/technolo.htm

[Jalili *et al.* 2004] Jalili N. and Laxminarayana, K. **2004**, *A review of atomic force microscopy imaging systems: applications to molecular metrology and biological sciences*, Mechatronics, 14, 907-945.

[Koch 2006] Koch C.T. **2006**, *Transmission electron microscopy*, lecture notes at Universität Stuttgart.

[Larkin 2011] Larkin P. **2011**, *Infrared and Raman Spectroscopy. Principles and spectral interpretation*. Elsevier.

[Laurell Technologies Corporation website] http://www.laurell.com

[Manning 1997] Manning T.J. and Grow W.R. **1997**, *Inductively Coupled Plasma - Atomic emission spectrometry*, 2, 1-19.

[Mbraun website] http://www.mbraun.com/products/coating-equipment/vacuum-deposition/

[Méndez 2013] Méndez M. **2013**, *Synthesis and characterization of down-shifting Ln^{3+} doped lanthanum-based nanoparticles for photovoltaic applications*, PhD Thesis, Universitat Rovira i Virgili, Tarragona, Spain.

[Meng *et al.* 2014] Meng X. and Xiao F.-S. **2014**, *Green Routes for Synthesis of Zeolites*, Chem. Rev., 114, 1521-1543.

[Metler Toledo Website] Metler Toledo website <www.us.mt.com>

[Meyer *et al.* 2003] Meyer E., Hug H.J. and Bennewitz R. **2003**, *Scanning Probe Microscopy: the*

lab on a tip, Advanced texts in Physics, Springer.

[Meyers 2012] Meyers R.A. **2012**, *Encyclopedia of Analytical Chemistry*, Wiley, 1st edition.

[Mokaya *et al.* 1997] Mokaya R., Jones W., Moreno S. and Poncelet G. **1997**, *n-heptane hydroconversion over aluminosilicate mesoporous molecular sieves*, Catal. Lett, 49, 87-94.

[Moore *et al.* 1997] Moore D.M and Reynolds R.C, **1997**, *X-Ray diffraction and the identification and analysis of clay minerals*, Oxford University Press, 2nd edition.

[Ortiz 2007] Ortiz C. **2007**, *AFM Imaging*, lecture notes at Massachusetts Institute of Technology.

[Othman *et al.* 2009] Othman M.R., Helwani Z., Martunus and Fernando W.J.N. 2009, *Synthetic hydrotalcites from different routes and their application as catalysts and gas adsorbents: a review*, Appl. Organometal. Chem. 23, 335-346.

[Pujol 2014] Pujol M.C. **2014**, *AFM*, lecture notes at Universitat Rovira I Virgili.

[Sánchez *et al.* 2013] Sánchez T., Salagre P. and Cesteros Y. **2013**, *Ultrasounds and microwave-assisted synthesis of mesoporous hectorites*, Micropor. Mesopor. Mater., 171, 24-34.

[Settle 1997] Settle F.A. **1997**, *Handbook of Instrumental techniques for analytical chemistry*, Prentice Hall.

[Stuart 1983] Stuart R. V. **1983**, *Vacuum technology, thin films and sputtering,* Academic Press, London.

[Thomas 2006] Thomas M. **2006**, *BET surface Area Analyzer*, lecture notes at Rice University.

[Trunschke 2007] Trunschke A. **2007**, *Surface area and pore size determination*, lecture notes at Fritz Haber Institute of the Max Planck Society.

[Vernon-Parry 2000] Vernon-Parry K.D. **2000**, *Scanning electron microscopy: an introduction*, III-Vs Review, 13, 40-44.

[Vernon-Parry 2001] Vernon-Parry K.D. **2001**, *TEM: an introduction - part 2*, III-Vs Review, 14, 48-51.

[Vicente *et al.* 2010] Vicente I. Salagre P. Cesteros Y. Medina F. and Sueiras J. E. **2010**, *Microwave-assisted synthesis of saponite*, Appl. Clay Sci., 48, 26-31.

[Webb 2003] Webb P. **2003**, *Introduction to chemical adsorption analytical techniques and their applications to catalysis*, Micromeritics Technical Publications, 1-12.

[Williams et al. 2009] Williams D.B and Carter C.B. **2009**, *Transmission electron microscopy. Part 1: Basics*, Springer, 2nd edition.

[Yeung 2004] Yeung K. L. **2004**, *Adsorption and Catalysis*, lecture notes at Hong Kong University of Science and Technology.

[Yu *et al.* 2010] Yu P. and Cardona M. **2010**, *Fundamentals of semiconductors*, Graduate Texts in Physics, Springer, 4th edition.

[Zhou *et al.* 2006] Zhou W. and Wang Z. L. **2006**, *Scanning microscopy for nanotechnology*, Springer.

[Zur Loye 2013] Zur Loye H.-C. **2013**, *X-Ray diffraction*, lecture notes at University of South Carolina.

CHAPTER 4

Synthesis and characterization of CaAl layered double hydroxides & Delamination and reconstruction studies

4.1 Introduction.

As commented in the general introduction at Chapter 1, layered double hydroxides (LDH) have general formula $[M(II)_{1-x}M(III)_x(OH)_2]^{x+}(A^{n-}{}_{x/n})\cdot mH_2O$, where M(II) and M(III) are divalent and trivalent metals and A^{n-} an anion. They can be prepared in a variety of cations. For this particular work, M(II) is Ca^{2+}; the compound belongs to the hydrocalumite subgroup [Rousselot *et al*. 2002]. Hydrocalumite is a mineral of the CaAl layered double hydroxide family with chloride as anion.

Some LDH applications include: heterogeneous catalysts, catalysts supports, ion exchangers, flame retardant, absorbents, in medicine…

LDHs are commonly prepared by co-precipitation of inorganic salts in alkaline media either at constant or at increasing pH. For the preparation of LDHs, the method of pH variation is frequently used [Cavani *et al.* 1991, Othman *et al.* 2009]. However, as it will be explained in the next section, there are several methodologies to synthesize them.

4.1.1 Synthesis' routes for layered double hydroxides.

With the aim of synthesizing LDHs with controlled particle size, porosity and degree of crystallinity, there are different procedures reported in the literature [Othman *et al.* 2009].

- Co-precipitation: it is a well-know and commonly used method. Inorganic salts are added to an alkali solution, the metals will form the brucite-like layer in the form of hydroxides, whilst the anions along with water molecules will define the interlayer space. When the pH is kept constant, the definition of pH is matter of importance: if it is too low not all the ions may precipitate in the solution. In general, the products are highly crystalline in conditions of low supersaturation. In contrast, high supersaturation uses high concentrations that imply formation of several nuclei. As a consequence, less crystalline materials are obtained [Occelli *et al.* 1992].
- Urea hydrolysis: the process uses urea as precipitating agent, in opposition to NaOH (co-precipitation method). With urea, hydrolysis is slow, which favors a low degree of saturation. Mixing urea with the nitrate salts of the metals leads to the precipitation of LDH. Temperature might be used as well. Other parameters that might be modified are metal concentration and urea/metal ratio. In general, crystallinities are good using this methodology as well as the obtention of pure phases [Ogawa *et al.* 2002].
- Combustion synthesis: it is a quick methodology. A fuel is used (saccharose, for example), that will exothermically decompose after heated in the presence of mixed oxides (no solvent is used) and in the presence of sodium carbonate. A good degree of crystallization is obtained at shorter times (5 min) compared to other techniques [Patil *et al*. 2002, Dávila *et al*. 2008].
- Sol-gel: it is used because of the facility to control structural properties of the LDH and because of the high purity of the obtained material. The process involves metal precursors to be hydrolyzed and an acid or base. Full methodology may be found published elsewhere

[Aramendía *et al*. 2002]. Thin films may be obtained, which are on demand and have many applications. High surface areas may be obtained using this method, which makes them interesting depending the properties wanted.

- Reconstruction from the mixed oxides: another methodology commonly used to synthesize LDH is the reconstruction of the mixed oxides (of the desired metals) in the presence of water and the appropriate anion. This is possible because of the *memory effect*. Until a certain temperature of calcination, the mixed oxides can be reconstructed and form a layered structure. This methodology is later further explained.

After the LDH have been synthesized, a hydrothermal treatment can be applied in order to achieve good crystallinities, applying temperature and in the presence of water vapor (temperature and pressure are the main variables). In general, temperatures higher than 473 K are not used. This pressurized media is going to vary the morphology of the platelets, arising a better hexagonal shape typical for this kind of materials [Othman *et al.* 2009].
In this work, the precipitation method has been performed at low supersaturation: slow addition of the metals and alkali solutions. After LDH synthesis, a hydrothermal aging step has been applied to the LDHs, using reflux or autoclave as recipients, and using conventional or microwave radiation as heating sources. The use of microwave radiation is explained in Chapter 3.

The use of microwave irradiation during the aging treatment of inorganic materials reduces enormously aging times but also provides much more crystallinity in the final material, as observed when applied to the synthesis of zeolitic materials and LDHs [Ayala *et al*. 2011, Benito *et al*. 2006, Bergadà *et al.* 2007, Stoeger *et al*. 2012] or in the preparation of clays (hectorites and saponites among others), where aging times have been remarkably decreased [Sánchez *et al.* 2012, Trujillano *et al.* 2010, Vicente *et al.* 2010].

4.1.2 Methodologies for CaAl layered double hydroxide synthesis.

CaAl-LDHs are a subgroup of layered double hydroxides where the divalent metal is calcium and the trivalent one usually aluminum. Iron can also be found in some CaAl-LDHs. A number of anions can form the interlayer space, for the most common a specific nomenclature applies to them. This is the case for Friedel's salt and Kuzel's salt, with chloride and sulfate, respectively.
For the particular case of this work, two kinds of CaAl-LDH have been synthesized, with chloride and nitrate as anions. The different interlayer anion will predominantly affect to the unit cell parameters, and thus, to the interlayer distance. This variation in interlayer distance will affect the swelling and ion-exchange capacities [Balonis 2010, Kuzel *et al*. 2011].
The most common synthetic procedure is the co-precipitation of Ca & Al salts at constant pH followed by an aging treatment at room temperature or by conventional heating. In the next table (Table 4.1) some conditions reported in the literature are summarized.

Table 4.1. Examples in the literature of HC synthesis through co-precipitation.

Authors	Type of anion	Aging treatment	
		T (K)	time (h)
Radha *et al.* [Radha *et al*. 2005]	NO_3^-	338	18
Campos-Molina *et al.* [Campos-Molina *et al.* 2010], Vieille *et al.* [Vieille *et al.* 2003]	Cl^-	333-338	24
Grover *et al.* [Grover *et al*. 2010]	Cl^- and NO_3^-	RT	24
Domínguez *et al.* [Domínguez *et al.* 2011]	Cl^-	RT	48

However in the literature different methods have been described. Sánchez-Cantú *et al.* prepared CaAl-LDH from purchased hydrated lime (CaO) and boehmite (□-AlO(OH)) [Sánchez-Cantú *et al.* 2013]. The aqueous media where the addition took place was slightly acidified with HNO_3; to reach a basic pH of 12,5 ammonium hydroxide was added. The authors claimed that this was a greener methodology for synthesizing CaAl-LDH. However, it was possible to identify boehmite and calcite phases in the final product (calcite was detected in the starting reagent). Kuwahara and co-workers re-used blast furnace slag as precursor to obtain CaAl-LDH [Kuwahara *et al*. 2010]. This methodology is very interesting because it seeks to recycle an industrial waste, blast furnace slag, which is produced in the iron industry at a rate of 290 kg/ 1 ton of pig iron. It is formed by CaO, SiO_2, Al_2O_3, MgO and some transition metals. They could identify the CaAl-LDH phase as product, but some transition metals were incorporated in the structure. The synthesis was performed by acid-leaching and precipitation processes and from pH=9 CaAl-LDH phase was identified in all samples.

A methodology was reported by Cota and co-workers, who performed the synthesis by the hydrolysis reaction of the calcium and aluminum alkoxides [Cota *et al*. 2010]. They performed the aging treatment at different temperatures (273, 298 and 333 K) to check the influence in the crystallinity. However, gibbsite and katoite phases were also found in the diffractograms. Zhang and co-workers have optimized the modification of experimental variables such as pH, time, temperature and solvent for the production at a large-scale for the cement industry [Zhang *et al.* 2011]. They found the best results for samples aged at 343 K for 24 h that later were successfully scaled-up using SNAS (separate nucleation and aging steps) method at pH in the range of 10.5-11.5.

Recently, Pálinkó and co-workers studied the intercalation of carbonate species during the synthesis and drying of two kind of CaAl-LDHs, one prepared by co-precipitation and the other by a modified version of the co-precipitation technique, where the alkaline solution contained the

aluminum [Tóth *et al.* 2014]. Some samples were additionally prepared in the presence of the carbonate anions. Different drying methods where studied to optimize the process. Calcite did not appear in any sample and synthesis of the carbonate CaAl-LDHs were successful and with no other phase in the X-Ray diffractograms. With the aim of synthesizing precursors to obtain graphene-inorganic composites, Dekany and co-workers synthesized hydrocalumite from tricalcium aluminate and added nanosheets of graphene oxide, by reconstruction in aqueous media [Plank *et al*. 2014]. They obtained a CaAl-LDH with graphene oxide in the interlayer space. They tested as well the exchange capacity of this compound with sulfate anions and ettringitte ($Ca_6Al_2(SO_4)_3(OH)_{12}\cdot 26H_2O$) was formed.

4.1.3 Methodologies for LDH delamination.

Delamination can be achieved with the use of particular solvents; many appear reported in the literature. Adachi-Pagano and co-workers first delaminated LDHs intercalated with surfactants like dodecyl sulphate (LDH-DDS) in the presence of butanol, refluxing for 16 h at 393 K [Adachi-Pagano *et al*. 2000]. Jobbágy and Regazzoni studied exfoliaton of LDH-DDS with CCl_4 [Jobbágy *et al.* 2004] whereas Naik *et al.* performed the same process in toluene [Naik *et al.* 2011]. Hibino *et al.* have studied the role of formamide as solvent and were the first to report delamination of LDH in formamide at room temperature [Hibino *et al.* 2001]. They investigated several solvent combinations and found the system LDH-glycine along with formamide the most successful. Lately, in another study, they tested other amino-acids and several polar solvents [Hibino 2004]. Several authors reported then the use of formamide for delaminating some LDHs along with the use of mechanical stirring or the use of ultrasounds was also possible [Li *et al*. 2005, Wu *et al.* 2007, Liu *et al.* 2006, Palomares *et al*. 2012].
Gordijo *et al.* reported that Mg-Al-CO_3 LDH can be exfoliated with a mixture of ethanol:N,N-dimethylformamide [Gordijo *et al.* 2007]. Leroux and co-workers studied the exfoliation of LDHs in polyester aiming at polymer nanocomposite applications [Swanson *et al.* 2013]. Even though the procedure was performed with air, no carbonate phase was detected. Interestingly, an important number of publications have arisen seeking for the synthesis of nanocatalysts from exfoliated LDHs. To the best of our knowledge, there are no studies reporting CaAl-LDH delamination.

4.1.4 Methodologies for the reconstruction of calcined LDHs.

Another method to obtain LDHs is the reconstruction of calcined LDHs, which has been widely studied. After calcination at moderate temperatures (in the range 673-873 K), the layered structure of LDHs collapses, resulting in a mixture of the metal oxides and the removal of anion and water content as gases [Cavani *et al*. 1991]. Because of the so-called *memory effect*, in the presence of water calcined LDH can be rehydrated and be reorganized in a layered structure again [Abelló *et al*. 2005, Xu *et al*. 2013, Sharma *et al.* 2010].

Valente and co-workers studied the thermal decomposition and reconstruction processes of LDHs [Valente *et al*. 2010]. They prepared LDHs by two methodologies, from sol-gel and co-precipitation processes. After studying the reconstruction of these samples, they found that a decrease in the particle size was not always obtained, contrary to the expected tendency of the particle decrease. They claimed that the properties of the reconstructed materials depended mainly on the conditions used for reconstruction. Abelló and co-workers fastly synthesized reconstructed LDHs using sonication [Abelló *et al*. 2005]. They tested the reconstructed materials for the aldol condensation reaction. Álvarez and co-workers studied LDHs that were reconstructed by sonication [Álvarez *et al.* 2013]. They studied the changes in the crystallinities and the acid-basic properties of the active sites compared to the as-synthesized ones.

Reconstruction of LDHs has been widely used for applications that range from catalysts synthesis to adsorbents and many more applications. Tao and co-workers synthesized silylated LDHs thorough reconstruction of calcined LDHs without the use of any surfactants [Tao *et al.* 2010]. Zhao and co-workers compared the properties of as-synthesized and reconstructed LDHs with europium to detect changes in the luminescence properties. They reconstructed the calcined LDH using mechanical stirring in the presence of water [Zhao *et al*. 2012]. Pavel and co-workers compared the memory effect of catalysts based on calcined LDH for the cyanoethylation reaction [Pavel *et al*. 2010]. They also studied the elimination of the aging step after LDH synthesis and how it affected the memory effect for catalysts that were used for the same reaction, previously mentioned [Pavel *et al*. 2011]. More recently, Lee and co-workers used reconstructed LDHs for the isomerization reaction of glucose to fructose [Lee *et al*. 2014]. They compared catalysts reconstructed by sonication at different times and by mechanical stirring. For the particular case of CaAl-LDHs, the rehydration of tricalcium aluminate ($3CaO{\cdot}Al_2O_3$), an important phase in Portland cement, is a common route to synthesize them.

4.2 Aims of this chapter.

The aims of this chapter are:

- To synthesize several CaAl-LDHs with chloride as anion using different aging techniques, in order to study the effect over the crystallinity. In order to perform a cost-saving process in terms of energy consumption, microwave irradiation has been used along with conventional heating, in autoclaving or refluxing.

- To synthesize CaAl-LDHs with chloride and nitrate as anions in order to study their delamination behavior. Two delamination procedures were compared: in the presence of formamide using mechanical stirring, and the other procedure using ultrasounds in repeated cycles. The CaAl-LDHs were calcined and reconstructed in aqueous media in the presence of one of the following salts: NaCl or $NaNO_3$. Delamination tests were also performed to reconstructed samples, following as well the two procedures mentioned above, using mechanical stirring and ultrasounds in the presence of formamide.

- To synthesize a hybrid material of CaAl-LDH and thiol-capped CdTe nanoparticles by rehydration of a calcined CaAl-LDH.

4.3 Experimental procedure.

4.3.1 Chloride CaAl-LDH synthesis.

Several CaAl-LDHs were synthesized by co-precipitation method at constant pH [Vieille *et al.* 2003] with a Ca/Al molar ratio of 2 and Cl^- as anion. In a typical synthesis, the samples were prepared with vigorous stirring, under N_2 atmosphere and using decarbonized water to prevent from $–CO_3^{2-}$ incorporation. A solution of 250 ml ethanol/water mixture (2:3 v/v) was placed into a 500 ml 4-neck round-bottom flask in an oil bath at 333 K. A 100 ml solution with the salts was prepared by mixing the appropriate amounts of 0.66 M $CaCl_2{\cdot}2H_2O$ and 0.33 M $AlCl_3{\cdot}6H_2O$ solutions. Another solution of 2 M NaOH was used to keep pH constant at 11.5. The pH electrode and the two compensated pressure funnels for addition of the salts and the NaOH solution respectively, were connected to 3 of the necks of the round-bottom flask. N_2 was bubbled throw neck number 4 to avoid CO_2 incorporation.
After complete addition of the salts, several aging procedures were performed using conventional or microwave heating and reflux or autoclave as recipients (Table 4.2).

Table 4.2. Aging treatments for the synthesized hydrocalumites.

Nomenclature	Heating	Recipient	Temperature (K)	Time (h)
	Conventional/ Microwaves	Reflux/Autoclave		
$HCR_{24}(333)$	conventional	reflux	333	24
$HCR_3(353)$	conventional	reflux	353	3
$HCRMW_3(333)$	microwaves	reflux	353	3
$HCA_3(353)$	conventional	autoclave	353	3
$HCA_1(453)$	conventional	autoclave	453	1
$HCMW_1(353)$	microwaves	autoclave	353	1
$HCMW_6(353)$	microwaves	autoclave	353	6
$HCMW_1(453)$	microwaves	autoclave	453	1

Samples were named starting with letters HC, corresponding to CaAl-LDH, followed by letters R or A (refluxing or autoclave) for conventional heated samples and by RMW or MW (refluxing or autoclave) for microwaved samples. Finally, a number in subscript indicates the time of aging in hours whereas the number between parentheses is the temperature of aging. Additionally, another sample was synthesized at the same preparation conditions than those employed for synthesizing sample $HCRMW_3(353)$ but without using inert atmosphere during the hydrothermal treatment ($HCRMW_3(353)B$). This sample was characterized by XRPD and FT-IR spectroscopy

in order to detect the carbonate species bands. All samples were compared to HCR_{24}(333), which was aged as reported in literature [Vieille *et al.* 2003], by refluxing at 333 K for 24 h with conventional heating.

4.3.2 Nitrate CaAl-LDH synthesis.

The synthesis of a nitrate CaAl-LDH was also performed by co-precipitation method [Grover *et al.* 2010]. 50 ml of a mixed solution of the nitrate calcium and aluminum salts ($Ca(NO_3)_2{\cdot}4H_2O$ and $Al(NO_3)_3{\cdot}9H_2O$, respectively) was slowly drop-wised to 50 ml of 2M NaOH solution. N_2 was bubbled constantly to avoid carbonate incorporation. Decarbonized water was used as solvent. When the addition of the salts was completed, it was aged for 24 h at room temperature (RT). The selected Ca/Al ratio of the starting salts was 2. It was cleaned by centrifugation using decarbonized water and dried in an oven at 353 K overnight. This sample is labeled $HC\text{-}NO_3$.

4.3.3 Calcination of CaAl-LDHs.

Calcination was performed with synthetic air at 723 K for 8 h in a tubular furnace. The sample was placed in a quartz reactor. When calcination was completed, samples were stored in a desiccator. In an initial stage calcination was performed in a muffle under static air, but was later discarded since a phase attributed to $CaCO_3$ is present in the final product. For the reconstruction study, a chloride CaAl-LDH (sample HCR_{24}(333)) and the nitrate CaAl-LDH were calcined. Calcined samples are called $cHCR_{24}$(333) and $cHC\text{-}NO_3$.

4.3.4 Reconstruction of calcined nitrate CaAl-LDHs.

Rehydration was performed in an ultrasound bath, using a similar methodology to that published before [Abelló *et al.* 2005]. 0.25 g of sample was placed in a 2-necked round bottom flask with 50 ml of a 0.01 M solution of the suitable salt (either NaCl or $NaNO_3$ for each CaAl-LDH). The reconstruction was performed by refluxing the solution at 333 K for 2 h under an inert atmosphere of N_2. The solution was filtered and washed with ethanol. Finally, it was dried in an oven at 353 K overnight. In this work, the two calcined samples used for reconstruction studies were $cHCR_{24}$(333) and $cHC\text{-}NO_3$. The nomenclature for reconstructed samples is shown in Table 4.3.

Table 4.3. Reconstructed samples.

Reconstructed Sample	Calcined parent sample	Anion added in the reconstruction
rHC-Cl-Cl	$cHCR_{24}(333)$	chloride
rHC-Cl-NO_3	$cHCR_{24}(333)$	nitrate
rHC-NO_3-Cl	cHC-NO_3	chloride
rHC-NO_3-NO_3	cHC-NO_3	nitrate

4.3.5 Delamination process.

The following samples were used for delamination tests: $HCR_{24}(333)$, HC-NO_3, rHC-Cl-Cl, rHC-Cl-NO_3, rHC-NO_3-Cl and rHC-NO_3-NO_3.
Samples were diluted in formamide at a concentration of 1 mg/ml. Delamination was performed in a similar procedure to that of Palomares *et al.* [Stoica *et al.* 2012]: in an ultrasound bath at RT in cycles of 30 min of ultrasonication followed by 50 min of rest. Between 6 and 8 cycles were needed. In parallel, samples were also agitated vigorously for 2 days at RT, using a mechanical shaker, in a purged and sealed Erlenmeyer, as described before [Ma *et al.* 2006], in order to compare these methods.

4.3.6 Synthesis of a hybrid CaAl-LDH with thiol-capped CdTe nanoparticles.

A CaAl-LDH was synthesized with thiol-capped CdTe nanoparticles from reconstruction of a calcined sample, following the procedure explained in section 4.3.4. The synthesis started from sample $cHCR_{24}(333)$, a solution of 0,01 M ammonium thioglycolate (linear formula: $HSCH_2COONH_4$) and 250 µl of the thiol-capped CdTe colloidal solution were added. The sample was recovered by centrifugation at 4000 rpm and stored in a desiccator.

4.3.7 Characterization techniques.

The characterization techniques used in this chapter along with the working conditions are further explained in Chapter 3 of this thesis. For this particular chapter, some particularities are described here:

- Tyndall effect: In order to characterize delamination, Tyndall effect was tested using a laser beam. Delamination was fully accomplished when the solution remained transparent and the laser beam went through the solution of the glass container, usually a 50 ml beaker.
- AFM microscopy: Delaminated samples were characterized by AFM microscopy. In order to prepare the samples, samples were dropped in a Si wafer by spin coating at 4500 rpm for 1 min.

- Optical measurements: A solid sample holder has been used in the instrument to record the emission spectra. The measurements were done at the facilities of *Centro Nanosistemi* in Alessandria, Italy.

4.4 Results and discussion.

4.4.1 Chloride CaAl-LDHs aged with different conditions.

Figure 4.1 and 4.2 show the XRPD patterns of all samples.

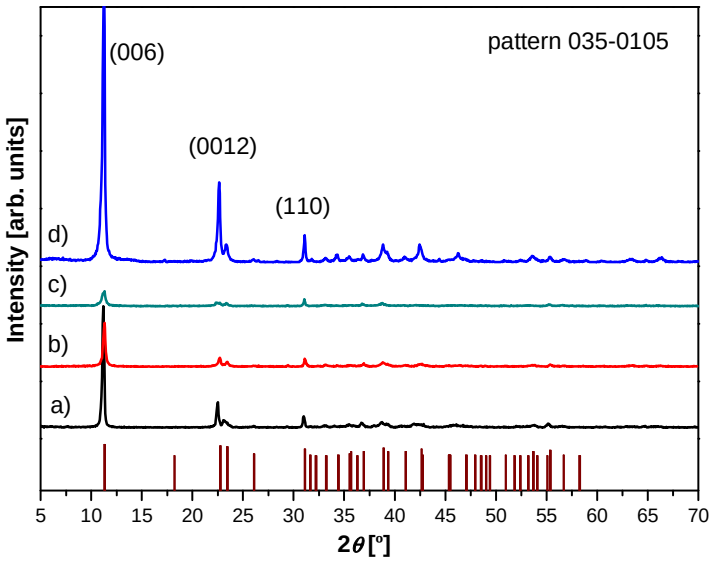

Figure 4.1. XRPD of the samples synthesized by conventional heating a) HCR_{24}(333), b) HCR_3(353), c) HCA_1(453) d) HCA_3(353). CaAl-LDH pattern: [JPDCS file: 035-0105].

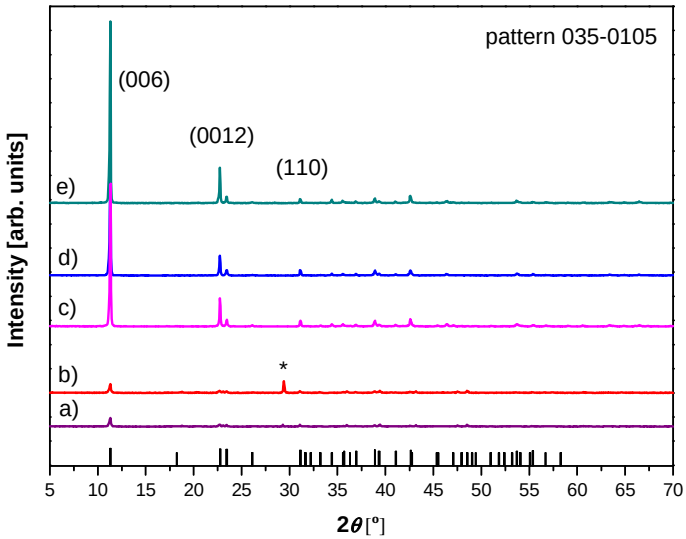

Figure 4.2. XRPD of the samples synthesized by microwaves irradiation a) HCRMW3(353), b) HCRMW3(353)B, c) HCMW6(353), d) HCMW1(353), e) HCMW1(453). CaAl-LDH pattern: [JPDCS file: 035-0105], *: calcite characteristic peak at 29.41º.

All reflections belonged to the same crystalline phase, which was identified as hydrocalumite (HC) by comparison with the corresponding JCPDS file [035-0105]. This is a layered compound with formula $[Ca_2Al(OH)_6]Cl{\cdot}2H_2O$, the structure of which is indexed in the trigonal lattice system and belongs to group *R*3*c* (No. 161) with theoretical ***a*** and ***c*** parameter values of 5.74 and 46.85 Å, respectively. The layered structure is built by the periodical stacking of positively charged $(Ca^{2+}, Al^{3+})(OH)_6$ octahedral layers and negatively charged interlayers with chloride and water molecules [Rousselot *et al.* 2002]. As observed in the diffraction patterns, the stacking direction is along crystallographic ***c*** direction, since the samples present a strong preferential orientation, showed by the high intensity of the (006) and (0012) peaks.

Additionally to the hydrocalumite phase, calcite was identified for sample $HCRMW_3$(353)B by comparison with the calcite JCPDS file [083-0577], which showed a typical intense peak at 29.41º (Fig. 4.2b). The presence of calcite phase in this sample, that was prepared without N_2 atmosphere, confirmed that the use of inert atmosphere during synthesis was necessary to obtain hydrocalumites as the only one crystalline phase.

The crystallite size along the stacking direction was calculated for (006) peak from the net integral breadth of the reflections, β_i, according to the following formula that comes from the Scherrer equation. This information is interesting in order to compare the growth rate for the different aging processes used.

Table 4.4 shows the crystallite size along the stacking direction and the FWHM of (110) reflection for all samples.

Table 4.4. Crystallographic characterization of the samples.

Sample	Crystallite size (006) (nm)	FWHM (º) (110)	a (Å)	c (Å)
HCR_{24}(333)	48	0,21	5,75	47,38
HCR_3(353)	41	0,20	5,74	47,35
$HCRMW_3$(353)	50	0,20	5,75	47,05
HCA_3(353)	42	0,16	5,74	47,17
HCA_1(453)	46	0,16	5,75	47,15
$HCMW_1$(353)	72	0,16	5,74	47,00
$HCMW_6$(353)	76	0,15	5,74	46,92
$HCMW_1$(453)	76	0,15	5,74	46,99

The crystallite size was related to the crystal growth rate in the stacking direction. In contrast, the crystallite size in the lamellar plane cannot be determined from Scherrer equation using the FWHM of (110) reflection, because, as commented later in TEM results, they are micrometric and the Scherrer equation is restricted to crystallites smaller than 500 nm [Cullity *et al.* 2001]. However, the values of FWHM for (110) peak can be used to compare the crystallinity of the samples (Table 4.4), since a decrease of FWHM values involves an increase of crystallinity [Cullity *et al.* 2001].

Hydrocalumites aged using microwave irradiation by refluxing or in autoclave showed larger crystallite sizes along the stacking direction than those aged by conventional heating under the same conditions. The largest values (72-76 nm) corresponded to samples synthesized in autoclave by microwaves ($HCMW_1$(353), $HCMW_6$(353) and $HCMW_1$(453)). Regarding samples aged by refluxing, it was also possible to observe the positive effect of microwave heating. Sample $HCRMW_3$(353) showed higher crystallite size (50 nm) after 3 h of aging compared to the conventional ones aged for 3 and 24 h (41 and 48 nm, respectively). Samples aged in autoclave by conventional heating exhibited values of crystallite size in the stacking direction (42 and 46 nm for samples HCA_3(353) and HCA_1(453), respectively) that were close to the crystallite size of sample aged conventionally by refluxing for 24 h (48 nm) (Table 4.3). This means that with autoclave under conventional heating (at 453 K for 1 h or at 353 K for 3 h), similar crystal growth can be obtained in less time. Therefore, microwave heating and autoclave increase crystal growth in the stacking direction.

Comparing the values of FWHM corresponding to reflection (110), the highest values (0.21-0.20º) corresponded to samples aged by refluxing using conventional or microwave heating. Therefore, the use of different heating method does not affect significatively the crystallinity of the layer when refluxing was used. The range of FWHM values for samples prepared with autoclave for conventional or microwave heating is 0.16-0.15º, which is slightly lower than that obtained for the samples aged by refluxing (0.21-0.20º). Thus, higher crystallinity was observed by using autoclave in comparison with refluxing. Among the samples aged by autoclave, slightly higher crystallinity was achieved with microwave irradiation. Therefore, samples aged using autoclave together with microwave heating were the most crystalline.

In conclusion, autoclave and microwave irradiation enhances a faster production of more crystalline lamellae at a lab-scale. Because of the faster synthesis, the absence of other phases and the higher degree of crystallinity, the conditions of synthesis of $HCMW_1(453)$ were found to be the most optima.

The lattice parameters of our synthesized samples ***a*** and ***c*** were calculated using literature equations [Gay 1972, Moore *et al.* 1989], from d_{110} and d_{006}, respectively (Table 4.4). Lattice parameter ***a*** is related to the isomorphic substitution between Ca^{2+} and Al^{3+}, whereas ***c*** parameter depends on the charge and size of the anion between the brucite layers [Cavani *et al.* 1991]. The fact that all values of ***a*** were practically the same for all hydrocalumites (Table 4.4) should be related to a similar stoichiometry for all samples. The same argument could be applied to ***c*** values. In this case, with the same number and type of anion, the slight differences observed in ***c*** values (Table 4.4) can be attributed to some differences in the hydration degree.

FT-IR spectra of all synthesized samples were very similar, showing the typical bands of these kind of layered double hydroxides [Domínguez *et al*. 2011, Mora *et al*. 2011], summarized in Table 4.5. Figure 4.3a shows the IR spectum of sample $HCMW_1(453)$ as a representative sample.

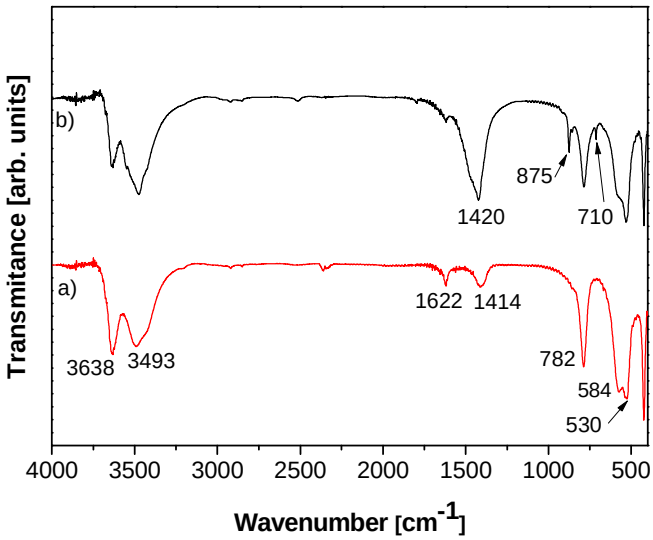

Figure 4.3. FTIR spectra of samples a) $HCRMW_3(353)$ aged with inert atmosphere, b) $HCMW_1(453)B$ aged without inert atmosphere.

Table 4.5. IR band assignations of the HC synthesized in the present work.

Band identification	*v* (cm^{-1})
OH stretching (AlO-H)	3638
OH stretching (CaO-H)	3493
deformation mode of water molecules	1622
C=O stretching	1414
metal-OH bonds	782
metal-OH bonds	584
metal-OH bonds	530

According to the literature, it was possible to observe in the region 3000-3750 cm^{-1} a broad band centered around 3500 cm^{-1} with peaks that are assigned to stretching vibrations of CaO-H (3490 cm^{-1}) and AlO-H (3634 cm^{-1}). In the region between 500 and 800 cm^{-1} three intense peaks, characteristic of metal bonds M-OH were also present. Additionally, in the region between 1400 and 1650 cm^{-1} one characteristic band, centered at 1620 cm^{-1} was observed. This band is assigned to deformation vibrations of water molecules. Finally, a small band around 1420 cm^{-1} was also observed in all spectra. This band could be related to some carbonation of the sample, since this band corresponds to the C=O anti-symmetrical stretching of the carbonate species. Taking into account the low intensity of this band, probably carbonation only takes place in the external surface of the particles during sample manipulation [Cota *et al*. 2010], since calcite was not detected by X-Ray powder diffraction, as previously commented.

In contrast, in figure 4.3b, IR spectrum of the sample $HCRMW_3$(353)B showed the effect of the absence of inert atmosphere during the synthesis and aging treatment of hydrocalumites, since a significant increase of the intensity of the band at 1420 cm^{-1}, corresponding to carbonate species, was observed. Additionally, it was also possible to identify other characteristic bands related to carbonates, at 710 cm^{-1} (bending angular) and at 875 cm^{-1} (bending non-planar). This agrees with the presence of calcite identified in this sample by XRPD.

Table 4.6. ICP and Physisorption results of the hydrocalumites synthesized in the present work.

Sample	Ca/Al molar ratio	BET specific surface area (m^2/g)	Microporous area (m^2/g)	Average pore radius (nm)
HCR_{24}(333)	1,99	9	1,52	18,3
HCR_3(353)	1,94	18	0,37	15,2
$HCRMW_3$(353)	2,00	7	0,21	14,8
HCA_3(353)	2,00	15	0,19	14,5
HCA_1(453)	1,95	12	0,32	11,9
$HCMW_1$(353)	1,88	5	0,26	13,0
$HCMW_6$(353)	1,87	5	0,42	16,9
$HCMW_1$(453)	1,84	2	0	10,1

Table 4.6 shows the values corresponding to Ca/Al molar ratio measured by ICP. These values are near to 2 for all samples. Therefore, with the different aging treatments it was possible to obtain hydrocalumites with the expected stoichiometry, in agreement with the reagents ratio used.

Adsorption/desorption isotherms were of type IV, according to IUPAC classification, corresponding to mesoporous materials, for all synthesized hydrocalumites with hysteresis loop type H3, associated to aggregates of plate-like particles leading to slid-shaped pores [Cota *et al*. 2010]. BET specific surface area, microporous area, determined by t-plot method, and average pore radius values are given in Table 4.6. All samples presented low BET area and negligible measured values of microporosity, mainly due to the fact that the internal area in the interlayer space cannot be measured due to the restriction for N_2 adsorption in this space. However, BET area values can be related to the crystallinity of the samples. Thus, lower BET area values (2 and 5 m^2/g) were obtained for the more crystalline samples, which were those prepared with microwave irradiation in autoclave. Average pore radius values, determined by BJH method, were between a maximum of 18.3 nm for $HCR_{24}(333)$ and a minimum of 10.1 nm for $HCMW_1(453)$. However, for the rest of samples, we did not observe a direct correlation between the average pore radium and crystallinity [Campos-Molina *et al.* 2010, Domínguez *et al*. 2011].

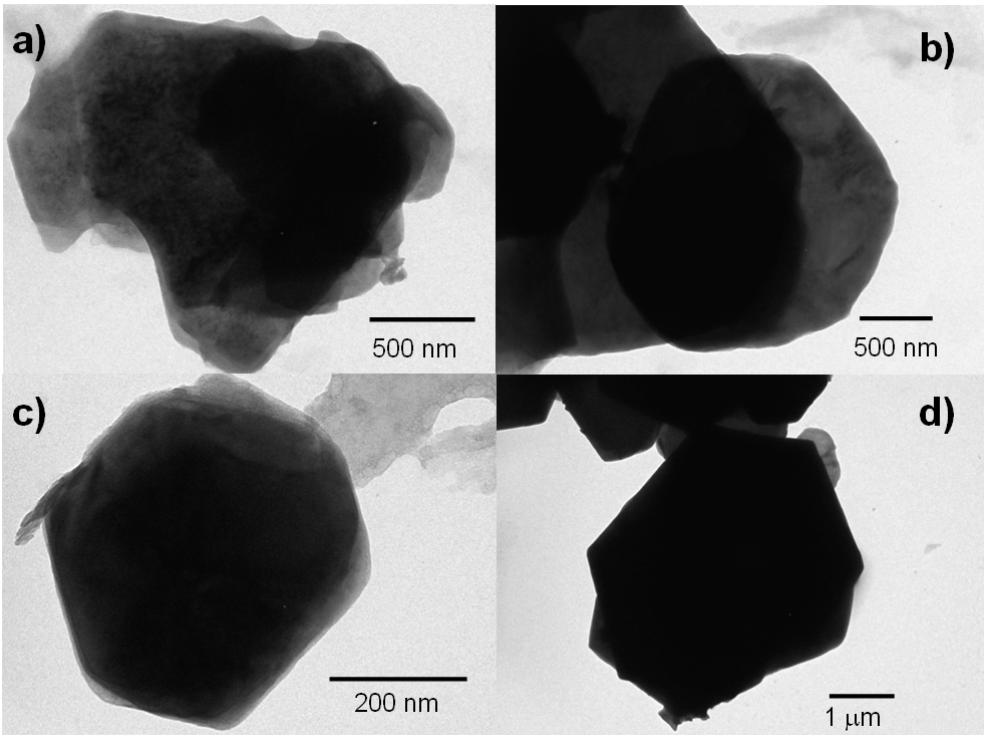

Figure 4.4. TEM micrographs of samples a) $HCR_{24}(333)$, b) $HCA_3(353)$, c) $HCMW_1(353)$ and d) $HCMW_1(453)$.

TEM micrographs of all synthesized hydrocalumites (Figures 4.4 and 4.5) showed lamellar structures with aggregated large particles as observed by the dark color of the sheets. Sample HCR_{24}(333) (Fig. 4.4a), which was aged with conventional heating under 24 h of refluxing, presented less defined hexagonal shape and very heterogeneous lamellar size distribution. This can be related to its lower crystallinity that is a consequence of the aging conditions. In contrast, sample HCA_3(353) (Fig 4.4b), which was aged by conventional heating in autoclave, exhibited a best definition of the hexagonal shape with more homogeneous lamellar sizes and width values between 350 and 800 nm.

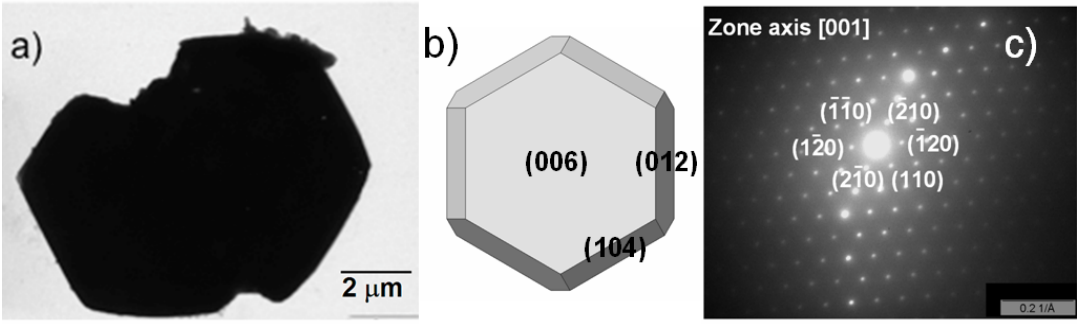

Figure 4.5. a) TEM micrograph of sample $HCMW_1$(453), b) morphology of hydrocalumite, c) electron diffraction pattern.

Samples that were fast aged under microwave irradiation $HCMW_1$(353) (Fig. 4.4c) and $HCMW_1$(453) (Fig. 4.4d) showed very well defined hexagonal lamellae with larger sizes and width values around 1.6 µm for $HCMW_1$(353) and 4 µm for $HCMW_1$(453). In fact, this sample presented the lowest value of FWHM for the peak (110) and the lowest BET specific surface area.

Figure 4.5 shows electron diffraction pattern with the presence of six equivalent reflections corresponding to (110) and equivalents (Fig. 5.5c) for sample $HCMW_1$(453) (Fig. 5.5a). The electron diffraction pattern indicates a highly crystalline sample, in agreement with the XRPD results and according to the defined hexagonal morphology for hydrocalumites. Using the *Shape* utility that applies the Wulff theorem R(hkl), it has been modelized the crystal habit and indexed the faces (Fig. 5.5b). In conclusion, the morphology, the crystallinity and the size of particles depended on the aged conditions used.

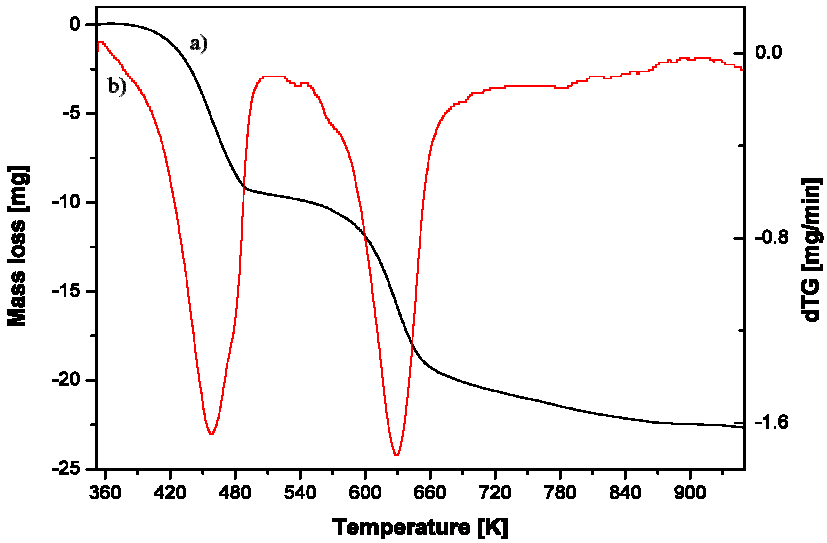

Figure 4.6. Thermal decomposition of hydrocalumite $HCMW_1$(453). a) mass loss, b).first derivative of mass loss.

Figure 4.6 shows a representative thermogram of the synthesized hydrocalumites, which was recorded from 353 to 1000 K after an isotherm of 30 min to exclude humidity adsorbed in the surface of the samples. We can observe 3 of the 4 expected steps [Domínguez *et al.* 2011]: i) dehydration of interlamellar water, ii) dehydroxylation of the layers, iii) and iv) anion decomposition. Due to the instrument safety limitations it was not possible to rise temperature to see completion of the anion decomposition. For all hydrocalumites, the first and second steps were well defined in the TGA curves and the values of mass loss were those expected: dehydration (12.8 %) and partial dehydroxylation (16 %), according to the decomposition steps proposed in the literature [Domínguez *et al.* 2011]. The % of the second step was lower than that corresponding to the total dehydroxylation (19.2 %). This was related to the formation of CaOHCl together with CaO and Al_2O_3 in the 2:2:1 ratio [Domínguez *et al*. 2011]. Respect to anion decomposition, the mass loss value obtained was lower than 13 %, since higher temperatures than 1000 K are necessary for total anion decomposition.

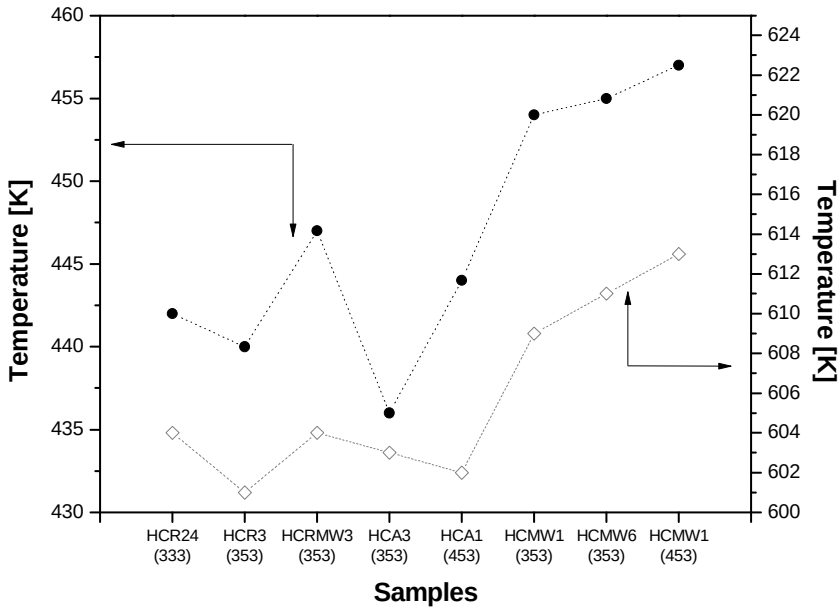

Figure 4.7. Temperatures of the maximum mass loss rate for the derivative of first and second steps in the thermal decomposition of synthesized samples. In black filled circles, temperature of dehydration step. In white filled rhombus, temperature of partial dehydroxylation step.

Figure 4.7 depicts the temperatures of the maximum mass loss rates corresponding to the first and second TGA steps for all samples (dehydration and dehydroxylation, respectively). The values of the temperature for the dehydration step were in the range 436-457 K. The highest values were obtained for the most crystalline samples ($HCMW_1$(453), $HCMW_6$(353) and $HCMW_1$(353)). A higher order in the stacking direction can suppose stronger interactions for the interlamellar water, and consequently, higher temperatures should be necessary to remove it. With respect to the second mass loss, which corresponds to dehydroxylation, the temperature of the maximum mass loss rate was similar for all samples (601-613 K). However, again, the highest values were observed for the samples prepared using microwaves in autoclave. These samples presented larger lamellar size, as observed by TEM and higher crystallinity of the lamellas in agreement with the XPRD results.

4.4.2 Delamination and reconstruction studies.

CaAl-LDHs and calcined CaAl-LDHs.

Thorough XRPD technique it was possible to identify CaAl-LDH phase for the two as-synthesized CaAl-LDHs HCR_{24}(333) and HC-NO_3.

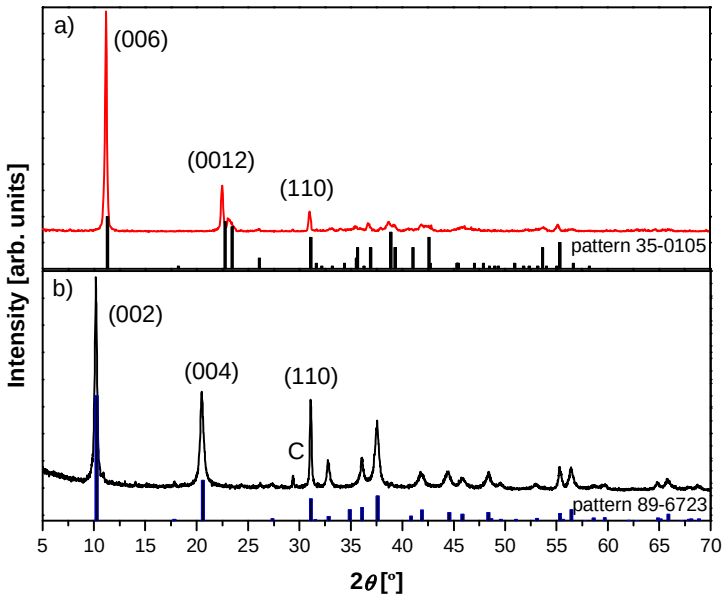

Figure 4.8. XRPD diffractograms of samples a) HCR_{24}(333) and b) HC-NO_3. The reflection labeled with C is due to an extra-phase of calcite.

Figure 4.8 shows the XPRD patterns for samples HCR_{24}(333) (Fig. 4.8a) and HC-NO_3 (Fig. 4.8b), respectively. The diffractograms are compared to the JCPDS files [035-0105] and [089-6723], respectively. Both samples belong to the trigonal system; sample HCR_{24}(333) with space group *R*3*c* (a=5,75 Å and c= 47,38 Å) and HC-NO_3 with space group *P*3*c*1 (a=5,75 Å and c= 17,34 Å) (Table 4.7). In the diffractogram of sample HC-NO_3 a small fraction of calcite is observed (JCPDS files [086-2334]).

Table 4.7. Crystallographic parameters for samples HCR_{24}(333) and HC-NO_3.

Sample	2θ(º) (00l)	d_{00l} (Å)	*c* (Å)	crystallite size (00l) (nm)	FWHM (º) (110)	*a* (Å)	Space group
HCR_{24}(333)	11,19	7,90	47,38	48	0,21	5,75	*R*3*c*
HC-NO_3	10,19	8,67	17,34	86	0,18	5,75	*P*3*c*1

The diffractogram of sample HCR_{24}(333) shows the highest intensities for the peaks that correspond to the stacking direction, which are reflections (006) and (0012), and are in good agreement for the characteristic LDH structure. The basal distance for the reflection (001) (7,90 Å) agreed with the presence of chloride (ionic radii 1,81 Å) anions in the interlayer space. The larger value of basal distance for HC-NO_3 compared to HC-Cl can be consequence of the higher ionic radii of nitrate (3,84 Å for nitrate and 1,81 Å for chloride) [Miyata 1983]. Parameters ***a*** and ***c***, which were calculated from d_{110} and d_{006}, respectively, are similar to those reported for the pattern, which imply a similar stoichiometry. Sample HC-NO_3, analogously, presented the highest intensities in the diffractogram for reflections (002) and (004) which are related to the stacking direction. The ***a*** parameter agrees with the typical stoichiometry for this sample. The main difference between these two CaAl-LDHs is in the crystallite size. Sample HC-NO_3 presents a higher degree of stacking along the *c* direction (86 nm) compared to sample HCR_{24}(333) (48 nm). The same tendency was observed in the direction of the layer (FWHM (110) =0.18º) compared to the chloride CaAl-LDH (FWHM (110) =0.21º).

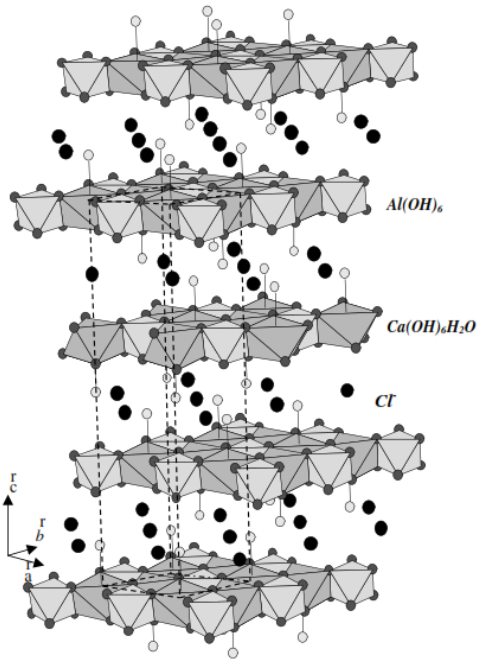

Figure 4.9 Structure of a CaAl-LDH with chloride anion [Rousselot *et al*. 2002].

Figure 4.9 shows a representative CaAl-LDH structure with chloride as anion. The chloride anion is surrounded by a cohesive environment in the interlayer region. The strong bonds between the anion the water molecules and the layers offer a high cohesion of the structure [Duan *et al.* 2005].

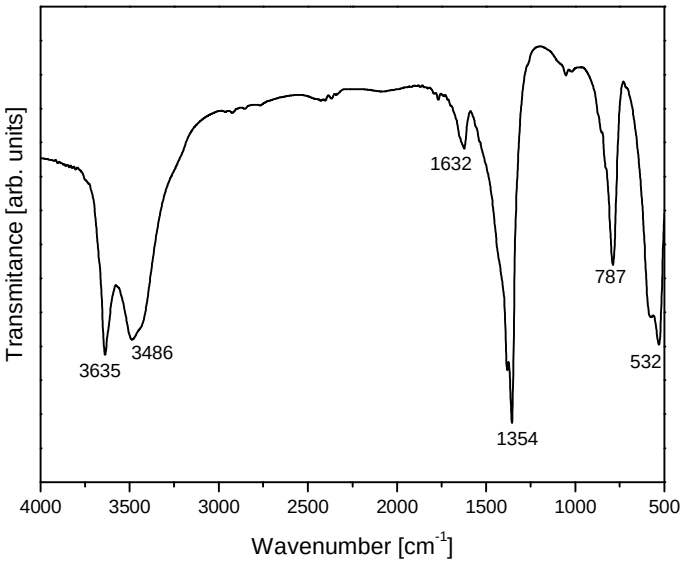

Figure 4.10. FT-IR spectrum of sample HC-NO_3.

FT-IR characterization was studied in order to see differences in the anion composition of the two CaAl-LDHs. For sample HCR_{24}(333), the typical bands can be found in the previous section 4.4.1. However, FTIR spectroscopy it is not generally used to detect chloride anion, it can be used to detect the presence of nitrate and other anions [Cavani *et al*. 1991]. In figure 4.10 it is possible to observe the FTIR spectra for sample HC-NO_3. The two typical bands, associated to the interlayer nitrate anion, appear between 1500 and 700 cm^{-1}. However, because of the low intensities, only the band around 1354 cm^{-1} was observed. The two bands at 3635 and 3486 cm^{-1} were ascribed to the OH stretching (Al-OH) and (Ca-OH), respectively, of the lamellae and to the water molecules in the interlamellar region. The band at around 1632 cm^{-1} was associated to the deformation mode of water molecules. Finally, the bands at 787 cm^{-1} and 532 cm^{-1} could be due to Al-O vibrations, respectively [Linares *et al*. 2014].

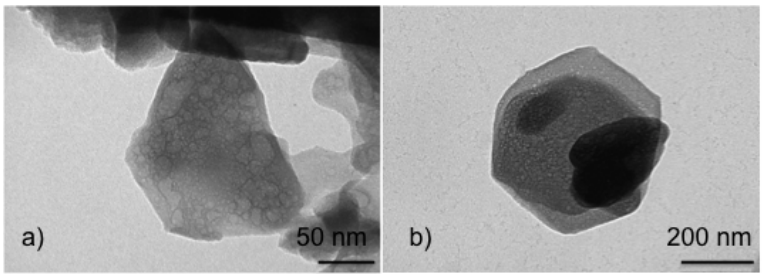

Figure 4.11. TEM micrographs of samples a) HCR_{24}(333) and b) HC-NO_3.

TEM micrographs (Figure 4.11) showed the typical hexagonal platelets of layered materials. In general, the sizes of particles ranged between 40 and 300 nm for HCR_{24}(333) sample and between 60 and 600 nm for HC-NO_3 sample. The size distribution of the lamellae was rather broad. The nitrate CaAl-LDHs exhibited larger and more regular particles than the chloride CaAl-LDH, thus suggesting a more crystalline nature of this sample in agreement with XRPD results.

Thermogravimetric analysis of the samples led to two differentiated temperature of anion decomposition, as expected for LDH with chloride and nitrate counter anions (Fig. 4.12).

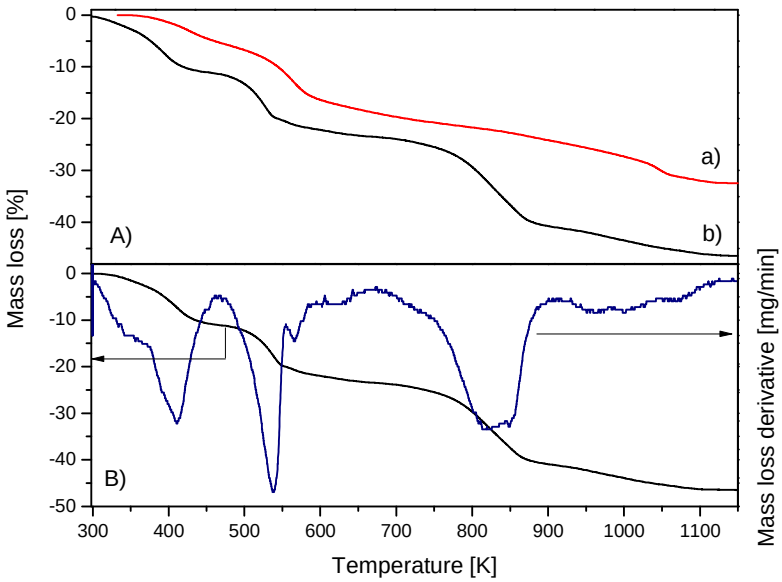

Figure 4.12. A) Thermograms for samples a) HCR_{24}(333) and b) HC-NO_3. B) Thermogram of sample HC-NO_3 with first derivative of mass loss.

Generally, the corresponding decomposition steps for CaAl-LDHs are as follows: dehydration of interlamellar water, dehydroxilation and anion decomposition [Vieille *et al*. 2003]. Particularly for HCR_{24}(333), chloride decomposition takes place in two steps, usually until 1473 K [Domínguez *et al.* 2011]. By the shape of the TGA curve, it is possible to observe that anion decomposition has not been completed at the temperature of 1100 K. Thermogravimetric characterization for HCR_{24}(333) is reported in the section 4.4.1 of this chapter. Regarding HC-NO_3 sample, the main mass loss steps corresponded to dehydration between 298 and 463 K (10,7%), decomposition of nitrate to nitrite and dehydroxilation of hydroxyls between 463 and 673 K (12,8%) and anion decomposition of nitrite and condensation of hydroxyls between 673 and 1273 K (22,8%). From dehydration step until 1273 K the mass loss was 35,6%. Also, some dehydroxilation during anion decomposition was produced, as suggested elsewhere [Renaudin *et al*. 2000]. At the temperature of 1273 K dehydroxilation was still not finished.

At the temperature of calcination of 723 K, chosen as a compromise with the *memory effect* of calcined mixed oxides, sample HCR_{24}(333) is transformed into a mixture of calcium and aluminium oxides with chloride content, whilst sample HC-NO_3 is transformed into a mixture of calcium and aluminium oxides with very low or nule nitrate content.

The diffractograms corresponding to the calcined CaAl-LDHs show (Fig.4.13a and 4.13b) an absence of the reflections that corresponded to the stacking direction, typical of layered structures. The diffractogram of sample $cHCR_{24}$(333) corresponds to an amorphous material.

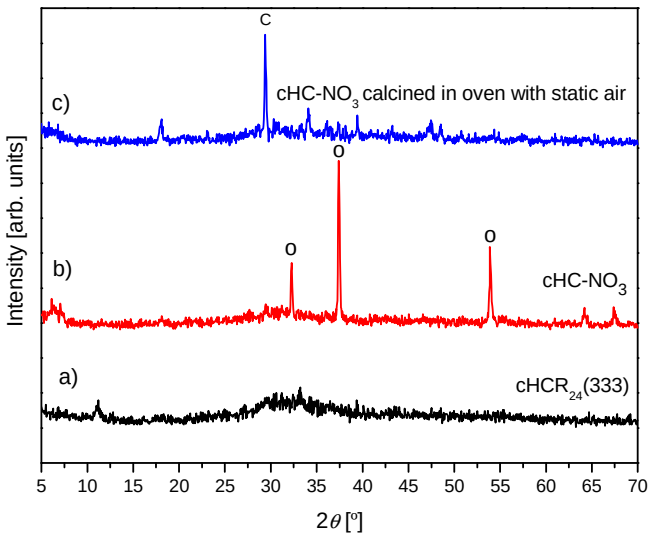

Figure 4.13. XRPD diffractograms of samples a) $cHCR_{24}$(333) and b) cHC-$NO_3$and c) cHC-NO_3 calcined in a mufle. C: calcite, O: CaO.

Further temperatures are needed to see the appearance of calcium oxide phase. For sample cHC-NO_3, a phase identified as CaO (JCPDS file: [37-1497]) was observed in the diffractogram. This is in agreement with the decomposition for this sample observed in the TGA curve. The presence of CaO for sample cHC-NO_3 is related to an earlier anion decomposition, compared to sample $cHCR_{24}$(333). The presence of NO_3^- in the reconstructed structure will affect the *memory effect* of sample cHC-NO_3 since the presence of nitrate in the mixed oxide is very little. Additionally, it is important to remark that when calcination was performed in an oven with static air, a phase attributed to calcite (JCPDS file [072-1652]) appeared in the diffractogram (Fig. 4.13c for cHC-NO_3). Thus, calcination was always carried through a tubular furnace with synthetic flowing air.

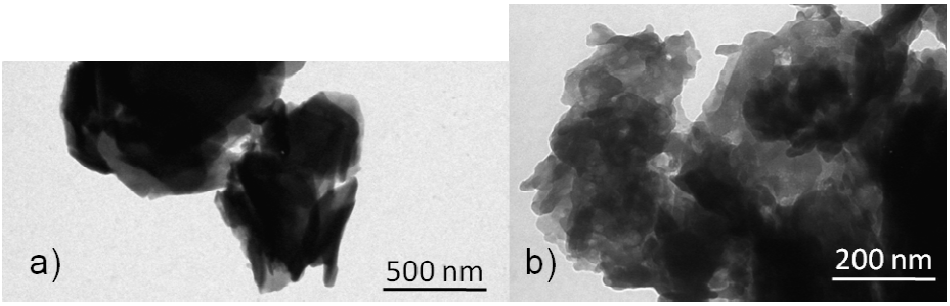

Figure 4.14. TEM micrographs of samples a) $cHCR_{24}(333)$ and b) $cHC\text{-}NO_3$

TEM micrographies of calcined samples resemble the previous layered particles (Fig. 4.14a and 4.14b). Lamellae of calcined CaAl-LDHs have decreased their size, compared to as-synthesized ones, mainly due to the water and anion loss that provokes the layer cracking. This decrease is more remarkable for sample $cHC\text{-}NO_3$ that presents a more extensive decomposition. For $cHCR_{24}(333)$ sample the lamellae sizes ranged between 450 and 100 nm while for $cHC\text{-}NO_3$ sample the range was between 200 and 50 nm. In general, particles were more aggregated for $cHCR_{24}(333)$ sample. There was a decrease in the size of the larger particles for this sample. Summarizing, samples were made of aggregates with heterogeneous shapes, being mainly sharp for $cHCR_{24}(333)$ and rounded for $cHC\text{-}NO_3$.

Reconstructed CaAl-LDHs.

Reconstructed CaAl-LDHs were synthesized by rehydration in the presence of NaCl and $NaNO_3$ salts from the calcined samples. The diffractograms of rehydrated CaAl-LDHs are shown in figures 4.15 and 4.16. After rehydration processes, it was possible to identify CaAl-LDH phase for all samples, and so the rehydration process in the presence of ultrasounds was satisfactory. In general, it was possible to observe the appearance of katoite in the reconstructed samples, contrary to the synthesized CaAl-LDH by co-precipitation. However, for some samples the incorporated anion was not previously expected considering the salt added in the reconstruction process, leading us to agree with a degree of affinity for anion insertion in the layered space of the CaAl-LDHs during reconstruction in aqueous media.

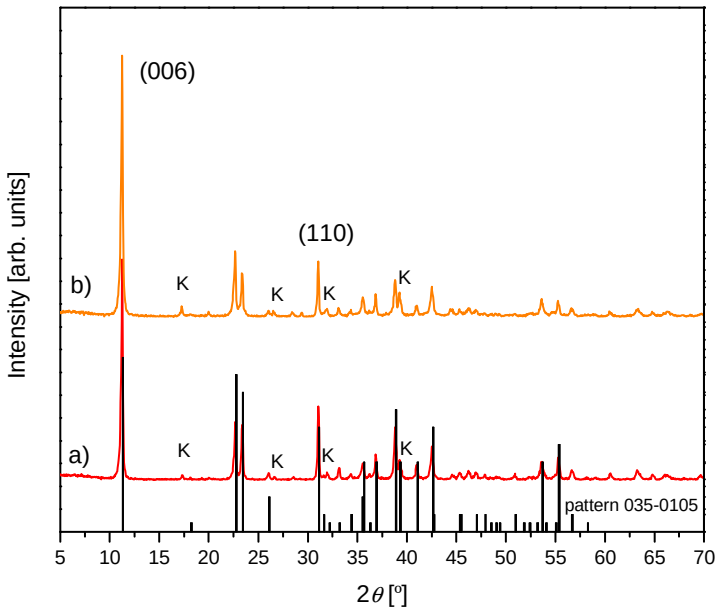

Figure 4.15. XRPD diffractograms of samples a) rHC-Cl-Cl and b) rHC-Cl-NO_3. K: katoite

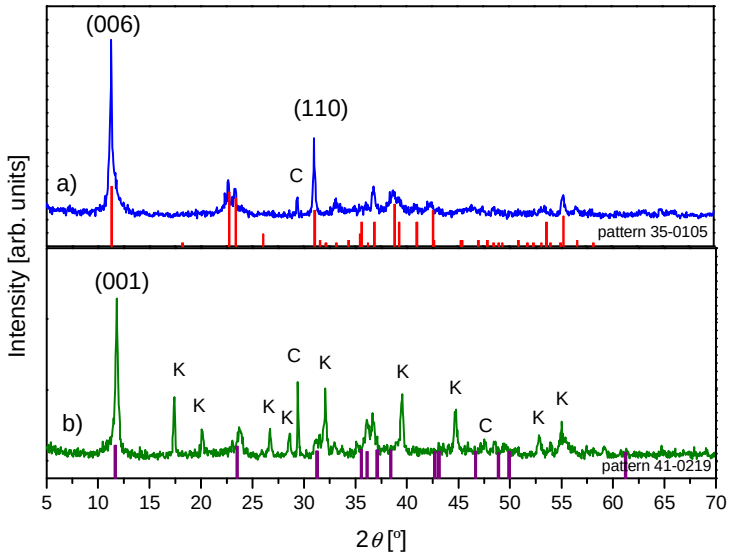

Figure 4.16. XRPD diffractograms of samples a) rHC-NO_3-Cl and b) rHC-NO_3-NO_3. K: katoite, C: calcite.

The CaAl-LDH crystalline phase was identified in all samples. This means that the rehydration process in the presence of ultrasounds was effective. However, in addition to the desired crystalline phase, it was possible to observe the appearance of katoite phase ($Ca_3Al_2(O_4H_4)_3$) (JCPDS file [074-3032]), which was not present in the CaAl-LDHs synthesized by direct co-precipitation. Katoite belongs to the body-centered cubic system with space group *Ia*-3*d* and lattice parameter a=12,57 Å.

Table 4.8. Crystallographic parameters for reconstructed samples.

Sample	2*θ* (º) (006)	d_{006} (Å)	*c* (Å)	crystallite size (006) (nm)	FWHM (º) (110)	*a* (Å)	Space group	Anion incorporated
rHC-Cl-Cl	11,26	7,85	47,09	56	0,17	5,75	*R*3*c*	chloride
rHC-Cl-NO_3	11,25	7,86	47,15	51	0,18	5,76	*R*3*c*	chloride
rHC-NO_3-Cl	11,3	7,82	46,94	45	0,19	5,75	*R*3*c*	chloride

Table 4.9. Crystallographic parameters for sample rHC-NO_3-NO_3.

Sample	2*θ* (º) (001)	d_{001} (Å)	crystallite size (001) (nm)	*a b c* (Å)	α β γ(º)	Space group	Anion incorporated
rHC-NO_3-NO_3	11,69	7,56	31	5,98/5,74/7,85	92,6/101,94/120,07	P-1	carbonate

The formation of a small fraction of katoite could be attributed to different anion diffusion during the reconstruction, depending on the particle size. For the samples reconstructed from $cHCR_{24}$(333) the CaAl-LDHs with chloride anion phase (hydrocalumite) was identified as the main phase (JCPDS file [035-0105]) along with some minor contribution of the katoite phase (Figure 4.15).

In the diffractogram of rHC-Cl-NO_3 sample the main phase observed was again the CaAl-LDH with chloride anion together with low amounts of katoite phase too (Figure 4.15). Additionally, a small fraction of calcite, probably due to some degree of contamination during the synthesis, was identified (JCPDS files [086-2339]). During the reconstruction process, there is a competition between the chloride present in the $cHCR_{24}$(333) sample and the nitrate of the solution, being the chloride incorporation of chloride more favoured due to its higher affinity (Table 4.8).

The highest XRPD peak intensity corresponded to the reflection (006) related to the stacking direction. This peak appeared at almost the same value of 2*θ* angle (11,26º and 11,25º for rHC-

Cl-Cl and rHC-Cl-NO_3, respectively) for the two samples reconstructed from $cHCR_{24}$(333) (Table 4.8). The basal distances were therefore, almost identical, with values of 7,85 and 7,86 Å.

These values allow us to confirm that during the reconstruction process chloride anions remain incorporated in the interlayer space. Cells parameters ***a*** and ***c*** were very similar for these two samples. The crystallite size in the stacking direction was slightly higher for rHC-Cl-Cl sample (56 nm) than for rHC-Cl-NO_3 sample (51 nm). Comparing the crystallographic parameters with those of sample HCR_{24}(333) we can conclude that the CaAl-LDH with chloride anion phase was successfully reconstructed for samples rHC-Cl-Cl and rHC-Cl-NO_3.

CaAl-LDH phase was also found after rehydration of the samples reconstructed from cHC-NO_3 (Fig. 4.16). XRPD pattern of rHC-NO_3-Cl mainly showed the presence of the chloride CaAl-LDH phase. However, calcite was also identified as a minor phase. The presence of calcite was already present in the precursor HC-NO_3. For sample rHC-NO_3-NO_3, carbonate CaAl-LDH phase (JCPDS files [041-0219]) was the main crystalline phase. The carbonate CaAl-LDH belongs to the triclinic system with space group *P*-1, and their lattice unit cell parameters are a= 5,78 Å, b= 8,47 Å and c= 9,92 Å, and α=64,77º β=82,75º and γ=81,43º (Table 4.9). For this sample, katoite and calcite were also observed. Comparing their intensities, their contribution cannot be negligible. The highest intense XRPD peak, which belongs to the reflection (00l) related to the stacking direction, appeared at 11,30º and 11,81º 2*θ* values, respectively for rHC-NO_3-Cl and rHC-NO_3-NO_3. These values agree with the anion present in each sample, chloride and carbonate, respectively. The basal distance d_{00l} presented values of 7,82 and 7,48 Å, respectively for rHC-NO_3-Cl and rHC-NO_3-NO_3, respectively. Sample rHC-NO_3-Cl had larger crystallite size in the stacking direction than rHC-NO_3-NO_3 (45 and 31 nm, respectively). The incorporation of carbonate instead of nitrate anions during the reconstruction can be explained by the different affinity for anion incorporation (higher affinity of carbonate than nitrate) [Duan *et al.* 2005].

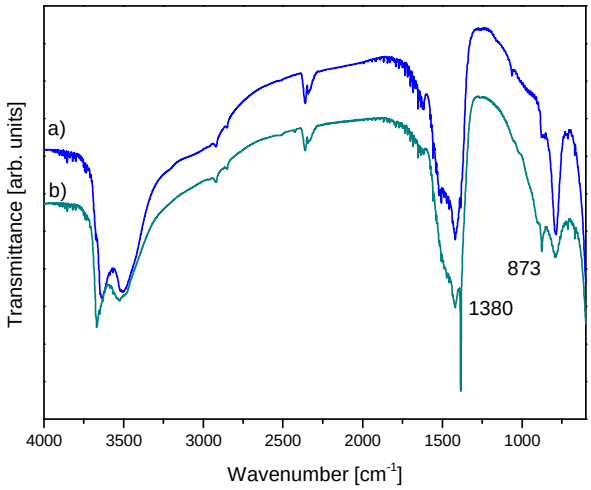

Figure 4.17. FT-IR spectra for samples a) rHC-NO_3-Cl and b) rHC-NO_3-NO_3.

In general, all reconstructed samples showed the typical FT-IR spectra for LDHs (Fig. 4.17). From the intensities and the position of the bands around 1420 cm^{-1}, we can possible confirm the presence of calcite in the rHC-NO_3-Cl and rHC-NO_3-NO_3 samples, as previously observed, in the corresponding XRPD diffractograms (Fig. 4.16). Additionally, sample rHC-NO_3-NO_3 presented the two characteristic stretching peaks attributed to the carbonate anion in the interlayer region at 873 and 1380 cm^{-1}. This also agrees with the XRPD results (Fig. 4.16b).

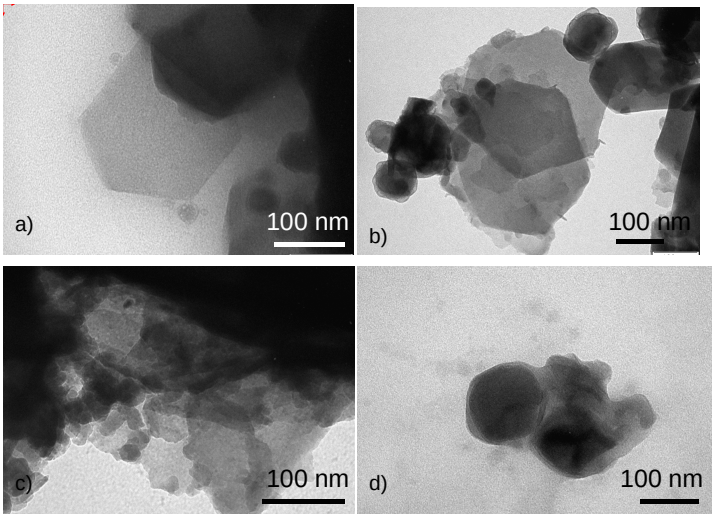

Figure 4.18. TEM micrographs of samples a) rHC-Cl-Cl, b) rHC-Cl-NO_3, c) rHC-NO_3-Cl and d) rHC-NO_3-NO_3.

TEM micrographs of the rehydrated samples are shown in figure 4.18. In general, all samples show a lamellar morphology with thin layers of heterogeneous sizes that have decreased their size compared to the initial as-synthesized ones. Values ranged between 300 and 40 nm for reconstructed samples.

Delamination studies.

In order to study delamination of the samples, two methods have been used to promote delamination: by the use of mechanical stirring and by the use of ultrasounds in the presence of a solvent. Results are shown in Table 4.10. Fast-checking of the delamination procedure was tested in-situ by the Tyndall effect [Ma *et al*. 2006] (Fig. 4.19).

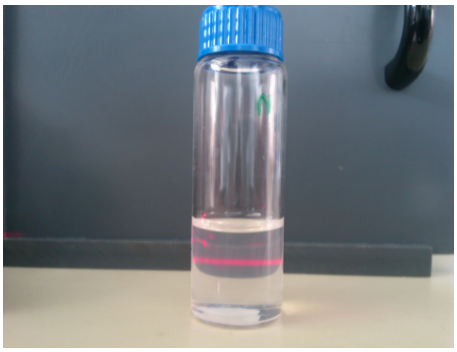

Figure 4.19. Tyndall effect corroborated for a delaminated sample.

Formamide was chosen as an adequate solvent to enhance delamination on LDH, based on results published before for LDH (see section 4.1.3). With the use of mechanical stirring as-synthesized samples HCR_{24}(333) and HC-NO_3 were not delaminated by the use of mechanical stirring. The solutions remained turbid and the majority of the particles sedimented after 48 h. In contrast, when the sonication was performed by the use of ultrasounds, sample HC-NO_3 could undergo delamination.

Table 4.10. Delamination tests.

Sample	Delamination by mechanical stirring	Delamination by sonication
HCR_{24}(333)	no[1]	no[1]
HC-NO_3	no[1]	yes
rHC-Cl-Cl	no[2]	yes[3]
rHC-Cl-NO_3	no[2]	yes
rHC-NO_3-Cl	no[2]	yes
rHC-NO_3-NO_3	no[2]	yes[3]

1: very turbid solution, 2: majority sedimentation of the particles after 48 h, 3: a few particles sedimented after 48 h.

Figure 4.20 shows the diffractogram corresponding to sample HC-NO_3 delaminated by sonication. The CaAl-LDH phase was not present. Only a broad signal due to the solvent was observed in the diffractogram. Consequently, the sample could be considered delaminated. In contrast, sample HCR_{24}(333), treated under the same conditions remained non-delaminated.

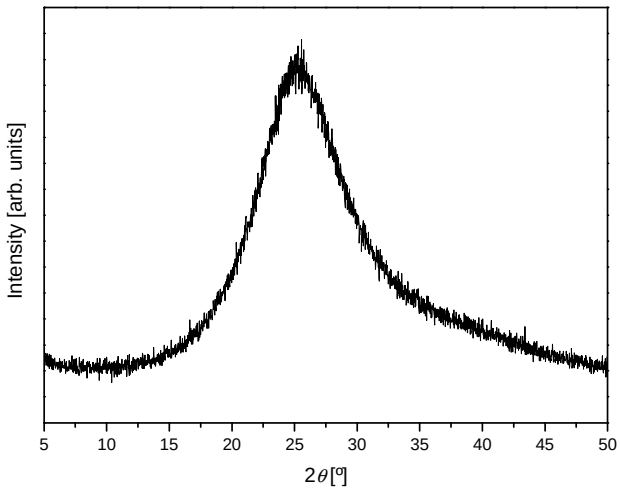

Figure 4.20. XRPD diffractogram for delaminated sample HC-NO_3.

We could suggest that mechanical stirring is not always a powerful effective procedure to delaminate CaAl layered double hydroxides. Our results could suggest that mechanical stirring and ultrasounds are not powerful effective procedures to delaminate this chloride CaAl-LDH. The nature of the chloride-CaAl-LDH with poor swelling capacity and large particle size could explain the difficulties observed for its delamination (Fig. 4.11a) [Duan *et al.* 2005]. In support of this observation, previous studies reported that the low swelling capacity was related to the environment for the chloride anion in the interlayer region. The strong interactions between the anion, the water molecules and the layers offer a high cohesion to the structure [Duan *et al.* 2005]. Sample HC-NO_3 could have a less cohesive environment because of the larger size of the nitrate anion together with a higher swelling capacity. These reasons would explain why sample HC-NO_3 could undergo delamination.

Reconstructed samples could led to certain degree of delamination in the presence of mechanical stirring but the process did not yield stable suspensions and the particles mainly sedimented after 48 h. Again, mechanical stirring was not a good procedure to provoke delamination in formamide solution. The fact that the size of the particles were smaller, in comparison with the parent ones, possibly favored some degree of delamination. However, the resulting particles sedimented after 48 h. Their smaller particle size, in comparison with the parent ones, probably favoured some degree of delamination. However, the particles sedimented after 48 h. The fact that certain delamination was accomplished involves that some swelling capacity was possible for reconstructed CaAl-LDHs, in comparison with HCR_{24}(333) and HC-NO_3. When reconstructed samples were sonicated the delamination process led to more stable suspensions although for rHC-Cl-Cl and rHC-NO_3-NO_3 samples some sedimentation only appeared after 48 h. For rHC-Cl-Cl sample this could be related to the cohesive interlamellar

region that difficults swelling in the larger particles, and thus some particles started to sediment after 48 h. For rHC-NO_3-NO_3 sample (i.e. for carbonate CaAl-LDHs) we could noticed that the delamination was more difficult probably because of the presence of carbonate species that make the interlayer region more cohesive (d_{001}=7,56 Å, Table 4.9). This was the sample with the highest content of carbonate species, which were present both in the interlayer region of the CaAl-LDH and in the calcite extra-phase. Samples rHC-Cl-NO_3 and rHC-NO_3-Cl could undergo an extensive delamination using ultrasounds and remained stable after 48 h. This can be explained by the lower presence of carbonate and the small particle size of these samples. In general, the use of ultrasounds was more effective compared to mechanical stirring in order to provoke delamination.

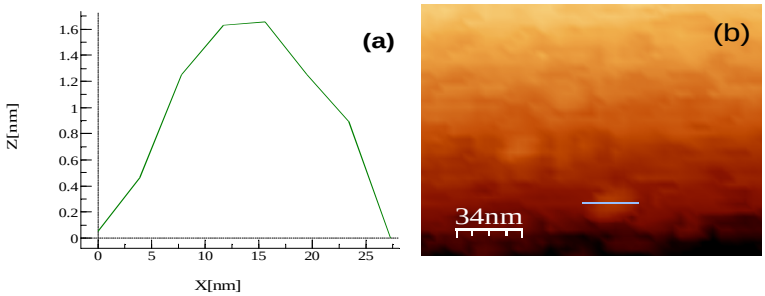

Figure 4.21. AFM micrograph of HC-NO_3. a) topography of a detailed particle, b) AFM micrograph.

The process of delamination was characterized by AFM microscopy. In figure 4.21 it is possible to observe a representative tapping-mode AFM micrography of sample HC-NO_3 together with a detailed profile image. The morphology of the delaminated sheets appears irregular, with lateral sizes that ranged between 200 and 30 nm and lateral thickness around 1.6 nm, which could be attributed to two single layers [Cho *et al.* 2014]. Thus, exfoliation process was successfully achieved for CaAl- LDH in the presence of ultrasounds and using formamide as solvent.

Hybrid reconstructed CaAl-LDH with thiol-capped CdTe nanoparticles.

An hybrid CaAl-LDH was synthesized by rehydration of a calcined chloride CaAl-LDH, in the presence of thiol-capped CdTe nanoparticles, obtaining a sample labelled as hrHC-Cl. Figure 4.22 shows the diffractogram for sample hrHC-Cl.

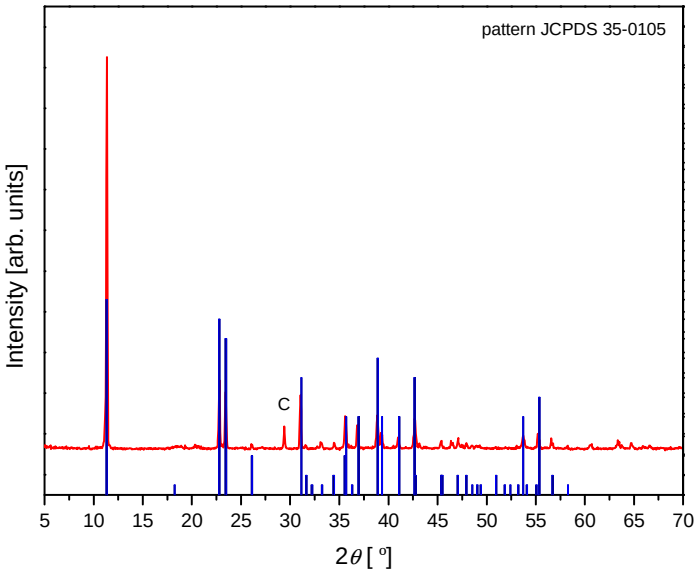

Figure 4.22. XPRD Diffractogram for sample hrHC-Cl.

The CaAl-LDH phase was identified by XRPD (JCPDS file 035-0105) (Fig. 4.22). The sample belongs to the trigonal system with space group *R3c*, with cell parameters (a= 5,76 Å and c= 46,74 Å) (Table 4.10). The highest intensity values were observed for the peaks that correspond to the stacking direction (006) and (0012) are in agreement with the LDH structure. The (006) diffraction peak appeared at values of 2θ, which corresponded to the expected value for chloride CaAl-LDHs (11,34º). The basal distance (7,79 Å) was also in agreement with the size of the chloride anion. It is therefore inferred that CdTe nanoparticles were not incorporated in the interlayer region. Optic measurements were necessary to identify the presence of CdTe nanoparticles in the external surface, as described below.

Sample hrHC-Cl presented calcite phase, as well, in low amounts. Some CO_2 incorporation could have occurred during the synthesis. This sample synthesized from rehydration showed slightly larger crystallite size along the direction of the lamella (FWHM= 0,15º), calculated from reflection (110), than samples rHC-Cl-Cl and rHC-Cl-NO_3, which were reconstructed from $cHCR_{24}$(333) without the presence of CdTe nanoparticles (0,17 and 0,18º, respectively) (Table 4.8). In the same way, crystallite size along the (006) reflection was larger (86 nm) compared to the reconstructed samples from the calcined chloride CaAl-LDH ($cHCR_{24}$(333)) (56 and 51 nm, respectively for samples rHC-Cl-Cl and rHC-Cl-NO_3). The larger crystallite size of sample hrHC-Cl could be associated to a less effective breaking of the lamellae during the reconstruction made under ultrasounds in the presence of CdTe nanoparticles.

Table 4.10 Crystallographic parameters for the hybrid CaAl-LDH.

Sample	2*θ*(º) (006)	d_{006} (Å)	*c* (Å)	crystallite size (006) (nm)	FWHM (º) (110)	*a* (Å)	Space group	Anion incorporated
hrHC-Cl	11,34	7,79	46,74	86	0,15	5,76	*R*3*c*	chloride

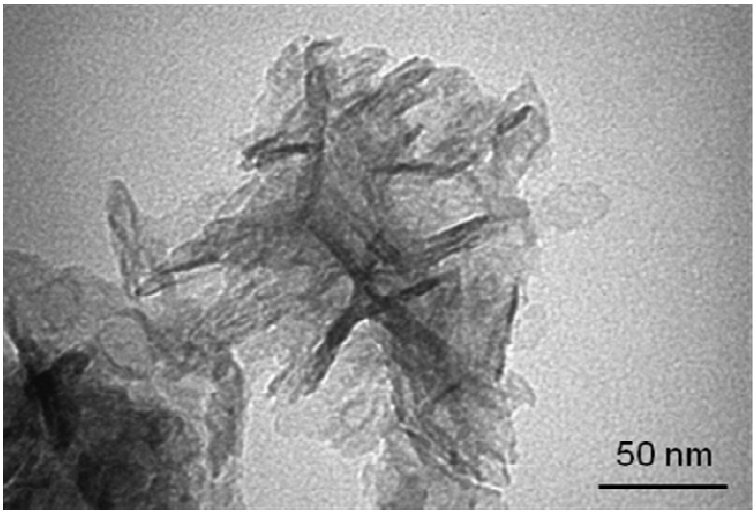

Figure 4.23.TEM micrographs of sample a) hrHC-Cl.

A TEM micrograph of the hybrid CaAl-LDH is shown in figure 4.23. The sample is formed by aggregates of disordered and ordered lamellae with particle sizes between 20 and 60 nm and it is also possible to observe different orientations of the lamellae. The CdTe nanoparticles could not be clearly distinguished. In order to test the luminescence of the hybrid sample, the emission spectrum was recorded (Fig. 4.24).

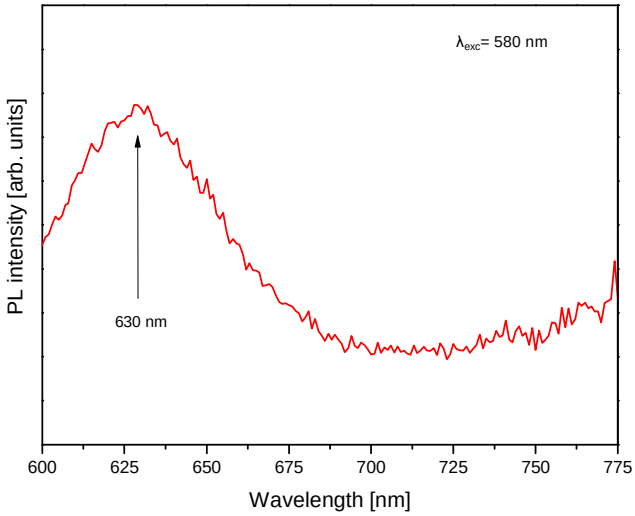

Figure 4.24. PL spectrum of sample hrHC-Cl.

It was possible to detect the photoinduced emission from the nanoparticles in the red region of the visible spectrum, with a peak centered at 630 nm. The low intensity of the peak could be associated to a limited number of nanoparticles probably located in the external edges of the lamellae.

4.5 Conclusions.

In this work, several CaAl-LDHs were synthesized by changing two variables, microwave or conventional heating and autoclave or refluxing. With the aim of synthesize faster a more crystalline material for future applications, we found that the sample $HCMW_1(453)$ prepared with microwaves by autoclave at 453 K for 1 h not only decreased significantly times of preparation compared to the conventional CaAl-LDHs reported in literature (aged at reflux for 24 h), but also presented high crystallinity, as observed by XRPD and TEM-electron diffraction. This agrees with its low surface BET area (2 m^2/g), its large defined hexagonal particles (4000 nm) and its highest temperature of dehydration and dehydroxilation observed by thermogravimetric analysis. In general, we can conclude that the use of microwaves for hydrocalumite synthesis favors a faster crystalline growth in the stacking direction whereas the use of autoclave improves the lamellar crystallinity (microwaves or conventional). Samples whose aging treatment was performed with microwave irradiation and in autoclave ($HCMW_1(453)$, $HCMW_6(353)$ and $HCMW_1(353)$) exhibited the lowest values of BET surface area (2, 5 and 5 m^2/g respectively) and the highest crystallinity. This characteristic was defined by their crystallite size for (006) reflection since these samples presented the highest values (762, 724 and 757 Å respectively),

by their lowest FWHM for (110) reflection (0.15, 0.15 and 0.16º respectively) and by their well-defined hexagonal lamellae with the highest size observed by TEM (>1600 nm).

Regarding characterization of reconstructed and delaminated CaAl-LDH, a series of CaAl-LDHs have been synthesized and later calcined in order to recover the CaAl-LDH structure through reconstruction, obtaining LDH with smaller lamellar sizes. The use of ultrasounds in the reconstruction procedure led to LDH with smaller lamellar size and lager crystallite size in the stacking direction. Delamination studies have been conducted using mechanical stirring and ultrasounds in the presence of formamide, for samples synthesized by co-precipitation and by rehydration. To the best of our knowledge, this is the first reported delamination for CaAl-LDH. The use of repeated cycles of ultrasounds made delamination possible for all samples, but for HCR_{24}(333). The cohesive surroundings for the chloride anion in sample HCR_{24}(333) and the little swelling capacity provoke that delamination was not possible for this sample. After 48 h, some particles of samples rHC-Cl-Cl and rHC-NO_3-NO_3 sedimented. In general, mechanical stirring was not a powerful effective procedure to delaminated synthesized or reconstructed CaAl-LDHs.

Finally, a hybrid CaAl-LDH with thiol-capped CdTe nanoparticles was synthesized by reconstruction from a calcined chloride CaAl-LDH. The CaAl-LDH phase was detected by the XRPD diffractogram. The nanoparticles were detected by optic measurements, observing an emission peak at around 630 nm that corresponds to the red region in the visible spectrum.

References for chapter 4

[Abelló *et al*. 2005] Abelló S., Medina F., Tichit D., Pérez-Ramírez J., Cesteros Y., Salagre P. and Sueiras J.E. **2005**, *Nanoplatelet-based reconstructed hydrotalcites: towards more efficient solid base catalysts in aldol condensations*, Chem. Commun., 1453-1455.

[Adachi-Pagano *et al*. 2000] Adachi-Pagano M., Forano C. and Besse J.P. **2000**, *Delamination of layered double hydroxides by use of surfactants*, Chem. Commun., 91-92.

[Álvarez *et al*. 2013] Álvarez M.G., Chimentão R.J., Barrabés N., Föttinger K., Gispert-Guirado F., Kleymenov E., Tichit D. and Medina F. **2013**, *Structure evolution of layered double hydroxides activated by ultrasound induced reconstruction*, Appl. Clay Sci., 83-84, 1-11.

[Aramendía *et al*. 2002] Aramendía M.A., Borau V., Jiménez C., Marinas J.M., Ruiz J.R. and Urbano, F.J. **2002**, *Comparative study of Mg/M(III) (M=Al, Ga; In) layered double hydroxides obtained by coprecipitation and the sol-gel method*, 168, 156-161.

[Ayala *et al*. 2011] Ayala A., Fetter G., Palomares E. and Bosch P. **2011**, *CuNi/Al hydrotalcites synthesized in presence of microwave irradiation*, Mater. Lett. 65, 1663-1665.

[Balonis 2010] Balonis M. **2010**, *The influence of inorganic chemical accelerators and corrosion inhibitors on the mineralogy of hydrated Portland cement systems*, Ph.D thesis, University of Aberdeen.

[Benito *et al*. 2006] Benito P., Labajos F.M., Rocha J. and Rives, V. **2006**, *Influence of microwave radiation on the textural properties of layered double hydroxides*, Micro. Meso. Mater., 94, 148-158.

[Bergadà *et al.* 2007] Bergadà O., Vicente I., Salagre P., Cesteros Y., Medina F. and Sueiras J.E. 2007, *Microwave effect during aging on the porosity and basic properties of hydrotalcites*, Micropor. Mesopor. Mater., 101, 363–373.

[Campos-Molina *et al.* 2010] Campos-Molina M.J., Santamaría-González J., Mérida-Robles J., Moreno-Tost R., Albuquerque M.C.G., Bruque-Gámez, S. Rodríguez-Castellón E., Jiménez-López and A. and Maireles-Torres, P. **2010**, *Base Catalysts Derived from Hydrocalumite for the Transesterification of Sunflower Oil*, Energ. Fuel., 24, 979–984.

[Cavani *et al.* 1991] Cavani F., Trifirò F. and Vaccari A. **1991**, *Hydrotalcite-type anionic clays: Preparation,properties and applications*, *Catal. Today*, *11*, 173-301.

[Cho *et al*. 2014] Cho S., Hong S.C. and Kim S. **2014**, *Quantum dot-layered double hydroxide composites for near-infrared emitting codes*, J. Mater. Chem. C, 2, 450-457.

[Cota *et al.* 2010] Cota I., Ramírez E., Medina F., Sueiras J.E., Layrac G. and Tichit D. **2010**, *New synthesis route of hydrocalumite-type materials and their application as basic catalysts for aldol condensation*, Appl. Clay Sci., 50, 498-502.

[Cullity *et al*. 2001] Cullity B.D. and Stock S.R. **2001**, *Elements of X-Ray Diffraction*, 3rd ed, Prentice Hall, New Jersey.

[Dávila *et al*. 2008] Dávila V., Lima E., Bulbulian S. and Bosch P. **2008**, *Mixed Mg(Al)O oxides synthesized by the combustion method and their recrystallization to hydrotalcites*, *Micropor. Mesopor. Mater*., 107, 240-246.

[Domínguez *et al*. 2011] Domínguez M., Pérez-Bernal M.E., Ruano-Casero J.R., Barriga C., Rives V. Ferreira R.A.S., Carlos L.D. and Rocha J., **2011**, *Multiwavelength Luminescence in Lanthanide-Doped Hydrocalumite and Mayenite*, Chem. Mater., 23, 1993-2004.

[Duan *et al.* 2005] Duan X. and Evans D. G. 2005, Layered Double hydroxides, Structure and bonding, Springer, Verlag Berlin Heidelberg.

[Gay 1972] Gay P. **1972**, *The Crystalline State, an Introduction*, 1st ed, Oliver & Boyd, Edinburgh.

[Gordijo *et al.* 2007] Gordijo C.R, Constantino V.R.L. and de Oliveira Silva, D. **2007**, *Evidences for decarbonation and exfoliation of layered double hydroxide in N,N-dimethylformamide-ethanol solvent mixture*, J. Solid State Chem., 180, 1967-1976.

[Grover *et al.* 2010] Grover K., Komarneni S. and Katsuki H. **2010**, *Synthetic hydrotalcite-type and hydrocalumite-type layered double hydroxides for arsenate uptake*, Appl. Clay Sci., 48, 631-637.

[Gunjakar *et al.* 2011] Gunjakar J.L., Kim T.W., Kim H.N., Kim I.Y. and Hwang S.J. **2011**, *Mesoporous layer-by-layer ordered nanohybrids of layered double hydroxide and layered metal oxide: highly active visible light photocatalysts with improved chemical stability*, J. Am. Chem. Soc., 133, 14998-15007.

[Hibino 2004] Hibino T. **2004**, *Delamination of layered double hydroxides containing amino acids,* Chem. Mater., 16, 5482-5488.

[Hibino *et al*. 2001] Hibino T. and Jones W. **2001**, *New approach to the delamination of layered double hydroxides*, J. Mater. Chem., 11, 1321-1323.

[Jobbágy *et al.* 2004] Jobbágy M. and Regazzoni A.E. **2004**, *Delamination and restacking of hybrid layered double hydroxides assessed by in situ XRD*, J. Colloid Interface Sci., 275, 345-348.

[Kuwahara *et al*. 2010] Kuwahara Y., Ohmichi T., Kamegawa T., Mori K. and Yamashita H. **2010**, *A novel conversion process for waste slag: synthesis of a hydrotalcite-like compound and zeolite from blast furnace slag and evaluation of adsorption capacities*, J. Mater. Chem., 20, 5052–5062.

[Lee *et al*. 2014] Lee G., Jeong Y., Takagaki A. and Jung J.C. **2014**, *Sonication assisted rehydration of hydrotalcite catalyst for isomerization of glucose to fructose*, J. Mol. Catal. A:Chem., 393, 289-295.

[Li *et al*. 2005] Li L., Ma R., Ebina Y., Iyi N. and Sasaki T. **2005**, *Positively charged nanosheets derived via total delamination of layered double hydroxides*, Chem. Mater., 17, 4386-4391.

[Linares *et al.* 2014] Linares C.F, Ocanto F., Bretto P. and Monsalve M. **2014**, *Study of as-synthesized and calcined hydrocalumites as possible antacid agents*, Bull. Mater. Sci., 37, 941-944.

[Liu *et al*. 2006] Liu Z., Ma R., Osada M., Iyi N., Ebina Y., Takada K. and Sasaki T. **2006**, *Synthesis, anion exchange, and delamination of Co-Al layered double hydroxide: assembly of the exfoliated nanosheet/polyanion composite films and magneto-optical studies*, J.Am.Chem.Soc., 128, 4872-4880.

[Ma *et al*. 2006] Ma R., Liu Z., Li L., Iyi N. and Sasaki T. **2006**, *Exfoliating layered double hydroxides in formamide: a method to obtain positively charged nanosheets*, J. Mater. Chem., 16, 3809-3813.

[Mesbah *et al*. 2011] Mesbah A., François M., Cau-dit-Coumes C., Frizon F., Filinchuk Y., Leroux F., Ravaux J and Renaudin G. **2011**, *Crystal structure of Kuzel's salt* $3CaO{\cdot}Al_2O_3{\cdot}1/2CaSO_4{\cdot}1/2CaCl_2{\cdot}11H_2O$ *determined by synchrotron powder diffraction*, Cem. Concr. Res., 41, 504-509.

[Milliron *et al*. 2004] Milliron D.J., Hughes S.M., Cul Y., Manna L., Li J., Wang L.W. and Alivisatos A.P. **2004**, *Colloidal nanocrystal heterostructures with linear and branched topology*, Nature, 430, 190-195.

[Miyata 1983] Miyata S. **1983**, *Anion-exchange properties of hydrotalcite-like compounds*, Clays Clay Miner. 31, 305-311.

[Mora *et al*. 2011] Mora M., López M.I., Jiménez-Sanchidrián C. and Ruiz J.R. **2011**, *Near- and mid-infrared spectroscopy study of synthetic hydrocalumites*, Solid State Sci. 13, 101-105.

[Moore *et al.* 1989] Moore D.M. and Reynolds R.C. **1989**, *X-Ray Diffraction and the Identification and Analysis of Clay Minerals*, 1st ed, Oxford University Press, Oxford.

[Naik *et al.* 2011] Naik V.V., Ramesh T.N. and Vasudevan S. **2011**, *Neutral nanosheets that gel: exfoliated layered double hydroxides in toluene*, J. Phys. Chem. Lett., 2, 1193-1198.

[Ocelli *et al.* 1992] Ocelli M.L and Robson H. **1992**, *Synthesis of microporous materials*, Vol II. Expanded clays and other microporous solids, 1st ed., Springer.

[Ogawa *et al*. 2002] Ogawa M. and Kaiho H. **2002**, *Homogenous precipitation of uniform hydrotalcite particles*, Langmuir, 18, 4240-4242.

[Ontam *et al.* 2012] Ontam A., Khaorapapong N. and Ogawa M. 2012, Immobilization of cadmium telluride nanoparticles on the surface of hexadecyltrimethylammonium-montmorillonite, J. Mater. Chem., 22, 20001-20007.

[Othman *et al.* 2009] Othman M.R., Helwani Z., Martunus and Fernando W.J.N. **2009**, *Synthetic hydrotalcites from different routes and their application as catalysts and gas adsorbents: a review*, Appl. Organometal. Chem. 23, 335-346.

[Patil *et al.* 2002] Patil K.C., Aruna S.T and Mimani T. **2002**, *Combustion synthesis: an update*, Curr. Opin. Solid State Mater. Sci., 6, 507-512.

[Pavel *et al*. 2010] Pavel O.D., Zăvoianu R., Bîrjega R. and Angelescu E. **2010**, *Impact of the memory effect on the catalytic activity of Li-Al hydrotalcite-like compounds for the cyanoethylation reaction*, Mater.Res.Bull.,45, 1106-1111.

[Pavel *et al*. 2011] Pavel O.D., Zăvoianu R., Bîrjega R. and Angelescu E. **2011**, *The effect of ageing step elimination on the memory effect presented by $Mg_{0.75}Al_{0.25}$hydrotalcites (HT) and their catalytic activity for cyanoethylation reaction*, Catal. Commun., 12, 845-850.

[Plank *et al.* 2014] Plank J., Zou N., Zhao Z. and Dekany, I. **2014**, *Preparation and properties of a graphene oxide intercalation compound utilizing hydrocalumite layered double hydroxide as host structure*, Z. Anorg. Allg. Chem., 640, 1413-1419.

[Radha *et al*. 2005] Radha A.V., Kamath P.V. and Shivakumara C. **2005**, *Mechanism of the anion exchange reactions of the layered double hydroxides (LDHs) of Ca and Mg with Al*, Solid State Sci., 7, 1180-1187.

[Renaudin *et al*. 2000] Renaudin G., Rapin J.P., Humbert B. and François M. **2000**, *Thermal behaviour of the nitrated AF, phase $Ca_4Al_2(OH)_{12}(NO_3)_2{\cdot}4H_2O$ and structure determination of the intermediate hydrate $Ca_4Al_2(OH)_{12}(NO_3)_2{\cdot}2H_2O$*, Cem. Concr. Res., 30, 307-314.

[Rousselot *et al.* 2002] Rousselot I., Taviot-Guého C., Leroux F., Léone P., Palvadeau P. and Besse J.P. **2002**, *Insights on the Structural Chemistry of Hydrocalumite and Hydrotalcite-like Materials: Investigation of the Series $Ca_2M^{3+}(OH)_6Cl{\cdot}2H_2O$ (M^{3+}: Al^{3+}, Ga^{3+}, Fe^{3+}, and Sc^{3+}) by X-Ray Powder Diffraction*, J. Solid State Chem. 167, 137-144.

[Sánchez *et al.* 2012] Sánchez T., Salagre P., Cesteros Y. and Bueno-López A. **2012**, *Use of delaminated hectorites as supports of copper catalysts for the hydrogenolysis of glycerol to 1,2-propanediol*, Chem. Eng. J., 179, 302–311.

[Sánchez-Cantú *et al*. 2013] Sánchez-Cantú M., Pérez-Díaz L.M., Tepale-Ochoa N., González-Coronel V.J., Ramos-Cassellis M.E., Machorro-Aguirre D. and Valente J.S. **2013**, *Green synthesis of hydrocalumite-type compounds and their evaluation in the transesterification of castor bean oil and methanol*, Fuel, 110, 23-31.

[Sharma *et al*. 2010] Sharma S.K., Parikh P.A and Jasra R.V. **2010**, *Reconstructed Mg/Al hydrotalcite as a solid base catalyst for synthesis of jasminaldehyde*, Appl. Catal A: Gen., 386, 34-42.

[Stoeger *et al*. 2012] Stoeger J. A., Palomino M., Agrawal K. V., Zhang X., Karanikolos G. N., Valencia S., Corma A. and Tsapatsis M. **2012**, *Oriented CoSAPO-5 Membranes by Microwave-Enhanced Growth on TiO_2-Coated Porous Alumina*, Angew. Chem. Inter. Ed. 51, 2470–2473.

[Stoica *et al.* 2012] Stoica G., Castelló Serrano I., Figuerola A., Ugarte I., Pacios R. and Palomares E. **2012**, *Layered double hydroxides as carriers for quantum dots@silica nanospheres*, Nanoscale, 4, 5409-5419.

[Swanson *et al*. 2013] Swanson C.H., Stimpfling T., Troutier-Thulliez, A.L., Hintze-Bruening H. and Leroux F. **2013**, *Layered double hydroxide platelets exfoliation into a water-based polyester*, J. Appl. Polym. Sci., 128, 2954-2960.

[Tao *et al*. 2010] Tao Q., Zhu J., Frost, R.L., Bostrom T.E., Wellard R.M., Wei J., Yuan P. and He H. **2010**, *Silylation of layered double hydroxides via a calcination-rehydration route*, Langmuir, 26, 2769-2773.

[Tóth *et al.* 2014] Tóth V., Sipiczki M., Pallagi A., Kukovecz A., Kónya Z., Sipos P. and Pálinkó I. **2014**, *Synthesis and properties of CaAl-layered double hydroxides of hydrocalumite-type*, Chem. Pap., 68, 633-637.

[Trujillano *et al.* 2010] Trujillano R., Rico E., Vicente M.A., Herrero M. and Rives V. **2010**, *Microwave radiation and mechanical grinding as new ways for preparation of saponite-like materials*, Appl. Clay Sci. 48, 32-38.

[Valente *et al.* 2010] Valente J.S, Lima E., Toledo-Antonio J.A., Cortes-Jacome M.A., Lartundo-Rojas L., Montiel R. and Prince J. **2010**, *Comprehending the thermal decomposition and reconstruction process of sol-gel MgAl layered double hydroxides*, J. Phys. Chem. C, 114, 2089-2099.

[Vicente *et al.* 2010] Vicente I., Salagre P., Cesteros Y. and Sueiras J.E. **2010**, *Microwave-assisted synthesis of saponite*, Appl. Clay Sci. 48, 26–31.

[Vieille *et al*. 2003] Vieille L., Rousselot I., Leroux F., Besse J.P. and Taviot-Guého C. **2003**, *Hydrocalumite and Its Polymer Derivatives. 1. Reversible Thermal Behavior of Friedel's Salt: A Direct Observation by Means of High-Temperature in Situ Powder X-ray Diffraction*, Chem. Mater., 15, 4361-4368.

[Wang *et al*. 2007] Wang S.L. and Wang P.C. **2007**, *In situ XRD and ATR-FTIR study on the molecular orientation of interlayer nitrate in Mg/Al-layered double hydroxides in water*, Colloids Surf. A Physicochem Eng. Asp., 292, 131-138.

[Wang *et al.* 2012] Wang Q. and O'Hare D. **2012**, *Recent advances in the synthesis and application of layered double hydroxide (LDH) nanosheets*, Chem. Rev., 112, 4124-4155.

[Werner *et al.* 2013] Werner S., Lau V.W.H., Hug S., Duppel V., Clausen-Schaumann H. and Lotsch B.V. **2013**, *Cationically charged $Mn^{II}Al^{III}$ LDH nanosheets by chemical exfoliation and their use as building blocks in graphene oxide-based materials*, Langmuir, 29, 9199-9207.

[Wu *et al.* 2007] Wu Q., Sjåstad A.O., Vistad, Ø.B., Knudsen K.D., Roots J., Pedersen J.S. and Norby, P. **2007**, *Characterization of exfoliated layered double hydroxides (LDH, Mg/Al=3) nanosheets at high concentrations in formamide*, J. Mater. Chem., 17, 965-971.

[Xu *et al*. 2011] Xu S., Zhang B., Chen Z., Yu J., Evans D.G. and Zhang, F. **2011**, *A General and Scalable Formulation of Pure CaAl-Layered Double Hydroxide via an Organic/Water Solution Route*, Ind. Eng. Chem. Res., 50, 6567-6572.

[Xu *et al*. 2013] Xu C., Gao Y., Liu X., Xin R. and Wang Z. **2013**, *Hydrotalcite reconstructed by in situ rehydration as a highly active solid base catalyst and its application in aldol condensations*, RSC Adv., 3, 793-801.

[Zhao *et al*. 2011] Zhao J., Kong, X., Shi, W., Shao M., Han J., Wei M., Evans D.G. and Duan X. **2011**, *Self-assembly of layered double hydroxide nanosheets/Au nanoparticles ultrathin films for enzyme-free electrocatalysis of glucose*, J. Mater. Chem., 21, 13926-13933.

[Zhao *et al.* 2012] Zhao Y., Li J.G., Fang F., Chu N, Ma H. and Yang X. **2012**, *Structure and luminescence behaviour of as synthesized, calcined, and restored MgAlEu-LDH with high crystallinity*, Dalton Trans., 41, 12175-12184.

CHAPTER 5

Glycerol etherification to short-chain polyglycerols using calcined MgAl and CaAl layered double hydroxides as catalysts

5.1 Introduction.

5.1.1 The etherification reaction of glycerol towards polyglycerols in published literature.

It is possible to find in the literature many studies on the etherification reaction of glycerol towards short-chain polyglycerols. Many catalysts have been tested, mainly basic ones but also some with acidic properties. As it will be further explained later on this section, the reaction might be as well catalyzed by acid sites [Ruppert *et al*. 2008]. Consequently, also catalysts with an acid-basic bifunctional nature will be eligible as candidates for catalysts.

Some homogenous catalysts have been tested in the literature. Barrault and Clacens tested Na_2CO_3 at 533 K. They achieved a 87,5% of conversion and di- and triglycerol selectivities of 50,4 and 26%, respectively [Barrault *et al.* 2004]. Ayoub tested several homogenous catalysts: NaOH, LiOH, KOH and Na_2CO_3 performing the reaction in the range of 453 and 533 K [Ayoub *et al*. 2012]. They found that the highest diglycerol selectivity after 2 and 6 h of reaction was for catalyst LiOH, around 40 and 20%, respectively with conversions of 80 and 100%, respectively. They studied with LiOH several parameters including catalyst loading, temperature and reaction time, and found the best conditions, which were selectivity of 33 % for a conversion of 100%, after 6 h of reaction at 513 K. Richter and co-workers studied the catalytic behavior of $CsHCO_3$ and found complete glycerol selectivity with a diglycerol selectivity of 20% [Richter *et al.* 2008]. Highest diglycerol selectivity (100%) was achieved only at low glycerol conversion (20%).

Barrault and Clacens compared an important number of catalysts (homogeneous and heterogeneous) as well as the performance of catalysts that appeared reported in patents with the aim of obtaining high selectivities towards di- and triglycerol [Clacens *et al.* 1998, Clacens *et al*. 2002, Clacens *et al.* 2000, Sivaiah *et al*. 2012]. They used impregnated mesoporous materials, with magnesium, cesium and lanthanum, exchanged mesoporous materials with cesium, and aluminum grafted mesoporous materials, among others. They compared the catalytic results to homogenous Na_2CO_3 and CsOH and to some zeolites that appeared in published patents. Selectivities of heterogenous catalysts in general improved the results of the homogenous ones, performing the reaction at 533 K for 8 h and 24 h. The most significant result yielded selectivity values to di- and triglycerol of 62 % and 33 %, respectively, for a 79 % of conversion at 533 K after 24 h for the caesium-based mesoporous catalyst. Lanthanum and magnesium impregnated mesoporous materials were not so selective or active and furthermore lead to higher amounts of secondary-reaction product acrolein. Nonetheless these results, cesium leaching was detected independently of the catalyst's quantity loaded into the batch reactor.

Recently, Barrault *et al.* tested several materials with Mg incorporated in the structure in order to avoid Mg leaching: Mg-MCM-41 in a pilot scale, and Mg-clays in a lab scale. Bulk and supported MgO were also tested for comparison [Sivaiah *et al.* 2012]. (Di- + tri-)glycerol selectivity and conversion values did not change after scale up when using MCM-41 powder catalysts (70% and 100%, respectively at 533 K after 20 h of reaction) whereas Mg-clays presented high selectivity towards (di- + tri-)glycerols (80%) for a conversion of 85% at 533 K after 7 h of

reaction. The use of MgO led to high conversion (77% at 533 K after 4 h of reaction), but inactive magnesium glyceroxide was identified in the catalyst after reaction. The same behavior was observed when using CaO and BaO. In general, the use of Mg- containing catalysts resulted in a higher degree of polymerization, since (tetra+penta)glycerol selectivity was detected for these catalysts (between 15-21%) [Sivaiah *et al.* 2012].

Ruppert *et al.* tested several alkali oxides [Ruppert *et al.* 2008] performing the reaction at 493 K. They tested oxides of Mg, Ca, Sr and Ba. They found that glycerol conversion increased with the basicity of the catalysts in the following order: MgO<CaO<SrO<BaO. The best selectivities towards di- and triglycerol were obtained for CaO. Based on the basic characterization they concluded that basic sites were not only responsible for the reaction mechanism. In order to clarify the nature of the active sites, after studying Lewis acidity they suggested a possible basic mechanism with contribution of acid sites, that would operate in this etherification reaction. The two mechanisms, basic-acid and basic, are shown in scheme 5.1. They detected, as well, colloidal particles formed during the reaction, this leaching appearance might be a problem to recover the catalyst.

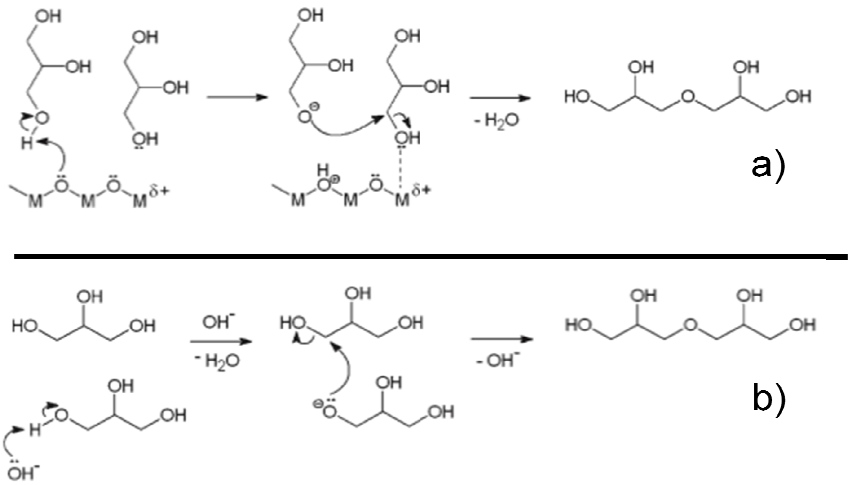

Scheme 5.1. a) Basic-acid catalyzed reaction, b) Basic catalyzed reaction [Ruppert *et al.* 2008].

Abdullah *et al.* obtained 53% and less than 25% of selectivity towards di- and triglycerol, respectively, for a conversion of 98% at 513 K for 12 h using calcined LiOH-modified montmorillonite [Gholami *et al*. 2013, Ayoub *et al.* 2013]. The montmorillonite, a smectite type of clay, was chosen because of the pore distribution looking for a shape-selective mechanism.

These authors also reported a selectivity of 74 % to di + triglycerol for a conversion of 91% at 523 K for 8 h using Ca-La oxide supported on MCM-41, a mesoporous material, although some metal leaching was observed [Gholami *et al*. 2014].

The group of Maireles-Torres *et al.* used calcined Mg/Al and Mg/Fe layered double hydroxides (LDH) [García-Sancho *et al.* 2011, Guerrero-Urbaneja et al. 2014]. Regarding Mg/Al calcined LDHs, the highest conversion (50%) was found for a catalyst prepared using $NaOH/Na_2CO_3$ as precipitant agent, with selectivity to di- and triglycerol of 85 and 15 %, respectively at 493 K after 24 h of reaction. Using different Mg/Al catalysts with the same basic characteristics, different catalytic results were obtained due to the shape-selectivity of the reaction. Large pores lead to triglycerol formation whereas small pores lead to diglycerol formation.

Regarding Mg/Fe calcined LDHs, the best result was obtained for the catalyst with a molar ratio of 4, achieving total selectivity towards di-+triglycerol at a conversion around 40%. They characterized the basicity and acidity of the catalysts to explain a possible acid-base bifunctional behavior.

5.1.2 Industrial applications of short-chain polyglycerols.

The obtention of polyglycerols in the industry is significantly interesting seeing the different uses of them. Particularly at the food industry, their presence is considerable in a number of processes. They may be used as food emulsifiers, for example, in the form of polyglycerol esters. Food emulsifiers are of key importance in the bakery and chocolate industry. In the chocolate industry, polyglycerol polyricinoleate adjusts the properties of chocolate, for example.

A quick glance at our kitchen will provide a number of items where chemical compounds derived from polyglycerols are present in: ice creams, dressings, beverages, *light* processed food, chewing gums… These chemical compounds are collected as E-numbers (valid in the European Union and Switzerland) as E-475, E-476 [Solvay, Solvay b].

Besides those applications, many others include their use as polymer additives, lubricants, plasticizers, stabilizers, humectants, antifoaming agents… [Solvay c, Solvay d]

Their use at the industry justify the number of patents about the production of polyglycerols, some of them are summarized in the following table (Table 5.1):

Table 5.1. Some examples of patents regarding polyglycerol production.

Year of publication	Patent #	Title	Catalyst	Inventors	Applicant
1949	US2487208 A [Patent 1949]	Preparation of diglycerol	basic catalyst	A.W. Godfrey	Colgate Palmolive Peet Co.
1998	US5710350 A [Patent 1998]	Process for the production of diglycerol	zeolite	L. Jeromin, B. Gutsche, R. Bunte, V. Jordan	Henkel
2002	US20020058781 A1 [Patent 2002]	Processes for preparing linear polyglycerols and polyglycerol esters	calcium compound	D. Lemke	-
2008	EP1961726 A1 [Patent 2008]	Process for the conversion of glycerol and catalytically active material suitable therefore	CaO doped with alkali oxide compounds	A.M. Ruppert, B.M. Weckhuysen	Netherlands Organisation for Scientific Research
2012	EP2491069 A2 [Patent 2012]	Production and composition of glycerol based polyols	base catalyst stronger than NaOH	X. H. Li, J.L. Shih, H.E. Bode, J. Wang, F.J. Swiecinski	Nalco Company
2014	EP2754684 A1 [Patent 2014]	Method for the production of hyperbranched polyglycerol	CaO-based catalyst	R. Ciriminna, M. Pagliaro	Greenseal Chem

5.1.3 Etherification reaction from glycerol to short-chain polyglycerols.

The reaction studied in this chapter is the one-pot etherification reaction from glycerol to short-chain polyglycerols. The polyglycerols of interest, for this particular work, range from diglycerol to pentaglycerol. The reaction is shown in scheme 5.2.

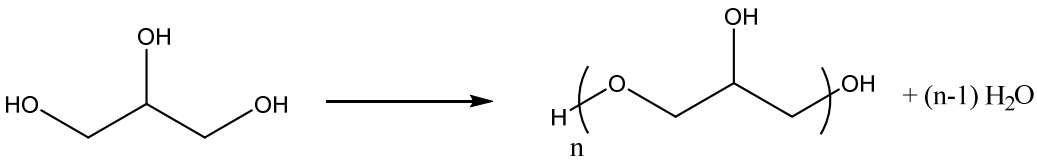

Scheme 5.2. Polyglycerol reaction.

In order to favor the etherification reaction for polyglycerol production, the tested catalysts mainly have basic properties. Both homogeneous and heterogeneous catalysts have been used to catalyze this reaction. The aim of using heterogeneous catalysts is to simplify and optimize the costs for the obtention of polyglycerols by:

- performing the etherification in a one-pot reaction.
- removing water constantly from the reaction.
- using catalysts easy to synthesize.
- trying to re-use the catalyst.
- increasing selectivities to separate easily the products of reaction.

In this work, the catalysts used are mixed oxides of MgAl and CaAl. The precursors are hydrotalcites- and hydrocalumites-like compounds, which belong to the family of layered double hydroxides. In chapter 1 and 4 more information can be found about LDHs. After their calcination, the LDH transforms into a mixture of metal oxides. Calcined LDH have been used before in other reactions [Corma *et al.* 1998] as well as for the reaction of this study [García-Sancho *et al.* 2011, Guerrero-Urbaneja *et al*. 2014].

5.1.4 Derivatization reaction for polyglycerols.

In order to analyze the products of reaction (short-chain polyglycerols) they cannot be directly introduced into the gas chromatograph. Because of the polarity of the compounds, only broad peaks would be observed in the chromatogram. So, they should be derivatized in order to see narrow and well-defined peaks.

Analytical derivatization is employed for two reasons:

- to permit analysis of compounds not directly amenable to analysis due to, for example, inadequate volatility or stability.

- to improve the analysis by, for example, improving chromatographic behavior or detectability. The foremost reason in gas chromatography (GC) analysis it to impart volatility to otherwise nonvolatile compounds. Masking on polar groups by derivatization can yield dramatic increases in volatility [Knapp 1979].

Replacement of hydrogen of the polar group –OH by silylation increases volatility. For this, replacement of the active hydrogens with trimethylsilyl groups gives volatile products that readily undergo GC analysis. Also it should be pointed out that some sensitive compounds can undergo partial thermal decomposition in GC, so derivatization may be employed to yield a more stable product and improve the chromatographic performance and peak shape.
The general equation to form silyl derivatives is shown in scheme 5.3:

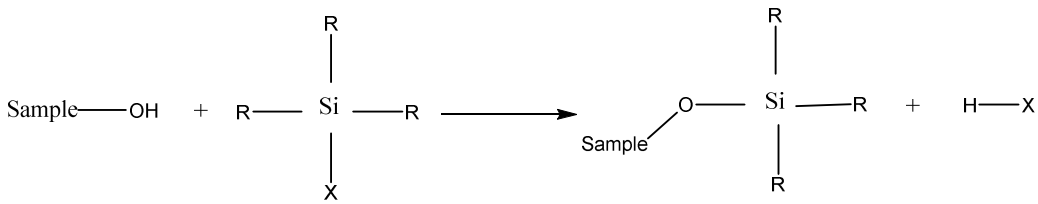

Scheme 5.3. General silylation reaction.

Trimethylsilyl derivatives are commonly used but other substituted silyl derivatives can be used too. For our particular case, the mechanism appears to involve nucleophilic attack upon silicon, after deprotonation of hydrogens by pyridine of the polar –OH group.
A variety of reagents have been developed, some commercial brands sell ready-to-use silylating mixtures. The common reagents are HMDS and TMCS, hexamethyldisilazane and trimethylchlorosilane, respectively. The silyl donor potencies of the reagents are markedly influenced by the solvent systems and added catalysts. TMCS is often added to the reagents to increase the silyl donor strength.

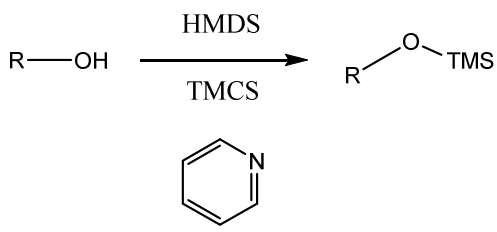

Scheme 5.4 Silylation reaction used in this work.

Basic catalysts have been used to promote silyl enol ether formation [Knapp 1979]. In this case, HMDS has a poor silylating power and it is the main drawback for its application [Bruynes *et al*.

1982]. For the activation of HMDS, a variety of catalysts have been reported. Herein TMCS in pyridine has been used as a catalyst. The reaction is shown in scheme 5.4.

5.1.5 Acrolein, a *valuable but unwanted* product of the glycerol etherification reaction.

Several compounds may result from glycerol dehydration, as seen in scheme 5.5. In this reaction, double dehydration of glycerol occurs because the temperature exceeds 473 K and because the acid and basic sites of the catalysts might catalyze its formation. Because of this, a *Dean-Stark* system, for example, needs to be attached to the reactor to extract water constantly because it can displace the sense of the reaction to produce acrolein but also the etherification reaction of our interest.

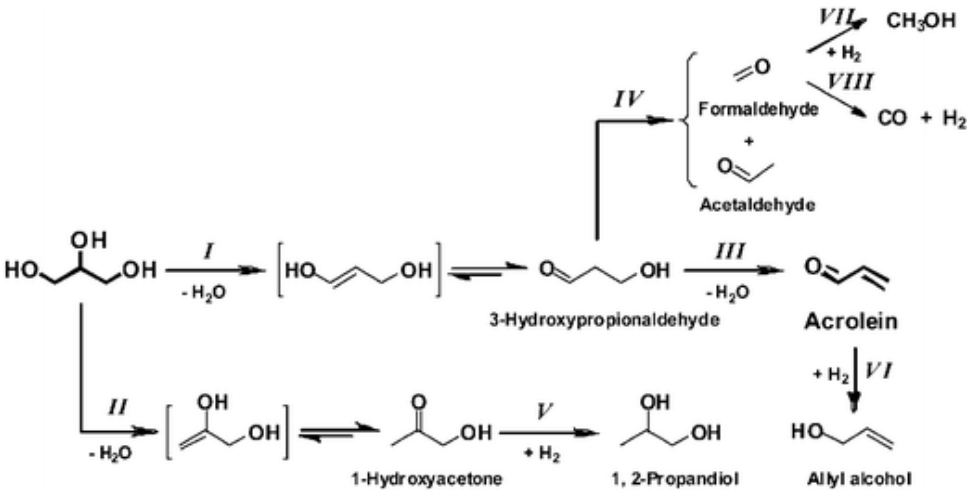

Scheme 5.5. Compounds obtained from glycerol dehydration [Chai *et al.* 2007].

Scheme 5.6 shows specifically the scheme reaction of double dehydration from glycerol to acrolein.

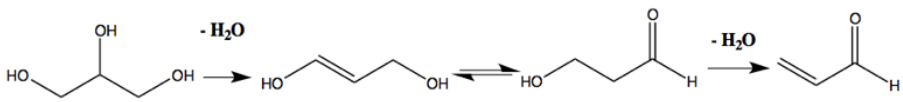

Scheme 5.6. Acrolein formation from glycerol.

Acrolein is a product used in the chemistry industry because it is an intermediate of acrylic acid. From acrylic acid, many compounds are derived that are used in many applications such us:

plastics, coatings, adhesives, elastomers… From acrolein many compounds can be also obtained (pyridines, 1,3 propanediol, flavors and fragrances…). It can be directly used as a biocide for algae and water microorganisms in water systems, to control the growth of microorganisms in fuels…

The usual path to obtain acrolein is based on propene which is oxidized by heterogeneous catalysts containing metals such as bismuth and molybdenum at high temperatures [Behr *et al.* 2008]. Additional to this petrochemical route, acrolein can also be obtained from glycerol by dehydration in the liquid or in the gas phase on heterogeneous catalysts [Chheda *et al*. 2007, Chai *et al*. 2007].

Additionally, it is important to remind the toxicity of this compound, highly reviewed in the literature. At room temperature it is colorless or yellowish and has a disgusting odor. Inhalation or dermal exposure should be avoided. Safety measures must be followed when working with acrolein, specially, placing all the reaction set-up inside a fume hood. Multiple studies have linked lung cancer to active and passive smokers: acrolein is found in all cigarette brands [DeWoskin *et al*. 2003].

5.2 Aim of this chapter.

The aim of this chapter is to test a series of calcined layered double hydroxides for the etherification reaction of glycerol to short-chain polyglycerols (scheme 5.1). The catalytic results have been correlated to the acid and basic properties. The influence and the effect of several parameters have been studied on the etherification reaction, such as the nature of the catalyst, the different hydrothermal treatments and the temperature of calcination.

- the precursors: MgAl-LDHs and CaAl-LDHs.
- the hydrothermal treatments: using microwave irradiation or conventional heating, in autoclave or refluxing.
- calcining the catalysts at different temperatures: 723, 923 and 1073 K.

5.3 Experimental procedure.

5.3.1 Catalyst precursors synthesis.

MgAl layered double hydroxides (MgAl-LDHs) synthesis.

The synthesis of MgAL-LDHs was done by co-precipitation at low supersaturation, starting from the hydrated nitrate salts of Mg and Al. The set-up went as follows: two 50 ml burets are placed on a 600 ml beaker, located on a stirring mantle. A 50 ml solution of the salts, keeping a Mg:Al ratio 3:1, was prepared and placed in a buret, whilst in the other a 2 M solution of NH_3 was added (usually 200 ml of ammonia solution are prepared). In the beaker we add 100 ml of a solution 0,0078 M of $(NH_4)_2CO_3$. The procedure is done at constant pH of 10, with vigorously

stirring and at room temperature. When the addition of the salts has been completed, a hydrothermal treatment is applied to the solution. In this work, two treatments have been applied, one refluxing in a glass round-bottom flask for 18 h at 333 K and the other using microwaves irradiation and in autoclave for 1 h at 453 K.

When the hydrothermal treatment was completed, the solution was filtered and the solid washed with deionized water until pH 7. Finally, it was dried in an oven at 353 K overnight. Each solid was ground, labelled and stored in a desiccator. Table 5.2 summarizes the samples prepared.

Table 5.2. MgAl-LDHs prepared and their aging conditions.

Sample	Heating	Recipient	Temperature (K)	Time (h)
HT-R18(333)	conventional	reflux	333	18
HT-mw1(453)	microwaves	autoclave	453	1

CaAl layered double hydroxides (CaAl-LDHs) synthesis.

The synthesis of CaAl-LDHs is explained in Chapter 4. From all the samples synthesized, four samples have been chosen to be later calcined and used as catalysts in the etherification reaction. These samples are summarized in Table 5.3 along with their aging treatment parameters.

Table 5.3. CaAl-LDHs prepared and their aging conditions.

Sample	Heating	Recipient	Temperature (K)	Time (h)
HC-R24(333)	conventional	reflux	333	24
HC-R3(353)	conventional	reflux	353	3
HC-Rmw3(353)	microwaves	reflux	353	3
HC-mw1(453)	microwaves	autoclave	453	1

5.3.2 Catalyst synthesis.

The precursors were calcined at 723 K for 15 h to obtain the mixture of oxides that will be the catalysts used in the etherification reaction. In order to study the influence of calcination temperature, precursor HC-mw1(453) was also calcined at 923 and 1073 K. The nomenclature for the catalysts remains the same than for the precursors but adding a *c* before each sample name.

5.3.3 Etherification reaction set-up.

The etherification reaction was always carried inside a fume hood with proper ventilation. Several heating mantles were used for this reaction, some of them with an interior basket made of fabric to surround the glass reactor. However some difficulties arose achieving the reaction

temperature. Thus, the solution found was using a plain heating mantle with a metal adaptor with the shape of the round-bottom flask to distribute the heat homogeneously.

In a typical experiment, around 28 g of glycerol were placed in a 50 ml topaz 3-neck glass reactor. The central neck was connected directly to a Dean Stark system that was coupled to a condenser. In another neck, N_2 was constantly being bubbled and in the other one a temperature probe was introduced being in contact with the glycerol. The reaction was performed at 508 K, the amount of catalyst used was 2 wt% and samples were taken after 24 h for analysis in the gas chromatograph. Stirring was kept during the reaction.

In order to prevent from thermal loss, the system was wrapped with glass wool and aluminum foil. The following image shows the reaction set-up (figure 5.1).

Figure 5.1. Reaction set-up.

Following safety measurements and because it's unstable, after cleaning the reaction set-up once a reaction was completed, all liquids resulting from cleaning were collected and stored at a freezer (253 K) in dark bottles.

The following are the equations used to calculate glycerol conversion (5.1) and polyglycerol selectivity values (5.2):

$$X_{\text{glycerol}}(\%) = \frac{n_o - n_f}{n_o} 100 \qquad \text{(eq. 5.1)}$$

where n_o is the initial amount of glycerol mols and n_f is the final amount of glycerol mols,

$$S(\%) = \frac{X \cdot n_d}{n_o - n_f} 100 \qquad \text{(eq. 5.2)}$$

where X is the stoichiometric constant with the following range of values: 2 for diglycerol, 3 for triglycerol, 4 for tetraglycerol and 5 for pentaglycerol; n_d is the amount of polyglycerol mols, n_o is the initial amount of glycerol mols and n_f is the final amount of glycerol mols.
Catalytic yield was calculated as follows (5.3):

$$Y(\%) = \frac{X_{glycerol}}{100} \Sigma S \qquad \text{(eq. 5.3)}$$

Where $X_{glycerol}$ is glycerol conversion and ΣS the sum of short-chain polyglycerol selectivity values. The presence of acrolein was qualitatively checked by gas chromatography.

5.3.4 Silylation derivatization reaction prior to polyglycerols analysis.

The silylation procedure was performed as follows: the sample (until 0,05 g) was taken from the final reaction mixture or calibration standard with a Pipette Pasteur and then placed in a small vial to cool off. With a glass stick (because of the viscosity) the sample is introduced into a test tube and weighted. Then, pyridine, HMDS, TMCS in a ratio 9:3:1 in excess (3462, 1154 and 385 µl, respectively) were added into. After TCMS was added, a white fume of ammonia was formed. The mixture was centrifuged for 3 minutes in a fume hood and then, left to settle down for 30 minutes. A precipitate was quickly formed. In a GC small vial, 100 of methyl laureate, used as internal standard, was added together with 1000 µl of the supernatant solution of the test tube, with the help of a micropipette.
The samples were introduced to the GC using an auto-injector. 3 µl of the solution were introduced by injection. Methanol was placed in another GC small vial to clean the column before and after each reaction sample run. The stability of the silylation reaction was tested, and it was concluded that it was stable even 5 h after it was prepared.

5.3.5 Gas chromatography set-up.

The following data belongs to the program used in the GC software to analyze the products of the reaction.

<u>SPL1:</u>
linear velocity
T: 523 K.
P: 87,1 KPa.
Total flow: 63,6 ml/min.
Column flow: 0,60 ml/min.
Linear velocity: 22,4 cm/s.

Purge flow: 3 ml/min.

Split ratio: 100.

Column:

T: 373 K.

Eq. time: 3 min.

Ramp conditions:

Table 5.4. Heating conditions for the column.

# Step	Rate (º)	Temperature (K)	Hold time (min)
0	-	373	1
1	10	563	10

FID1:

T: 613 K.

signal acquire: yes.

Sampling rate: 40 ms.

5.3.6 Calibration curves.

Using commercial reagents, a series of calibration curves were done in order to analyze the chromatographic results. Between 6 and 10 points were analyzed for each reagent; the weights ranged from 0 until 0,05 g. A micropipette and an analytical scale were used, together with test tubes. Each sample was silylized with the procedure seen in section 5.3.4. The commercial reagents used were: glycerol, diglycerol, triglycerol and the mixtures polyglycerol-3 and polyglycerol-4. In the following table the different calibration curves are summarized (table 5.5):

Table 5.5 Calibration curve data.

Compound	Commercial reagent name	equation	R^2	comments
glycerol	glycerol (Sigma-Aldrich)	y=3,5063x	0,99632	
diglycerol	diglycerol (Solvay)	y=2,7x	0,98868	
triglycerol	triglycerol (Sigma-Aldrich)	y=2,4792x	0,98013	80% of triglycerol in the reagent
tetraglycerol	polyglycerol-4 (Solvay)	y=1068,6x	0,7732	8% of pentaglycerol in the reagent
pentaglycerol	polyglycerol-3 (Solvay)	y=537,69x	0,96599	40% of tetraglycerol in the reagent

5.3.7 Characterization techniques.

For the characterizations techniques used in this chapter, the conditions can be found in Chapter 3.

5.4 Results and discussion.

5.4.1 Catalyst characterization.

Calcined MgAl layered double hydroxides (MgAl-LDHs).

The difractograms that belong to the two calcined MgAl-LDHs are similar (Figure 5.2). The only crystalline phase identified was periclase (MgO, JPDCS 89-4248) with a low degree of crystallinity since the peaks were quite broad. The peaks showed a certain shift compared to the pattern. This can be related to the presence of mixed oxides $Mg(Al)O_x$. However, some differences were observed in the values of FWHM, measured from the reflection (200), resulting in values of 2.43 and 1.91º for samples cHT-R18(333) and cHT-mw1(453), respectively.

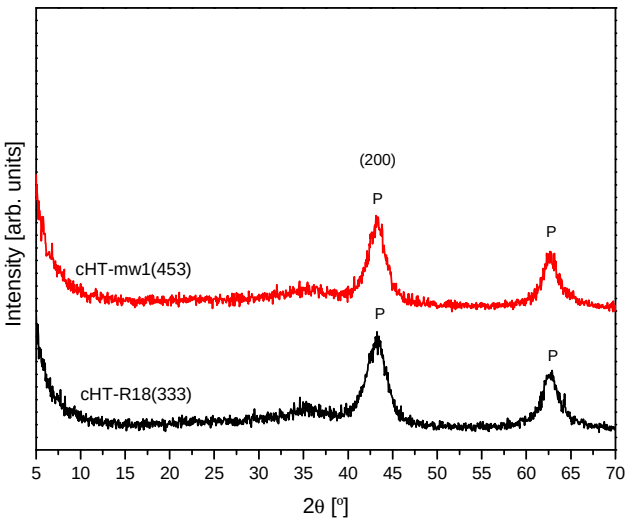

Figure 5.2. XPRD of the calcined MgAl-LDHs. P: periclase.

Therefore, some increase of crystallite size was obtained for the catalyst, the MgAl-LDHs precursor of which, was aged at 453 K for 1 h with microwave irradiation. Elemental analysis showed that the Mg/Al ratio for all calcined MgAl-LDHs was close to 3 in agreement with the expected stoichiometry.

Table 5.6 Characterization data for calcined MgAl-LDHs.

Catalyst	ICP (Mg/Al)	BET specific surface area (m^2/g)
cHT-R18(333)	3,00	237
cHT-mw1(453)	3,00	188

BET specific surface areas of calcined MgAl-LDHs were high (237 and 188 m^2/g, Table 5.6) due to the release of H_2O and NOx gases during MgAl-LDHs calcination with generation of porosity and disaggregation/breaking of the lamellae that involve the formation of small crystallites with mesoporosity, as previously reported [Bergadà *et al.* 2007b, Valente *et al*. 2010]. Catalyst cHT-mw1(453) had lower BET specific surface area than cHT-R18 (333) (Table 5.6) according to their higher crystallite size, as observed by XRPD. Figure 5.3a) and b) show TEM micrographs of samples cHT-R18(333) and cHT-mw1(453), respectively. After calcination, calcined MgAl-LDHs remind the former lamella structure. In general, the size of the particles were of less than 100 nm.

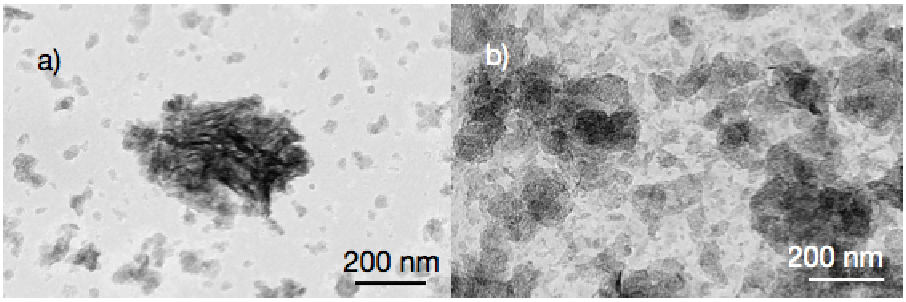

Figure 5.3 TEM micrographs of a) cHT-R18(333) and b) cHT-mw1(453).

Calcined CaAl layered double hydroxides (CaAl-LDHs).

The diffractograms of the four samples calcined at 723 K were similar, so only the diffractogram for sample cHC-mw1(453) is shown as representative. The diffractogram of sample cHC-mw1(453) (Fig. 5.4), corresponded to a very amorphous material.

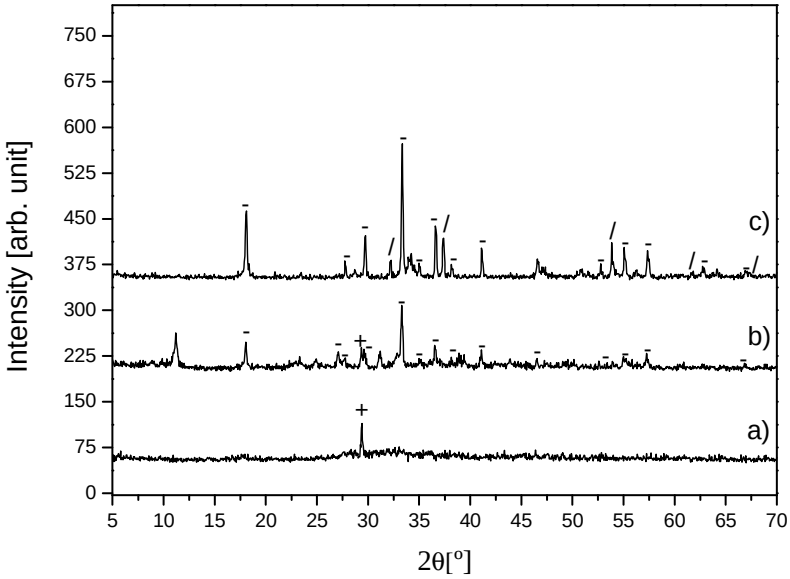

Figure 5.4 XPRD for samples cHC-mw1(453), cHC-mw1(453)/923 and cHC-mw1(453)/1073. (+): $CaCO_3$, (-): $Ca_{12}Al_{14}O_{33}$, (/): CaO.

However, a low intense peak, identified as calcite phase ($CaCO_3$, JPDCS file 072-1652), was observed. The appearance of calcite can be attributed to the calcination conditions in static air. In order to see the effect of calcination temperature, the hydrocalumite HC-mw1(453) was also calcined at 923 and 1073 K.

For the catalyst obtained by calcination at 923 K (cHC-mw1(453)/923), a new crystalline phase, identified as mayenite ($Ca_{12}Al_{14}O_{33}$, JPDCS file 48-1882), was observed in the diffractogram (Fig. 5.4). This is in agreement with the results previously reported for CaAl-LDH decomposition between 873 and 973 K [López-Salinas *et al.* 1996]. It was also possible to identify the calcite phase for this catalyst, although with less intensity than in cHC-mw1(453) since carbonate decomposition takes place from 873 K. When the temperature of calcination was raised to 1073 K (Fig. 5.4), a mixture of mayenite and lime (CaO, JPDCS 04-0777) was identified. If we compare the peaks of mayenite for samples cHC-mw1(453)/923 and cHC-mw1(453)/1073, peaks were broader for sample cHC-mw1(453)/923 due to its lower calcination temperature, since mayenite was completely crystallized at 1073 K.

Table 5.7. Characterization data for calcined CaAl-LDHs.

Catalyst	ICP (Ca/Al)	BET specific surface area (m^2/g)
cHC-R24(333)	1,99	15
cHC-R3(353)	1,94	22
cHC-Rmw3(353)	2,00	6
cHC-mw1(453)	1,84	3
cHC-mw1(453)/923	1,84	5
cHC-mw1(453)/1073	1,84	3

Elemental analysis showed that the Ca/Al ratio was close to 2 for all calcined samples (Table 5.7). Therefore, using different aging treatments in the preparation of CaAl-LDHs, we obtain catalysts with the expected stoichiometry.

BET specific surface areas were lower (between 3 and 22 m^2/g) than those of calcined MgAl-LDHs (Table 5.7). This is surprising considering the amorphous character of the samples calcined at 723 K. It is important to take into account that at 723 K, dehydroxylation (loss of water) and anion decomposition (loss of chloride) is partial [Rousselot *et al*. 2002] compared to MgAl-LDHs [Bussi *et al.* 2003]. This can also explain their lower BET specific surface area values.

For calcined MgAl-LDHs it has been observed that when the aging treatment is used with microwaves irradiation, BET specific surface areas are lower. We have observed the same for calcined CaAl-LDHs [Chapter 4] (Table 5.7). The lowest value was obtained for cHC-mw1(453) (3 m^2/g). In fact, the precursor of this sample presented the highest decomposition temperatures in the TGA analysis [Chapter 4].

By increasing the temperature of calcination at 923 K, the BET specific surface area increased from 3 to 5 m^2/g. In contrast, when the temperature of calcination was 1073 K, the value was again 3 m^2/g. Actually, a certain decrease of the area should be expected for the sample calcined at higher temperature due to crystallization and synterization processes [López-Salinas *et al*. 1996]. However, the differences between areas are irrelevant.

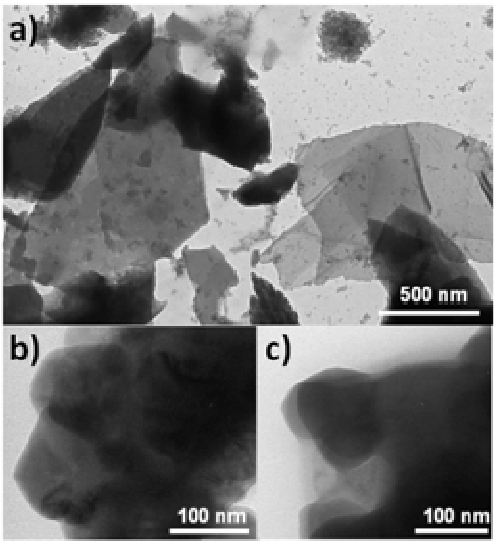

Figure 5.5. TEM micrographs of a) cHC-mw1(453), b) cHC-mw1(453)/923 and c) cHC-mw1(453)/1073.

Figure 5.5 shows TEM micrographies that correspond to a) cHC-mw1(453), b) cHC-mw1(453)/923 and c) cHC-mw1(453)/1073. The morphologies of samples calcined at 723 K were quite similar. The size of the particles are in the range of micrometers. These values agree with the lower BET specific surface areas obtained for calcined CaAl-LDHs. TEM micrographies of cHC-mw1(453)/923 and cHC-mw1(453)/1073 (Fig. 5.5b and 5.5c, respectively) showed smaller lamellae compared to Fig. 5.5a as a consequence of lamellae breaking during anion decomposition, together with a higher degree of agglomeration.
The different aging conditions used for MgAl-LDHs and CaAl-LDHs synthesis led to differences in the textural properties of the calcined samples, probably related to differences of their decomposition temperatures, studied in a previous work [Chapter 4].

5.4.2 Acid-base study.

Basicity of the catalysts.

Table 5.8 shows the maximum CO_2-desorption temperature peaks of calcined MgAl-LDHs. One peak at low temperature (T_{max} around 368 K), corresponding to the weak basic sites, was obtained for both samples. An additional less-intense peak, associated with medium basic sites, appeared at 598 K for cHT-R18(333) and at 648 K for cHT-mw1(453). The intensity was lower for the former sample. The first peak can be related to hydroxylated surface species whereas the second peak would correspond to oxide species obtained after the total decomposition of the hydroxide compounds [Bussi *et al*. 2003, Domínguez *et al*. 2011]. The higher desorption

temperature (648 K) and slight higher intensity observed for HT-mw1(453) could be explained by the presence of some stoichiometry defects in this sample, the precursor of which was prepared with microwaves. This second peak cannot be associated with residual $MgCO_3$ decomposition since in the TPD performed at the same conditions but without adsorption of CO_2, this decomposition peak was not observed.

Table 5.8. CO_2-TPD desorption temperatures (K). Band intensities: vw: (very weak), w (weak), m (medium).

Catalyst	T_{max}<393 (K) Weak basic sites	393<T_{max}<693 (K) Medium-strength basic sites	T_{max}>693 K Strong basic sites
cHT-R18(333)	366 m	598 vw	
cHT-mw1(453)	368 m	648 w	
cHC-R24(333)		531 w	
cHC-R3(353)		398 w	693 vw
cHC-Rmw3(353)		499 w	
cHC-mw1(453)		450 w,642 w	
cHC-mw1(453)/923		461vw	858 w
cHC-mw1(453)/1073		498 vw	928 w

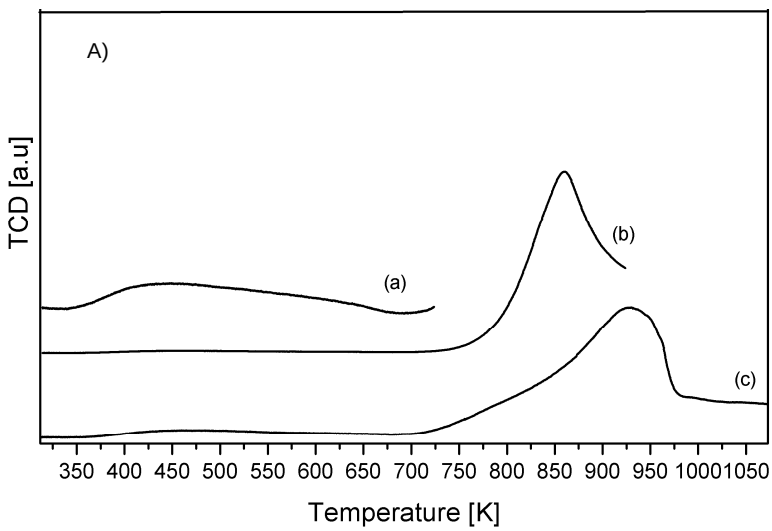

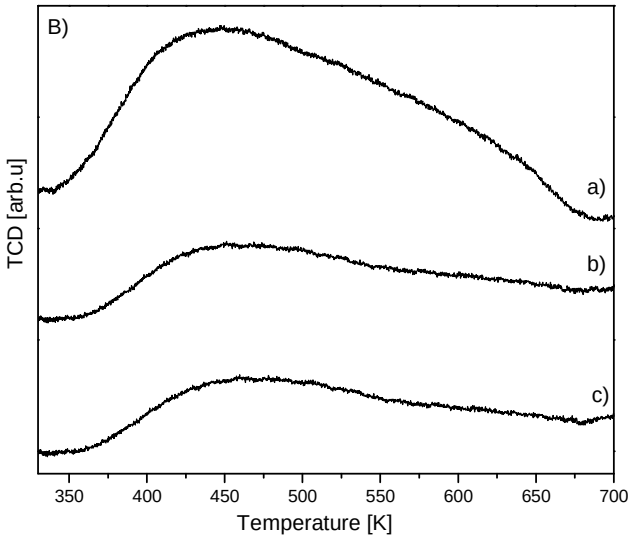

Figure 5.6. A) CO_2-TPD profiles for samples a) cHC-mw1(453), b) cHC-mw1(453)/923 and c) cHC-mw1(453)/1073. B) Detailed CO_2-TPD profile in the range 350-700 K.

For the CaAl-LDHs calcined at 723 K, the maximum CO_2 desorption temperature values were mainly between 499 and 693 K corresponding to medium basic sites (Table 5.8). These medium basic sites could correspond to O^{2-} ions adjacent to OH surface groups [López-Salinas *et al*. 1996], which in our samples could be adjacent to chlorine species. Additionally, a less-intense peak at 693 K was also observed for sample cHC-R3(353). This can be related to the lower anion decomposition temperature observed for this sample [Chapter 4] that could justify a more extended decomposition with loss of higher amount of chlorine. This is in agreement with the lower amount of chlorine detected for this sample (Table 5.9). The higher basicity of calcined CaAl-LDHs compared to calcined MgAl-LDHs can be interpreted by the presence of CaO, which has higher basicity than MgO. Actually, at 723 K a mixture of CaOHCl, CaO and Al_2O_3 in a ratio of 2:2:1 could be expected, as proposed in the literature from TGA experiments of Cl-hydrocalumites [Chapter 4, Domínguez *et al.* 2011]. Higher temperatures are necessary for a total dehydroxylation and anion decomposition, with the subsequent increase of the number of strong basic sites. The maximum CO_2 desorption temperature values for cHC-mw1(453)/923 and cHC-mw1(453)/1073 (Table 5.8) confirmed the presence of strong basic sites in these samples. The CO_2 desorption graphs of cHC-mw1(453), cHC-mw1(453)/923 and cHC-mw1(453)/1073 are shown in Figure 5.6 A), B).

These profiles were obtained by subtraction of the peaks recorded with and without CO_2, since some overlapping of the CO_2 desorption from the strong basic sites and $CaCO_3$ decomposition took place for the samples calcined at 923 and 1073 K.

The stronger basicity of these samples agrees with the higher calcination temperature used that involves the formation of isolated O^{2-} species in the mayenite and/or calcium oxide phases (Fig. 5.4) [López-Salinas *et al.* 1996, Aramendía *et al.* 2001].

Acidity of the catalysts.

The mass loss, in a TG experiment, associated with disruption of the base from acid sites was used to calculate the acid content in mmol of cyclohexylamine (CHA) per gram of sample following the method reported by Mokaya *et al.* [Mokaya *et al.* 1997]. From the first derivative of the thermogram, differences in the interaction CHA-acid site can be evaluated. The temperature corresponding to the minimum of the curve related to CHA loss can be considered a measure of the acid strength (Table 5.9). The acidity of calcined samples is a consequence of the presence of amorphous oxides with aluminum. The strength of the acidity can be modified by the amount of chlorine present in the amorphous material, due to its electronegative behavior [Constantino *et al.* 1995].

Table 5.9 Acidity characterization.

Catalyst	mmol cyclohexylamine/ g. catalyst	Temperature of cyclohexylamine desorption (K)	Chloride content (Cl/Al) atomic ratio
cHT-R18(333)	0.79	971	-
cHT-mw1(453)	0.15	978	-
cHC-R24(333)	0.53	1077	0.94
cHC-R3(353)	0.18	1070	0.72
cHC-Rmw3(353)	0.45	1077	0.92
cHC-mw1(453)	0.27	1084	1.02
cHC-mw1(453)/923	0.12	1053	0.56
cHC-mw1(453)/1073	<0.10	1044	0.46

For calcined MgAl-LDHs, the acid values were 0.79 and 0.15 mmol cyclohexylamine/g cat, for cHT-R18(333) and cHT-mw1(453), respectively (Table 5.9). The higher crystallinity of cHT-mw1(453) could explain its lower acidity, associated to a more saturated coordination of aluminum. The temperature of CHA loss is low (971 and 978 K, respectively) and can be related to low acidity strength.

The acidity values for calcined CaAl-LDHs were between 0.53 and <0.1 mmol cyclohexylamine/g. cat (Table 5.9). The lowest values (<0,1 and 0.12 mmol cyclohexylamine/g cat) corresponded to the samples HC-mw1(453)/923 and HC-mw1(453)/1073, which were calcined at 923 and 1073 K, respectively. An increase in the temperature of calcination supposed a decrease in the acidic content. Additionally, the amount of chlorine and the temperature of CHA loss also decreased when the calcination temperature increased (Table 5.9). These effects combined resulted in lower acidity content and lower acidity strength for cHC-

mw1(453)/1073. The differences observed between the CaAl-LDHs calcined at 723 K are difficult to explain, since all samples were very amorphous. However, in these group of samples, the catalyst with the lowest acidity (cHC-R3(353), 0.18 mmol cyclohexylamine/g cat) was synthesized from the CaAl-LDHs with the lowest temperature of dehydroxylation [Chapter 4] and probably with a faster formation of a microcrystalline aluminum oxide with less acidity. This sample also presented the lowest acid strength. Its lower amount of chlorine could justify again this fact. In the four samples of this group it is possible to establish a direct correlation between the chlorine content and the temperature of cyclohexylamine desorption cHC-mw1(453) >cHC-R24(333) >cHC-Rmw3(353) >cHC-R3(353).

The acidity will affect to the selectivity of the products of reaction, as acid sites catalyze the formation of acrolein, among other products (Schemes 5.5 and 5.6), and favor this parallel reaction of dehydration. Since the differences of basicity were not significant for the samples calcined at 723 K, catalysts with lower acid content will favor, *a priori*, the selectivity towards the products of interest short-chain polyglycerols.

5.4.3 Catalytic activity.

Calcined MgAl layered double hydroxides.

Catalyst cHT-R18(333) showed almost total glycerol conversion (96%) and low selectivity towards the products of interest (12 % DG+TG) (Table 5.10). This behavior can be related to an important contribution of the acidic content (0.79 mmol cyclohexylamine/g. cat) of this catalyst that favors acrolein formation. In contrast, catalyst cHT-mw1(453) exhibited low conversion (24%) and 100% selectivity towards (DG+TG) with less contribution of acidic content (0.15 mmol cyclohexylamine/g. cat). The differences in selectivity towards triglycerol for the two calcined MgAl-LDHs (3 and 11%, respectively) can be attributed to their differences in acidity, and also to the presence of higher amounts of medium-strength basic sites for the catalyst cHT-mw1(453) (Tables 5.8 and 5.9) resulting in a higher catalytic yield towards the products of interest.

Table 5.10 Catalytic results for calcined MgAl-LDHs. a: mainly acrolein.

Catalysts	Conversion (%)	DG Selectivity (%)	TG Selectivity (%)	Other products Selectivity (%)	Catalytic yield (DG+TG+TTG+PG) (%)
cHT-R18(333)	96	9	3	88[a]	12
cHT-mw1(453)	24	89	11	0	24

Calcined CaAl layered double hydroxides at 723 K.

The highest conversion (75%) was obtained for catalyst cHC-R24(333) (Table 5.11). In spite of the presence of medium-strength basic sites, the high acidic content of this catalyst (0.53 mmol cyclohexylamine/g. cat) favored mainly the formation of acrolein (selectivity to other products of 58%) rather than DG+TG selectivity (42 %).

Table 5.11 Catalytic results for calcined CaAl-LDHs.

Catalysts	Conversion (%)	DG Selectivity (%)	TG Selectivity (%)	Other products Selectivity (%)	Catalytic yield (DG+TG+TTG+PG) (%)
cHC-R24(333)	75	36	6	58[a]	32
cHC-R3(353)	40	50	14	36[a]	26
cHC-Rmw3(353)	64	35	10	55[a]	29
cHC-mw1(453)	60	44	11	45[a]	33

a: mainly acrolein.

Catalyst cHC-R3(353) led the highest value of DG+TG selectivity (64%). For this catalyst, the low acidic content (0.18 mmol cyclohexylamine/g. cat) and the presence of strong basic sites, favoured the formation of the products of interest (DG and TG). It is important to remark that cHC-R3(353) exhibited the highest % of TG selectivity (14%) of all catalysts calcined at 723 K. In contrast, catalysts cHC-Rmw3(353) and cHC-mw1(453) showed similar conversion values (64 and 60%, respectively) but cHC-mw1(453) presented higher selectivity to DG+TG (55%) than cHC-Rmw3(353) (45%) (Table 5.11). The different acidic content (0.45 and 0.27 mmol CHA/g. cat), together with the presence of medium basic sites with higher strength (maximum CO_2 desorption temperature at 642 K, Table 5.8) for catalyst cHC-mw1(453) justify these results. Figure 5.7A shows the correlation between acidity (mmol CHA/g cat), glycerol conversion (%) and short chain polyglycerols (DG+TG+TTG+PG) selectivity (%) for all catalysts. It is possible to observe that an increase of acidity involved an increase of conversion and a decrease of selectivity towards short chain polyglycerols.

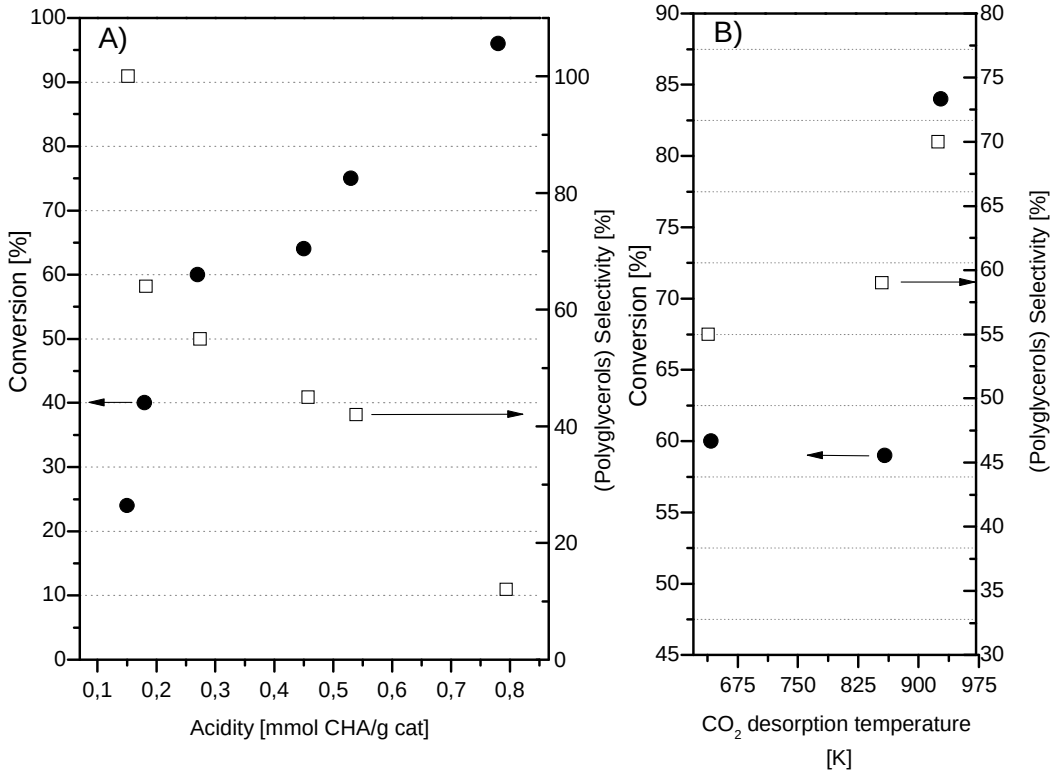

Figure 5.7. A) Correlation between acidity (mmol CHA/g. cat), glycerol conversion (%) and polyglycerols selectivity (%) for samples calcined at 723 K. B) Correlation between desorption temperature (K), glycerol conversion (%) and polyglycerol selectivity (%) for samples calcined at >723 K.

Effect of the calcination temperature.

In order to increase the basicity of the catalyst, HC-mw1(453) was calcined at higher temperatures (923 and 1073 K). For cHC-mw1(453)/923, conversion slightly decreased (59%) resulting in a similar selectivity towards DG+TG (51%) and the formation of tetraglycerol (Table 5.12).

Table 5.12. Catalytic results for CaAl-LDHs calcined at higher temperature.

Catalysts	Conversion (%)	DG Selectivity (%)	TG Selectivity (%)	Other products Selectivity (%)	Catalytic yield (DG+TG+TTG+PG) (%)
cHC-mw1(453)/923	59	38	13	49 (8% TTG)	35
cHC-mw1(453)/1073	84	29	20	51 (15% TTG + 6% PG)	59

The acidic content decreased when increasing the temperature of calcination to 923 K (0.12 mmol cyclohexylamine/g. cat) and at the same time, basicity strength increased since the maximum temperature of CO_2 desorption (858 K) corresponded to strong basic sites (Table 5.8), leading to higher TG selectivity (13%) and tetraglycerol formation (selectivity 8%). Interestingly, conversion (84%) as well as the degree of polymerization towards short-chain polyglycerols increased for catalyst cHC-mw1(453)/1073. The selectivity towards triglycerol was the highest observed (20%). The selectivity values for tetra- and pentaglycerol were 15% and 6%, respectively, with a total % yield to short-chain polyglycerols of 59%. For this catalyst, the amount of acidic content was the lowest (<0.1 mmol CHA/g. cat), and the strongest basic sites, as confirmed by CO_2-TPD analysis, where the desorption temperature achieved the highest value (928 K) for this catalyst.

Figure 5.7B) shows the correlation between the highest temperature value of CO_2 desorption vs. glycerol conversion and selectivity to polyglycerols for the CaAl-LDHs calcined at 723, 923 and 1073 K. The lower acidity content and stronger basicity, could explain the formation of higher weight polyglycerols. However, the acrolein formation was not totally avoided, since its low acidity content corresponded to medium acid sites, as deduced from the higher desorption temperature of cyclohexylamine obtained for this sample that was lower than those of the other calcined CaAl-LDHs but higher than those of calcined MgAl-LDHs (Table 5.9).

Stability of the catalyst.

In order to study the stability of the catalysts, XRD of the used catalysts were performed. The resulting patterns were similar to the patterns of the corresponding fresh catalysts. Calcium glycerolate phase was not observed in any case [Taylor *et al*. 1992]. Calcium glycerolate might appear as a result of an undesired secondary reaction and might block the pores of the catalyst, thus, decreasing the catalyst activity.

In order to discard homogeneous catalytic contribution to the results in our study, ICP tests were performed to the solution of the reaction, after its completion. The catalyst was recovered by

ultracentrifugation. Leaching was discarded since calcium and aluminum were not detected as part of the final solution.

Comparison to other published results.

The results shown in this work, regarding (DG+TG) catalytic yield, are similar to those published recently. In those results, the best catalytic yields towards (DG+TG) ranged between 33% using homogeneous LiOH as catalyst [Ayoub *et al*. 2012], around 33% using homogeneous $CsHCO_3$ [Richter *et al.* 2008], 40% with a Mg/Al calcined layered double hydroxide [García-Sancho *et al*. 2011] and 50% using a Mg/Fe calcined layered double hydroxide [Guerrero-Urbaneja *et al*. 2014]. However, it is remarkable the high catalytic activity of calcined CaAl-LDHs considering their low values of BET specific surface area (Table 5.7).

5.5 Conclusions.

A series of calcined Mg/Al-LDHs (cHTs) and calcined Ca/Al-LDHs (cHCs) were synthesized, characterized and tested for the etherification reaction of glycerol towards polyglycerols. The acid-base properties were correlated with their catalytic behaviour. All samples were active for the etherification reaction of glycerol towards short chain polyglycerols. For the CaAl-LDHs calcined at 723 K, the highest catalytic yield (DG+TG 33%) was obtained for sample cHC-mw1(453) after 24 h of reaction. This sample presented low acidity content, lower acidity strength in comparison with other CaAl-LDHs calcined at the same temperature and strong basic sites. Increasing the temperature of calcination supposed a decrease in chloride and acidity content, a decrease in the acidity strength and an increase of the basicity strength.
Catalyst cHC-mw1(453)/1073 achieved the highest catalytic yield to short chain polyglycerols (DG+TG+TTG+PG 59 %) of all samples. Regarding catalytic yield, results are similar to those published before for mixed oxides considering DG and TG % and higher when TTG and PG are included. It is important to remark the low values of BET specific surface area of the calcined CaAl-LDHs. The higher acidity strength of the CaAl-LDHs calcined at higher temperature with respect to that of the calcined MgAl-LDH HT-mw1(453) justifies the acrolein obtained in those samples in spite of their lower total acidity content. Catalysts were stable after reaction since glycerolate phase was not detected, by XRD, in any case. Contribution of homogeneous catalysis was discarded.

References for chapter 5.

[Aramendía *et al*. 2001] Aramendía M.A., Borau V., Jiménez C., Marinas J.M., Ruiz J.R. and Urbano F. J. **2001**, *Activity of Basic Catalysts in the Meerwein–Ponndorf–Verley Reaction of Benzaldehyde with Ethanol*, J. Coll. Interf. Sci., 238, 385-389.

[Ayoub *et al.* 2012] Ayoub M., Khayoon M.S and Abdullah A.Z. **2012**, *Synthesis of oxygenated fuel additives via the solventless etherification of glycerol*, Bioresour. Technol. 112, 308-312.

[Ayoub *et al.* 2013] Ayoub M. and Abdullah A.Z. **2013**, *LiOH-modified montmorillonite K-10 as catalyst for selective glycerol etherification to diglycerol*, Catal. Commun., 34, 22-25.

[Barrault *et al*. 2004] Barrault J., Clacens J.-M. and Pouilloux Y. **2004**, *Selective oligomerization of glycerol over mesoporous catalysts*, Top. Catal., 27, 137-142.

[Behr *et al*. 2008] Behr A., Eilting J., Irawadi K., Leschinski J. and Lindner F. **2008**, *Improved utilisation of renewable resources: New important derivatives of glycerol*, Green Chem., 10, 13-30.

[Bergadà et al. 2007] Bergadà O., Vicente I., Salagre P., Cesteros Y., Medina F. and Sueiras J.E. **2007**, *Microwave effect during aging on the porosity and basic properties of hydrotalcites*, Micropor. Mesopor. Mater., 101, 363–373.

[Bergadà *et al*. 2007b] Bergadà O., Salagre P., Cesteros Y., Medina F. and Sueiras J.E. **2007**, *Effective catalysts, prepared from several hydrotalcites aged with and without microwaves, for the clean obtention of 2-phenylethanol*, Appl. Catal. A Gen., 331, 19-25.

[Bergadà *et al.* 2007c] Bergadà O., Salagre P., Cesteros Y., Medina F. and Sueiras J.E. **2007**, *Adsorption of Carbon Dioxide in Several Aged Hydrotalcites and Calcined Hydrotalcites: Influence of Microwave Irradiation during the Ageing Step on their Basic Properties*, Adsorpt. Sci. Technol., 25, 143-154.

[Bruynes *et al.* 1982] Bruynes C.A and Jurriens T. K. **1982**, *Catalysts for silylations with 1,1,1,3,3,3-Hexamethyldisilazane*, J. Org. Chem., 47, 3966-3969.

[Bussi *et al*. 2003] Bussi J., López A., Peña F., Timbal P., Paz D., Lorenzo D. and Dellacasa E. **2003**, *Liquid phase oxidation of limonene catalyzed by palladium supported on hydrotalcites*, Appl. Catal. A Gen., 253, 177-189.

[Cavani *et al*. 1991] Cavani F., Trifirò F. and Vaccari A. **1991**, *Hydrotalcite-type anionic clays: Preparation,properties and applications*, *Catal. Today*, *11*, 173-301.

[Chai *et al*. 2007] Chai S.H., Wang H.P., Liang Y. and Xu B.Q. **2007**, *Sustainable production of acrolein: investigation of solid acid-base catalysts for gas-phase dehydration of glycerol*, Green Chem., 9, 1130-1136.

[Chheda *et al*. 2007] Chheda J.N., Huber G.W. and Dumesic J. A. **2007**, *Liquid-phase catalytic processing of biomass-derived oxygenated hydrocarbons to fuels and chemicals*, Angew. Chem. Int. Ed., 46, 7164-7183.

[Clacens *et al*. 1998] Clacens J.-M., Pouilloux Y., Barrault J., Linares C. and Goldwasser M. **1998,** *Mesoporous basic catalysts: comparison with alkaline exchange zeolites (basicity and porosity). Application to the selective etherification of glycerol to polyglycerols*, Stud. Surf. Sci. Catal., 118, 895-902.

[Clacens *et al*. 2000] Clacens J.-M., Pouilloux and Barrault J. **2000**, *Synthesis and modification of basic mesoporous materials for the selective etherification of glycerol*, Stud. Surf. Sci. Catal., 143, 687-695.

[Clacens *et al*. 2002] Clacens, J.-M, Pouilloux and Barrault J. **2002**, *Selective etherification of glycerol to polyglycerols over impregnated basic MCM-41 type mesoporous catalysts*, Appl. Catal. A Gen., 227, 181-190.

[Constantino *et al*. 1995] Constantino V.R.L. and Pinnavaia T.J. **1995**, *Basic properties of* $Mg^{2+}_{1-x}Al^{3+}_{x}$ *layered double hydroxides intercalated by carbonate, hydroxide, chloride, and sulfate anions*, Inorg. Chem., 34, 883-892.

[Corma *et al.* 1998] Corma A., Iborra S., Miquel S. and Primo J. **1998**, *Catalysts for the production of fine chemicals*, J. Catal, 173, 315-321.

[DeWoskin *et al*. 2003] DeWoskin R.S., Greenberg M., Pepelko W. and Strickland J. **2003**, *Toxicological review of acrolein*, US Environmental Protection Agency, Washington, DC.

[Di Cosimo *et al.* 1998] Di Cosimo J.I., Díez V.K., Xu M., Iglesia E. and Apesteguía C.R. **1998**, *Structure and surface and catalytic properties of Mg-Al basic oxides*, J. Catal., 178, 499-510.

[Domínguez *et al.* 2011] Domínguez M., Pérez-Bernal M.E., Ruano-Casero R.J., Barriga C., Rives V., Ferreira R.A.S., Carlos L.D. and Rocha J. **2011**, *Multiwavelength luminescence in lanthanide-doped hydrocalumite and mayenite*, *Chem. Mater*., *23*, 1993-2004.

[García-Sancho *et al.* 2011] García-Sancho C., Moreno-Tost R., Mérida-Robles J. M., Santamaría-González J., Jiménez-López A. and Maireles Torres P. **2011**, *Etherification of glycerol to polyglycerols over MgAl mixed oxides*, Catal. Today, 167, 84-90.

[Gholami *et al.* 2013] Gholami Z., Lee K.-T.and Abdullah A.Z. **2013**, *Glycerol etherification to polyglycerols using* $Ca_{1+x}Al_{1-x}La_xO_3$, J. Taiwan Inst. Chem. Eng., 44, 117-122.

[Gholami *et al.* 2014] Gholami Z., Abdullah A. Z. and Lee K.T. **2014**, *Heterogeneously catalyzed etherification of glycerol to diglycerol over calcium–lanthanum oxide supported on MCM-41: A heterogeneous basic catalyst*, Appl. Catal. A Gen., 479, 76-86.

[Guerrero-Urbaneja *et al*. 2014] Guerrero-Urbaneja P., García-Sancho C., Moreno-Tost R., Mérida-Robles J., Santamaría-González J., Jiménez-López A. and Maireles-Torres P. **2014**, *Glycerol valorization by etherfication to polyglycerols by using metal oxides derived from MgFe hydrotalcites,* Appl. Catal. A Gen., 470, 199-207.

[Knapp 1979] Knapp D.R. **1979**, *Handbook of analytical derivation reactions*, Wiley, New York.

[López-Salinas *et al.* 1996] López-Salinas E., Llanos Serrano M.E., Cortés Jácome M.A. and Schifter Secora I. **1996**, *Characterization of synthetic hydrocalumite-type* $[Ca_2Al(OH)_6]NO_3{\cdot}mH_2O$*: Effect of the calcination temperature*, J. Porous Mat., 2, 291-297.

[Mokaya *et al.* 1997] Mokaya R., Jones W., Moreno S. and Poncelet G. **1997**, *n-heptane hydroconversion over aluminosilicate mesoporous molecular sieves*, Catal. Lett, 49, 87-94.

[Othman *et al*. 2009] Othman M.R., Helwani Z., Martunus and Fernando W.J.N. **2009**, *Synthetic hydrotalcites from different routes and their application as catalysts and gas adsorbents: a review*, Appl. Organometal. Chem. 23, 335-346.

[Patent 1949] US Patent 2487208 A, *Preparation of diglycerol*, **1949**.

[Patent 1998] US Patent 5710350 A, *Process for the production of diglycerol*, **1998**.

[Patent 2002] US Patent 20020058781 A1, *Processes for preparing linear polyglycerols and polyglycerol esters*, **2002**.

[Patent 2008] EU Patent 1961726 A1, *Process for the conversion of glycerol and catalytically active material suitable therefore*, **2008**.

[Patent 2012] EU Patent 2491069 A2, *Production and composition of glycerol based polyols*, **2012**.

[Patent 2014] EU Patent 2754684 A1, *Method for the production of hyperbranched polyglycerol*, **2014**.

[Richter *et al.* 2008] Richter M., Krisnandi Y.K., Eckelt R., Martin A. **2008**, *Homogeneously catalyzed batch reactor glycerol etherification by* $CsHCO_3$, Catal. Commun., 9, 2112-2116.

[Rousselot *et al.* 2002] Rousselot I., Taviot-Guého C., Leroux F., Léone P., Palvadeau P. and Besse J.-P. **2002**, *Insights on the Structural Chemistry of Hydrocalumite and Hydrotalcite-like Materials: Investigation of the Series* $Ca_2M^{3+}(OH)_6Cl\cdot{}_2H_2O$ *(*M^{3+}*:* Al^{3+}*,* Ga^{3+}*,* Fe^{3+}*, and* Sc^{3+}*) by X-Ray Powder Diffraction*, J. Solid State Chem., 167, 137-144.

[Ruppert *et al.* 2008] Ruppert A.M., Meeldijk J.D., Kuipers B.W.M., Erné B.H. and Weckhuysen B.M. **2008**, *Glycerol etherification over highly active CaO-based materials: new mechanistic aspects and related colloidal particle formation*, Chem. Eur. J., 14, 2016-2024.

[Sivaiah *et al*. 2012] Sivaiah M.V., Robles-Manuel S., Valange S. and Barrault J. **2012**, *Recent developments in acid and base-catalyzed etherification of glycerol to polyglycerols*, Catal. Today, 198, 305-313.

[Solvay] Polyglycerols in industrial applications, Solvay chemicals website http://www.solvaychemicals.com/EN/products/Polyglycerols

[Solvay a] *Polyglycerols for food*, Solvay chemicals website http://www.solvaychemicals.com/EN/products/Polyglycerols

[Solvay c] *Polyglycerols for ester production*, Solvay chemicals website http://www.solvaychemicals.com/EN/products/Polyglycerols

[Solvay d] *Polyglycerols in personal care*, Solvay chemicals website http://www.solvaychemicals.com/EN/products/Polyglycerols

[Taylor *et al.* 1992] Taylor R.M., Slade P.G., Aldous G.L., Wilding I.R., Siddiqui O. and Whitehouse M.W. **1992**, *Preparation and Properties of a Glycerolatocalcium Complex*, Aust. J. Chem., 45, 1179-1185.

[Valente *et al*. 2010] Valente J.S., Hernandez-Cortez J., Cantu M.S., Ferrat G. and López-Salinas E. **2010**, *Calcined layered double hydroxides Mg–Me–Al (Me: Cu, Fe, Ni, Zn) as bifunctional catalysts*, Catal. Today, 150, 340-345.

[Vieille *et al*. 2003] Vieille L., Taviot-Guého C., Besse J.-P. and Leroux F. **2003**, *Hydrocalumite and Its Polymer Derivatives. 2. Polymer Incorporation versus in Situ Polymerization of Styrene-4-sulfonate*, Chem. Mater., 15, 4369-4376.

CHAPTER 6

Quantum dot-LED based on CdTe embedded in layered double hydroxides and clays

6.1 Introduction.

The introduction of this chapter covers the following topics: i) light-emitting devices based on quantum dots (QD-LEDs), ii) clays and iii) materials with luminescent properties. Regarding QD-LEDs herein are explained the main types in which these devices may be classified and some of the most important publications that report their assembly and characterization. Additionally, the main electronic conduction mechanisms are summarized for electronic devices. After this, a brief introduction about clays, which are materials used in this work, is given. Clays can contain nanoparticles with luminescent properties and thus be hybrid materials. Then, a classification of materials with luminescent properties is offered.

6.1.1 Architecture of a light-emitting diode (LED).

In a typical light-emitting device based on quantum dots, the emissive layer, which is the quantum dot film is sandwiched between the contacts: anode and cathode. ITO (indium tin oxide) is commonly used as anode. It is transparent to visible light and has a high working function. The anode injects holes into the HOMO level of the emissive layer. Typical metals are preferred with low work function, as they promote injection of electrons into the LUMO of the emissive layer.

Thus, the electrons are injected through the cathode and holes are injected through the anode. The quantum dots are electrically excited because a voltage is applied. The applied field makes that there is an electron-hole recombination in the emissive layer, and light is emitted trough the glass substrate.

Usually quantum dot LEDs (QDLEDs) have a similar architecture to that of organic LEDs (OLEDs).

To enhance the pass of holes and electrons several layers can be added to the architecture, always sandwiched between the cathode and the anode:

- Hole injection layer (HIL) and/or Hole transport layer (HTL): holes are injected through the anode, the HTL layer potentiates the mobility of the holes. It reduces the energy barrier for hole injection.
- Charge transport layer (CTL): the electrons are injected through the cathode, the charge transport layer potentiates the electron transport to the quantum dot film.

Figure 6.1a shows an architecture of a QDLED [Chen *et al*. 2014]. Figure 6.1b shows a schematic representation of the electron-hole recombination in a working QDLED that works as a p-n junction, like the devices assembled in this work.

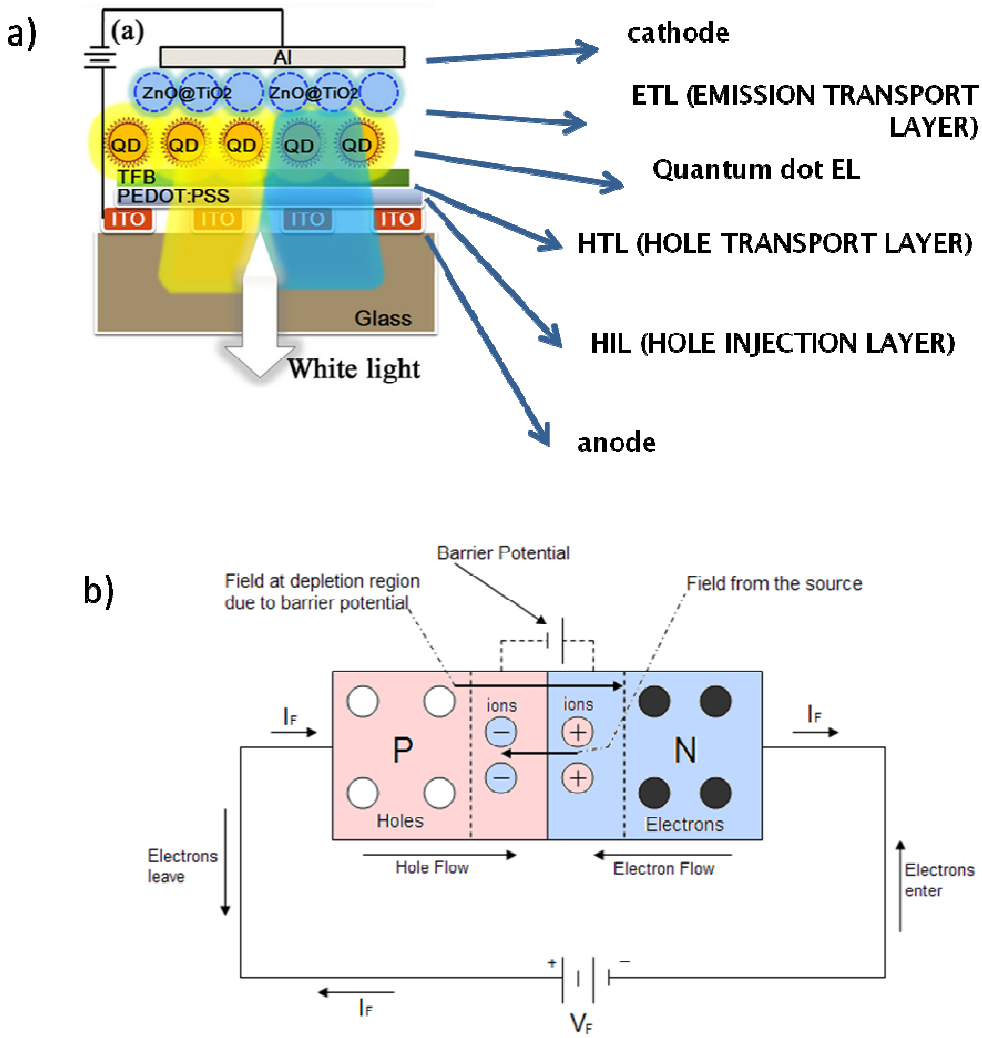

Figure 6.1. a) Representative architecture of a QDLED [Chen *et al*. 2014], b) Schematic representation of a QDLED that works as a p-n junction [Wikipedia website].

6.1.2 Types of QD-LEDs.

The first works that reported the use of quantum dots in light emitting devices started in the early 1990's. Of course, it's only since the early 1980's that quantum dots were first synthesized [Ekimov *et al*. 1981], as reported in the *Introduction* chapter 1.

We can divide the QD-LEDs according to their architecture in 5 main types:

- Type I: QD-LEDs with polymer as CTL (charge transport layer).

These were the first ever reported LEDs based on quantum dots. CdSe nanoparticles were sandwiched between the electrodes using a polymer bilayer [Colvin *et al.*1994]. The quantum

efficiencies were very low (<0,01%) but electroluminescence was achieved. Some of the electroluminescence was produced by the polymer, and so, the exciton formation was not completely efficient. The mechanisms involving the electroluminescence were believed to be charge injection, FRET (Förster resonance energy transfer) or both of them combined.

- Type II: QD-LEDs with organic small molecules as CTL (charge transport layer).

This kind of devices combined quantum dots and organic LEDs (OLEDs). A monolayer of quantum dots is inserted in the architecture of an OLED between two organic films. Efficiencies increased to 0,5% [Coe *et al*. 2002]. This increase was explained by the role of quantum dots used exclusively as an emissive layer. When quantum dots are also used as electron transport layer poor conduction may occur and therefore luminescent efficiency decreases. There were two processes to explain electroluminescence, direct charge injection or Förster energy transfer. In a later work, FRET was considered the main excitation mechanism for the quantum dots in many type II devices [Anikeeva *et al.* 2008]. Because organic molecules are incorporated into the architecture, encapsulation of the device is necessary to prevent from degradation on air [Burrows *et al.*1994].

- Type III: QD-LEDs with inorganic charge transport layer (CTL).

Looking to avoid organic materials that degrade on air, a new kind of devices emerged using inorganic materials as charge transport layers. Therefore this type of QD-LEDs presented a complete all-inorganic architecture. Mueller *et al*. first reported a device based on this architecture [Mueller *et al.* 2005]. Despite the fact that electroluminescence was achieved, low efficiencies arose (<0,01%). This fact led to an active research looking for alternatives. The use of metal oxides as CTL was reported by Caruge *et al.* [Caruge *et al.* 2008]. They used zinc tin oxide and NiO, however, efficiencies were <0,1%. Inefficiencies were explained by damage of the quantum dots during the sputtering of the oxide together with their quenching. In the last years, a new class of type III devices has arisen where the CTL is not present in the architecture [Wood *et al.* 2009, Cho *et al.* 2012]. They consist of a dielectric material with a layer of quantum dot in the center, sandwiched between the two contacts. They operate at high voltages.

- Type IV: QD-LEDs with hybrid inorganic-organic charge transport layers (CTL).

It works as a combination of types II and III. Usually it is formed by a layer of a metal oxide and an organic semiconductor. It has gained attention because of their quantum efficiencies (18%) and brightness [Mashford *et al.* 2013]. Quian *et al.* used solution-processed colloidal metal oxide nanoparticles as the electron transport layer [Qian *et al.* 2011]. Kim *et al.* fabricated a 4-inch display where the quantum dots where introduced by microcontact printing [Kim *et al.* 2011].

6.1.3 Basic electronic conduction processes in LEDs.

Devices are electrically characterized measuring the I-V (Intensity-Voltage) or J-V (Current density-Voltage) characteristics. After plotting the data obtained, it is possible to distinguish which conduction process is responsible for each voltage range applied. It is necessary to calculate the slope of each region of the curve. Comparing the values of the slope with the

presence or absence of linearity of the different processes, summarized in Table 6.1, will help to identify the conduction process.

Table 6.1. Basic conduction mechanisms [Sze *et al.* 2007].

Conduction process	Expression	Temperature dependence	Voltage dependence
Tunneling	$J \sim V exp\left[\frac{-2d\sqrt{2m^*\phi_B}}{\hbar}\right]$	none	$J \sim V$
Frenkel-Poole emission	$J \sim \frac{V}{d} exp\left[\frac{-q(\phi_B - \sqrt{q(\frac{V}{d})/\pi\varepsilon_i}}{kT}\right]$	$\ln(J) \sim \frac{1}{T}$	$ln\left(\frac{J}{V}\right) \sim V^{1/2}$
Ohmic	$J \sim \frac{V}{d} exp\left(\frac{-\Delta E_{ae}}{kT}\right)$	$\ln(J) \sim \frac{1}{T}$	$J \sim V$
Schottky emission	$J = A^* T^2 exp\left[\frac{-q(\phi_B - \sqrt{q(\frac{V}{d})/4\pi\varepsilon_i}}{kT}\right]$	$\ln(\frac{J}{T^2}) \sim \frac{1}{T}$	$\ln(J) \sim V^{1/2}$
Ionic conduction	$J \sim \frac{V}{dT} exp\left(\frac{-\Delta E_{ai}}{kT}\right)$	$\ln(JT) \sim \frac{1}{T}$	$J \sim V$
Space-chargelimited	$J = \frac{9}{8}\frac{\varepsilon_i \mu V^2}{d^3}$	none	$J \sim V^2$
Fowler-Nordheim tunneling	$J \sim \left(\frac{V}{d}\right)^2 exp\left[\frac{-4d\sqrt{2m^*\phi_B^{3/2}}}{3q\hbar V}\right]$	none	$ln\left(\frac{J}{V^2}\right) \sim \frac{1}{V}$

Notes: A*= effective Richardson constant, ϕ_B = barrier height, ε_i = insulator dynamic permittivity, *k*= Boltzmann's constant, $\hbar$= reduced Plank's, *m**= effective mass, *d*= insulator thickness, μ= charge carrier mobility, ΔE_{ai}= activation energy of ions, ΔE_{ae}= activation energy of electron.

Next, the mechanisms are explained [Sze *et al.* 2007]:

- Tunneling: it is the most common conduction mechanism. The tunnel emission is a result of quantum mechanics by which the electron wave function can penetrate through a potential barrier. It is independent of the temperature but dependent on the applied voltage.
- Frenkel-Poole emission: is due to the emission of trapped electrons into the conduction band. Electrons are supplied from the traps by thermal excitation. For trap states with Coulomb potentials, the expression is similar to that of Schottky emission. The barrier height is the depth of the trap potential as well. At low voltage and high temperature, current is carried by

thermally excited electrons hopping from one isolated state to the next. It yields an ohmic characteristic exponentially dependent on temperature.

- Ohmic: this mechanism is caused by the movement of mobile electrons in the conduction band and holes in the valence band. A linear relationship exists between the current density and the electric field. The magnitude of this current is very small. It could be observed if there is no significant contribution from other conduction mechanisms of current transport. It may be observed at low voltages in the (I-V) characteristics of devices [Chiu *et al.* 2014].
- Ionic conduction: is similar to diffusion process. The d_c ionic conductivity decreases during the time when the electric field is applied. After an initial current flow, positive and negative space charges will build up near the metal-insulator and the semiconductor-insulator interfaces, causing a distortion of the potential distribution.
- Space-charge limited: it appears as a result from carriers injected into a lightly doped semiconductor or an insulator, where no compensating is present. The current for the unipolar trap-free case is proportional to the square of the applied voltage. The mobility regime is relevant for this mechanism since mobility is typically very low in insulators. Further information regarding exponential trap distribution can be found elsewhere [Joung *et al.* 2010].
- Fowler-Nordheim tunneling: it occurs when the applied electric field is large enough so that the electron wave function may penetrate through the triangular potential barrier into the conduction band of the dielectric. The plot of the voltage dependent parameters (Table 6.1) should be linear. It is important to remember that even tough classical physics refer that when the energy of the incident electrons is less than the potential barrier, the electrons will be reflected, it is not the case in quantum mechanics, where the electrons may penetrate if the potential barrier is thin enough (<100 Å) [Chiu *et al.* 2014].

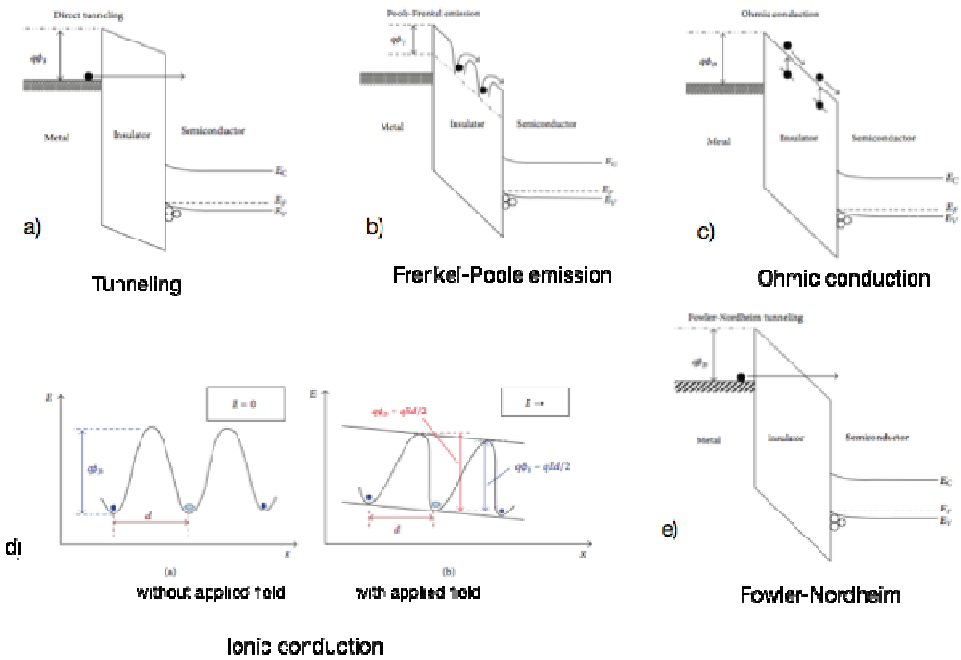

Figure 6.2 Energy diagrams for the main conduction mechanisms.

In figure 6.2, the band diagrams for some mechanisms are shown (extracted from ref [Chiu *et al.* 2014]).

6.1.4 Recent advances of QD-LEDs in published literature.

Wood and co-workers built different unipolar n-i-n light-emitting devices that operated via QD electrical excitation [Wood *et al.* 2010]. They introduced a thin film of ZnS at the charge transport layer to create a potential barrier for majority carriers limit charging of the QD layer. The architecture was based on ITO/ZTO ($ZnO:SnO_2$)/QDs/ZTO/ITO and then parallel structures introducing an additional layer of ZnS before or after the QDs. Different QDs were used: red CdSe/ZnS and green CdZnSe/CdZnS. They achieved transparency and detected electroluminescence from multicolored QDs. Luminescence was observed in voltages around between 10-15 V. They exhibit a luminance of 1040 Cd/m^2, recorded at a current density (J) of 92 mA/cm^2 and luminous efficiency of 1,1 Cd/A. They claimed that QD efficiency depended on the band gap energy of the QD. They demonstrated, additionally, that the device worked unpackaged, which was attributed to the stability of ZTO layers. They measure the devices for 40 days and they could detect luminescent response.

Sanchez and co-workers built a device with an inverted structure based on PbS-CdS quantum dots [Sanchez *et al.* 2014]. The architecture was FTO (SnO_2:F)/TiO_2/PbS/CdS/P3HT/Au. The

turn-on voltage was close to 1,2 V and the wavelength emission was detected in the red region of the visible spectrum. They compared the use of two capping agents for the quantum dots: TGA (thioglycolic acid) and MPA (3-mercaptopropionic acid). Charge carriers were injected into the QD layer and underwent radiative recombination. The stability of the device was studied as well, using different hole transport layers (HTL). The device was tested intermittently and showed that 50% electroluminescence dropped after 10 h.

Molaei and co-workers built a device based on CdS nanocrystals [Molaei *et al.* 2012]. The architecture was ITO/PEDOT:PSS/PVK/CdS-NCs/Al or Mg:Ag. The turn-on was around 7 V. The current density (J) reached 30 mA/cm^2 at 20 V of voltage. Wavelength emission was detected at around 550 nm, which is on the green-yellow boundary of white. Post-annealing was also studied. Electroluminescence increased when annealing of the nanocrystal layer was conducted. Current density then increased until 42 mA/cm^2 at 20 V of voltage. They claimed that annealing resulted in leveling of the layers and in a decrease of the roughness, which could affect the hole transport. When the cathode was substituted for Mg:Ag, the turn-on voltage was of 6 V and current density (J) reached 50 mA/cm^2 at 18 V. Brightness increased to 13 Cd/m^2 at 15 V. Luminescence was blue-shifted, which was attributed to the higher Fermi level of Mg:Ag cathode.

Stouwdam and co-workers built a device based on CdSE/ZnS and CdSeS/ZnS core-shell QDs [Stouwdam *et al.* 2008]. The architecture was ITO/PEDOT:PSS/PVK/CdSe/ZnO/Al or Ag. They studied the presence of ZnO and its different thickness. The emission peak was around 620 nm when ZnO is present. Luminous efficiency ranged around 0,1 Cd/A. In its absence, the main emission contribution is dominated from the PVK (420 and 490 nm), with poor emission of the QDs. Turn-on voltages ranged between 5,5 V and 8 V (the later without ZnO). ZnO facilitated electron injection in the QD layer. The behaviour of the devices was explained by trap limited current ($J \sim V^n$ with $n \sim 8$). The best luminous efficiencies achieved were 0,30 Cd/A for the red, 0,65 Cd/A for the green and 0,03 Cd/A for the blue.

Bendall *et al.* reported on an hybrid LED where the quantum dots, CdTe, were embedded in an inorganic matrix [Bendall *et al.* 2010]. The architecture was ITO/(LDH/CdTe)$_n$/Al. The layered double hydroxides used, a hydrotalcite, was delaminated to produce positively charged nanoplatellets. The CdTe was capped with thioglycolic acid, thus, being negatively charged. They performed 10 alternated depositions. Turn-on voltage was at 3-4 V with a current density (J) of 0,04 A/cm^2. They achieved luminescence efficiency at 8,42 Cd/A when current density (J) was of 0,02 A/cm^2. The emission was centered at 637 nm. This peculiar architecture with CdTe QDs embedded in delaminated LDH worked as a scaffold that prevented from nanoparticle aggregation. They suggested that the mechanism occurred through electron-hole recombination in the quantum dot and that conduction through the composite took place by hopping mechanism mediated by quantum-tunneling through the sheets. This work opened the possibility to build LEDs based upon QDs with inorganic matrixes.

6.1.5 Clay minerals.

Clay minerals can be an interesting matrix to be used in the architecture of light-emitting diodes based on quantum dots. Clay minerals can be divided in cationic clays and anionic clays. Cationic clays are named, in general, clays. Anionic clays, also called layered double hydroxides, have been previously described in previous chapters of this thesis.

Clay minerals form an important group of the phyllosilicate family of minerals, which are distinguished by layered structures composed of polymeric sheets of SiO_4 tetrahedra (T) linked to sheets of (Al, Mg, Fe)$(O,OH)_6$ octahedra (O) (Fig. 6.3). They present high specific surfaces and have ion-exchange properties. They have been used since pre-historical times. Their applications include from pottery, ceramics, nanocomposite materials, oil drilling, waste isolation and they can be used in the metal and paper industries. Some chemical applications include their use as adsorbents, decolorizing agents, ion-exchangers… [Kloprogge *et al.* 1999, Zhang *et al.* 2010]. Saponites and hectorites are common clays of mineral group smectites, with a distribution of sheets T:O:T. Delamination of clays is an interesting process to increase the surface area which can be of interest for catalytic applications [Sánchez *et al.* 2013, Gebretsadik *et al.* 2014].

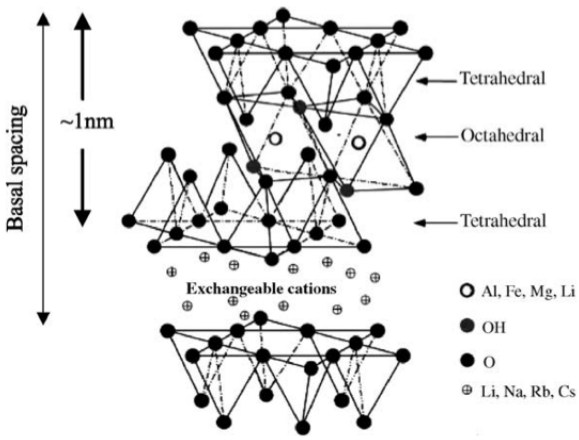

Figure 6.3 Structure of T:O:T phyllosilicates [Ray et al. 2003].

Saponites have theoretical formula $[Si_{8-x}Al_x]^T$ $[Mg_6^{2+}]^o$ $O_{20}(OH)_4$ $[M_x^+]\cdot nH_2O$ and can be synthesized using different procedures. Smectites can be extracted from nature, but they present impurities and purification procedures can be tedious, the synthesis procedure in laboratory facilities are cost-effective and easy. They avoid the disadvantages of natural clays and their properties, such as chemical composition, textural properties and cation exchange capacity can be controlled [Trujillano *et al.* 2011]. The success of hydrothermal techniques to obtain pure products is due to the high hydrolysis rates of octahedral cations at high temperature, which favor nucleation and growth of saponite materials [Bisio *et al.* 2008].

Therefore, it is possible to find many reported works for saponites synthesis [Kloprogge *et al.*1999, Bisio *et al.* 2008, Vicente *et al.* 2010, Trujillano *et al.* 2009 and 2011, Zhang *et al.* 2010]. Hectorites, with formula $[Si_8]^T$ $[Mg_{6-x}Li_x]^O$ $O_{20}(OH)_4$ $[M_x^+]\cdot nH_2O$, are synthesized using freshly prepared $Mg(OH)_2$ since in a first step silica monomers condense over brucite sheets [Vicente *et al.* 2009].

6.1.6 Suitable materials for luminescent applications.

Different materials are of interest in order to combine their structural with their luminescent properties. In this section, some of these materials are summarized:

- Hybrid organic-inorganic (O-I) nanocomposites: they are materials that combine properties of organic and inorganic materials. They have a high versatility in their chemical and physical properties. The conditions obtained by the sol-gel process concede the mixture of O-I components (i.e low temperatures, organic solvents, metal-organic precursors…). Some of their applications include the industry of photonics. Solid-state dye-laser hybrid materials, for example, are used as lasers and in pumped amplifiers. For the case of solid-state dye lasers, usually they are based on a dye in an inorganic host. The use of hybrid materials for these applications offers important positive aspects, such as improving matrix characteristics like hydrophobicity, density and mechanical resistance. Additionally, they offered longer lifetimes and operate at higher repetition rates, than inorganic xerogels or organic polymer hosts [Scott *et al.* 2001, Sanchez *et al.*2003, Sanchez *et al.* 2011].
- Electroluminescent hybrid materials: since the report of bright emission from dye films there is an important interest of their use in LEDs (light emitting devices). Functionalized alkoxysilanes are used for building hybrid LEDs. There is versatility in the design, efficient cross-linking through condensation reactions that offer chemical stability and the fact that they form insoluble films prevent from swelling and leaching. Because of these reasons, they are used as well as traditional low molecules, conjugated polymers or molecules dispersed in polymeric matrixes, among others. Some examples of HLEDs can be found elsewhere [Morais *et al.* 1999, Sanchez *et al.* 2003, Pandey *et al.* 2011, Kamino *et al.* 2013].
- Lanthanide-doped hybrid materials: Rare earth doped materials are of interest for the field of devices and optics because of the wide range of applications, such as lasers. Usually they are synthesized by the sol-gel process, through the hydrolysis of tetravalent metal alkoxides. The lanthanide is doped by dissolving the rare-earth in the initial sol. Some drawbacks include the formation of aggregates and quenching that decrease the luminescence and should be avoided by the design of the resulting hybrid compound [Sanchez *et al.* 2003, Carlos *et al* . 2009].
- Quantum dot-clay composites: As commented in the Introduction chapter, quantum dots (QDs) show unique size-dependent photoluminescence. They are used for a wide range of applications, that range from optoelectronics devices to medical treatments, among others

[Chapter 1]. When QDs are inserted into the structure of clays, they are constrained in the layered structure of clays and their properties stay stable. This clay environment prevents the quantum dots to be damaged under air conditions [Gao *et al.* 2011, Xie *et al.* 2011, Cao *et al.* 2012]. Many metals and semiconductors have been incorporated into the structure of clays [Belova *et al.* 2009, Khaorapapong *et al.* 2010, Zhang *et al.* 2010]. It is crucial that the disposition of the QDs is not in an agglomerated form, since it can lead to quantum efficiency problems in solar cells, for example. QDs dispersed in inert clays can help to prevent them from aggregation if they are well dispersed in clays. Following photoluminescence applications, organic molecules have also been introduced into the structure of layered clay minerals [Neumann *et al.* 2002, Ferreira *et al.* 2013].

- Hybrid layered double hydroxides: As commented in the Introduction chapter, layered double hydroxides, whose properties can be easily tuned, offer enormous spectra of applications when optical luminescent are needed. LDH are useful host matrixes where the quantum dots can be embed in order to prevent from QDs aggregation and/or later release from the matrix structure, similarly to composites with clays, mentioned before. LDHs can have optical transparency and in many cases they improve photostability to the QDs. Additionally, their synthesis is cheap. Their applications include optoelectronic devices, delivery of drugs, markers for biological use and many more [Liang *et al.* 2012, Stoica *et al.* 2012, Chen *et al.* 2013, Cho *et al.* 2013, Cho *et al.* 2013b].

6.2 Aims of this chapter.

The aims of this chapter are:

- To synthesize and characterize hybrid materials that could be candidates as emissive layers in optoelectronic devices. We are interested mainly in LEDs. These hybrid materials are smectite clays (hectorites and saponites) intercalated with capped-CdTe quantum dots.
- To synthesize and delaminate layered double hydroxides materials (with the following metals: CaAl and NiAl) to produce films that will be alternated with layers of capped-CdTe quantum dots, and later tested as candidates for emissive layers in optoelectronic devices.
- To build LEDs based on these emissive layers and characterize their electrical characteristics. In order to make a cost-effective process, the assembly is performed under air conditions (with humidity, RT and presence of dust) outside the glovebox.

During the assembly of the devices, we have studied four main variables:
- type of emissive layer matrix (delaminated layered double hydroxide or hybrid clay).
- number of alternated depositions of the layers that form the emissive layer.
- type of metal deposited as cathode (Al or Ca/Ag).
- post-annealing (after the deposition of the thiol-capped CdTe quantum dots).

6.3 Experimental procedure.

The experimental section is divided in four main parts:

- The quantum dots used in this work are described, which are thiol-capped CdTe nanoparticles that are negatively charged.
- The synthesis of hybrid materials with luminescent properties is reported. These hybrid materials are layered double hydroxides and clays where the thiol-capped CdTe nanoparticles are embedded.
- The synthesis of the inorganic matrixes where the thiol-capped CdTe nanoparticles will be embedded and form the emissive layer of the luminescent devices. The inorganic matrixes are delaminated layered double hydroxides and clays. As deposited films, these materials will be part of the emissive layer of the luminescent devices, alternated in films with the thiol-capped CdTe nanoparticles. The delaminated layered double hydroxides will be positively charged and because of the electrostatic interactions, the thiol-capped CdTe nanoparticles will not aggregate and be homogeneously deposited. The delaminated clays will be negatively charged. In order to interact with the thiol-capped CdTe nanoparticles and to prevent from nanoparticle aggregation, a film of a cationic polyelectrolite (PDDA), which is positively charged, is sandwiched between the clay film and the CdTe film to enhance the conduction of the electrons.
- The assembly of the light emitting devices is reported, covering all the steps from the cleaning of the glass substrates until the cathode deposition. The emissive layer of these devices is consisted in film depositions of inorganic materials in their delaminated form and the film deposition of the thiol-capped CdTe nanoparticles solution. Four parameters are studied for these devices: i) the nature of the inorganic matrix, ii) the number of alternated depositions, iii) the type of cathode and iv) post-annealing prior to cathode deposition.

6.3.1 Thiol-capped CdTe nanoparticles.

The thiol-capped CdTe quantum dots used in this thesis were of sizes that ranged 2,5-5 nm and their emission peak was centered at 630 nm. The nanoparticles were obtained from two sources. Firstly, they were purchased from *MkNano* (www.mknano.com). In the second part of the thesis they were supplied by the research center *Centro Nanosistemi*, in Alessandria, Italy, with the same properties. Figure 6.4 shows a representation of a capped CdTe quantum dot.

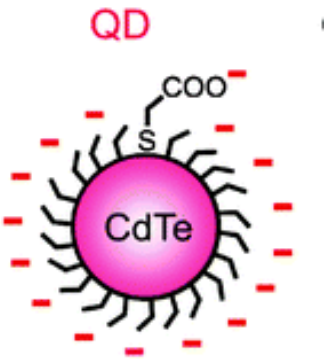

Figure 6.4 Representation of a CdTe capped quantum dot [Gaponik *et al.* 2010].

6.3.2 Hybrid materials with potential luminescent properties.

Synthesis of a CaAl layered double hydroxides with thiol-capped CdTe nanoparticles.

A hydrocalumite was directly synthesized with CdTe nanoparticles following the procedure explained in section 4.3.1 of Chapter 4 and adding 100 µl of a colloidal solution of CdTe ($1 \cdot 10^{-5}$ M) that were supplied by Centro Nanosistemi, Alessandria, Italy. After complete addition of the salts and the nanoparticles, it was aged for 24 h at 333 K. The sample was recovered by centrifugation at 7000 rpm and stored in a desiccator. This sample is labelled hHC-Cl.

Synthesis of hybrid oriented and delaminated saponites

Firstly, saponites are synthesized**.** The synthesis of oriented saponite is done following the work of Trujillano *et al.* but with some modifications [Trujillano *et al.* 2011]. The synthesis starts with the preparation of the buffer solution to achieve pH=13: 10,9 g of NaOH were mixed with 19,7 g of $NaHCO_3$ in 150 ml of deionized H_2O. The buffer solution is stirred for 10 min. Then, 16,8 ml of sodium silicate solution are added. The solution is stirred for 30 min. In the meantime, the Al&Mg solution is prepared by mixing 6,93 g. of the nonahydrated nitrate aluminum salt and 23,73 g. of the hexahydrated nitrate magnesium salt in 15 ml of deionized water. The salts solution was placed in a buret and dropped slowly into the buffer solution with sodium silicate. After complete addition of the salts, the solution was agitated using a tip sonicator for 30 min (70% duty cycle and 7,0 output). The hydrothermal treatment was performed in autoclave for 72 h at 453 K. After the hydrothermal treatment, the sample was recovered by filtration and dried in an oven overnight (353 K). This sample is labelled SAP.

The synthesis of the delaminated saponite was done following a methodology reported elsewhere [Gebretsadik *et al.* 2014]. In a beaker with 200 ml deionized water, 7 ml of NH_3 were

added. The solution was agitated for 5 min. Then 5,41 g of fumed silica were added. 30 min later, 2,56 g of aluminum acetate were added, and 30 min later 16,94 g of magnesium acetate were added as well. The final solution was agitated for 30 min with a tip sonicator (70% duty cycle and 7,0 output). 7 ml of NH_3 were added and the solution was left for agitation for 5 min. The hydrothermal treatment was done by the use of microwave radiation for 6 h. at 453 K. After the hydrothermal treatment, the sample was recovered by filtration and dried in an oven overnight (353 K). This sample is labelled dSAP.

Two types of hybrid clays were prepared:

- SAP-HDTMA-CdTe: The oriented saponite was exchanged with hexadecyltrimethylamonium bromide (HDTMA) and CdTe nanoparticles. 1 g of ordered saponite was exchanged with 0,2 g of HDTMA and were placed in a beaker with 50 ml of deionized water. The solution was agitated for 24 h at RT. Then, the solution was filtered and dried overnight (353 K). The addition of the nanoparticles was performed by mixing 0,1 g. of the saponite exchanged with HDTMA with 40 µl of the thiol-capped CdTe nanoparticles and placed in a beaker with 10 ml of deionized water. An additional exchange was done using 0,5 g of saponite with 2000 µl of the CdTe nanoparticles. The solutions were agitated for 2 h at RT. Finally, they were recovered by centrifugation at 7000 rpm for 8 min. The solids were dried overnight (323 K). These samples were labelled as SAP-HDTMA-CdTe(A) and SAP-HDTMA-CdTe(B), respectively.

- dSAP-PDDA-CdTe: This delaminated saponite was exchanged with poly(diallyldimethylammonium chloride) solution (20 wt. % in H_2O) (PDDA) and CdTe nanoparticles. The exchange was done by adding 5 g of the PDDA solution to 0,5 g of dSAP and was agitated for 24 h at RT. The exchanged clay was recovered by centrifugation at 8000 rpm for 8 min (repeated twice). The wet exchanged clay was diluted in 100 ml of deionized water and agitated for 5 min. A portion of 30 g. was transferred to a small beaker where 200 µl were added. The solution was left overnight with agitation. Then, the solution was recovered by centrifugation at 7000 rpm for 10 min (repeated twice). The recovered solid was dried in an oven overnight (333 K). This sample is labelled dSAP-PDDA-CdTe.

6.3.3 Synthesis of the inorganic matrixes for the emissive layer of the luminescent devices.

Synthesis and delamination of CaAl layered double hydroxide.

The synthesis and aging conditions of CaAl layered double hydroxide (CaAl-LDH) used in this chapter (HC-NO_3) is reported in Chapter 4, section 4.3.2. The delamination procedure is

explained in Chapter 4, section 4.3.5. The nitrate hydrocalumite is labelled HC-NO_3 and the delaminated sample dHC-NO_3.

Synthesis and delamination of NiAl layered double hydroxide.

A NiAl-LDH, named *takovite*, has been synthesized following this procedure: two 50 ml burets were placed on a 500 ml round-bottom flask, located on a stirring mantle. A 50 ml solution of the nitrate salts, keeping a Ni:Al ratio 4:1, was prepared and placed in a buret, whilst in the other a 1 M solution of NaOH was added (usually 200 ml of caustic soda solution are prepared). In the round-bottom flask we add 40 ml of a 0,01 M solution of NaOH. The procedure was done at constant pH of 8, with vigorously stirring and at RT. N_2 was bubbled during the process to avoid CO_2 incorporation. When the addition of the salts is completed, a hydrothermal treatment is applied to the solution. For this sample, the hydrothermal treatment was done by refluxing in a round-bottom flask for 18 h at RT. N_2 was also bubbled during the hydrothermal treatment. This sample is called NiAl-LDH.
The same methodology explained at Chapter 4, section 4.3.5 was followed to achieve delamination for sample Ni/Al-LDH. A 10 ml solution of 1mg/ml of the *takovite* sample is prepared using formamide as solvent (more quantities of solution could be prepared depending on the number of devices to be built). The solution was placed in a sealed vial, previously purged with N_2. 5 cycles of 30 min of ultrasounds were needed to delaminate this sample. No sediment was observed after this process. The delaminated sample is labeled dNiAl-LDH.

Synthesis of delaminated hectorite.

The synthesis of delaminated hectorite was done following a methodology reported elsewhere [Sánchez *et al.* 2013]. In a beaker, 8,73 g. of sodium silicate solution, 5,18 g. of dehydrated magnesium chloride and 0,1 g. of lithium fluoride were place with 43,65 ml of acid nitric 1M. We placed in a buret a solution of lithium hydroxide 1 M (usually, 200 ml are prepared), which will be added slowly to the solution of the salts until reaching pH= 10. The final solution is agitated, by the use of ultrasounds, for 20 min. Then, the solution is filtered and the solid recovered, dried overnight (353 K). With the recovered solid, a solution (10% wt.) is prepared in deionized water. Then, trimethyldodecylammonium chloride (AQ) is added in a ratio 1:1 (to lithium). The solution is agitated for 30 min. The hydrothermal treatment is performed using microwave radiation in autoclaves for 1 h. at 453 K. After the hydrothermal treatment, the sample was recovered by filtration and dried in an oven overnight (353 K). Finally, the sample is placed in a quartz reactor and calcined for 75 min. at 893 K under air flow (1ml/s). This sample is labelled dHEC.

6.3.4 Assembly of the luminescent devices.

The assembly of the luminescent devices is divided in the following steps: cleaning of the glass substrates patterned with ITO, deposition of PEDOT:PSS, deposition by spin coating of the films that compose the emissive layer and finally, the cathode is deposited by vacuum evaporation.

a) Cleaning of the glass substrates patterned with ITO.

The glass substrates with patterned ITO were purchased, with a sheet resistances of15 Ω/□. The ITO had a thickness of 120 nm. Because they were packaged with a protective resin, firstly it should be removed with regular acetone. Then, the cleaning procedure proceeded as follows for each substrate (the solvents used were of electronic grade):

- Carefully with commercial *decon90* soap and a soft sponge, then rinsed with regular water, then plunged in a beaker with Milli-Q water. Each substrate was dried with a compressed-air gun and placed in a substrate-teflon holder covered with a beaker upside-down, for dust protection.
- The holder was transferred to a beaker, filled with acetone and placed in an ultrasound bath for 10 min.
- Then, the holder was transferred to a beaker, filled with methanol and placed in an ultrasound bath for 10 min.
- Then, the holder was transferred to a beaker, filled with isopropanol and placed in an ultrasound bath for 10 min.
- Then, the holder was transferred to a beaker, filled with Milli-Q and placed in an ultrasound bath for 10 min.
- Then, each substrate was plunged in Milli-Q water three times and dried with a compressed-N_2 gun. Finally, the clean glass substrate was stored in a glass petri-box and stored in the oven at 393 K.

The electronic grade solvents were recycled for laboratory use. The beakers were labelled for each solvent. All the handling was done with non-scratching tweezers. Each holder could hold up to 9 glass substrates. All clean substrates were stored always in the oven in a glass petri-box. The pattern is designed in a way that each device presents 4 pixels of 9 mm^2.

b) Deposition by spin-coating of the emissive layers in the devices.

In this work, different architectures for the emissive layer were tested. Only those devices from where light emission was detected are reported here.

Before the emissive layers were deposited, PEDOT:PSS was deposited in all glass substrates by spin-coating. A 0,20 µm pore diameter filter was connected to a syringe in order to discard any agglomeration. The PEDOT:PSS was deposited using this syringe. The program had two steps, step 1) at 4500 rpm for 30 s and 2) at 3500 rpm for 30 s with an acceleration in both

cases of factor 11 (1232 rpm). Then, the substrate was baked for a minimum of 20 min in an oven (393 K). All substrates with coated PEDOT:PSS were stored always in the oven in a glass petri-box.

Devices based on delaminated layered double hydroxides and thiol-capped CdTe nanoparticles.

The solution of the delaminated layered double hydroxide was directly used for spin-coating. The concentration was 1 mg/ml using formamide as solvent. The solution of thiol-capped CdTe nanoparticles was diluted 1/2 in Milli-Q water. A 0,40 µm pore diameter filter was connected to a syringe in order to discard any agglomeration.

The spin-coating parameters for this family of devices are summarized next:

- Delaminated LDH films: 2500 rpm for 60 s.
- CdTe films: 3000 rpm for 30 s.

For devices that were post-annealed, it was performed in two ways: after each CdTe film deposition or after the last film was deposited for each device. It was done for 5 min at 393 K.

In Table 6.2 the parameters for each device are summarized:

Table 6.2. Parameters for devices based on delaminated LDHs.

Architecture	inorganic matrix	# alternated depositions (*n*)*	cathode	post-annealing
ITO/PEDOT:PSS/(dHC:CdTe)$_1$/Al	dHC-NO_3	1	Al	no
ITO/PEDOT:PSS/(dHC:CdTe)$_2$/Al	dHC-NO_3	2	Al	no
ITO/PEDOT:PSS/(dHC:CdTe)$_3$/Al	dHC-NO_3	3	Al	no
ITO/PEDOT:PSS/(dHC:CdTe)$_5$/Al	dHC-NO_3	5	Al	no
ITO/PEDOT:PSS/(dHC:CdTe)$_3$/Al	dHC-NO_3	3	Al	yes
ITO/PEDOT:PSS/(dHC:CdTe)$_5$/Al	dHC-NO_3	5	Al	yes
ITO/PEDOT:PSS/(dHC:CdTe)$_1$/Ca/Ag	dHC-NO_3	1	Ca/Ag	no
ITO/PEDOT:PSS/(dHC:CdTe)$_3$/Ca/Ag	dHC-NO_3	3	Ca/Ag	no
ITO/PEDOT:PSS/(dHC:CdTe)$_5$/Ca/Ag	dHC-NO_3	5	Ca/Ag	no
ITO/PEDOT:PSS/(dHC:CdTe)$_6$/Ca/Ag	dHC-NO_3	6	Ca/Ag	no
ITO/PEDOT:PSS/(dNiAl-LDH:CdTe)$_1$/Al	dNi/Al-LDH	1	Al	no

Notes: *: one alternated deposition *n* refers to one film of delaminated LDH and one film of CdTe.

<u>Devices based on delaminated clays, PDDA and thiol-capped CdTe nanoparticles.</u>

The solutions of the delaminated clays were prepared with a concentration of 1 mg/ml using ethanol as solvent. The solution of the PDDA was diluted to 1/40 in Milli-Q water. The solution of thiol-capped CdTe nanoparticles was diluted to 1/2 in Milli-Q water. A 0,40 µm pore diameter filter was connected to a syringe in order to discard any agglomeration. The delaminated clays and PDDA solutions were deposited using this syringe.

The spin-coating parameters for this family of devices are summarized next:

- Delaminated clay films: 1500 rpm for 60 s.
- PDDA films: 3000 rpm for 60 s.
- CdTe films: 3000 rpm for 30 s.

PDDA, which is a cationic polyelectrolyte, was sandwiched between the delaminated clay film and the CdTe film because of the negative charge of these delaminated clays and thiol-capped CdTe nanoparticles and to improve the interaction.

In Table 6.3 the parameters for each device are summarized:

Table 6.3. Parameters for devices based on delaminated clays.

Architecture	inorganicmatrix	# alternateddepositions (*n*)*	cathode	post-annealing
ITO/PEDOT:PSS/(dSAP:PDDA:CdTe)$_5$/Al	dSAP	5	Al	no
ITO/PEDOT:PSS/(dSAP:PDDA:CdTe)$_6$/Al	dSAP	6	Al	no
ITO/PEDOT:PSS/(dHEC:PDDA:CdTe)$_2$/Ca/Ag	dHEC	2	Ca/Ag	no
ITO/PEDOT:PSS/(dSAP:PDDA:CdTe)$_2$/Ca/Ag	dSAP	5	Ca/Ag	no

Notes: *: one alternated deposition *n* refers to one film of delaminated clay, one film of PDDA and one film of CdTe.

Figure 6.5 shows a schematic representation of a device assembled in this work.

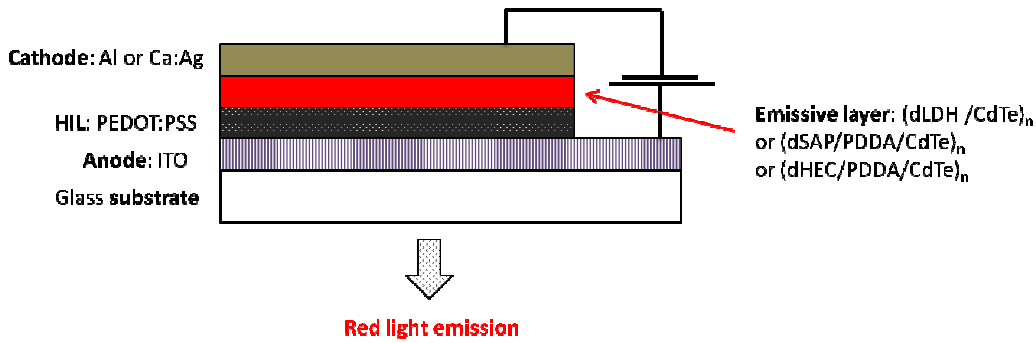

Figure 6.5 Schematic representation of a device assembled in this work.

c) Cathode deposition.

Once the emissive layers were deposited, the glass substrates were transferred to a glove box where the evaporation chamber was located. In this work, two metals were used for cathode evaporation: Al and Ca/Ag. The thickness of the cathode was 100 nm for Al and 20:40 nm for Ca/Ag. The evaporation started only when the pressure was less than $1 \cdot 10^{-6}$ torr. Once the cathode was deposited, the devices where stored inside the glove box.

Figure 6.6 shows a device after cathode deposition, located inside the glove box.

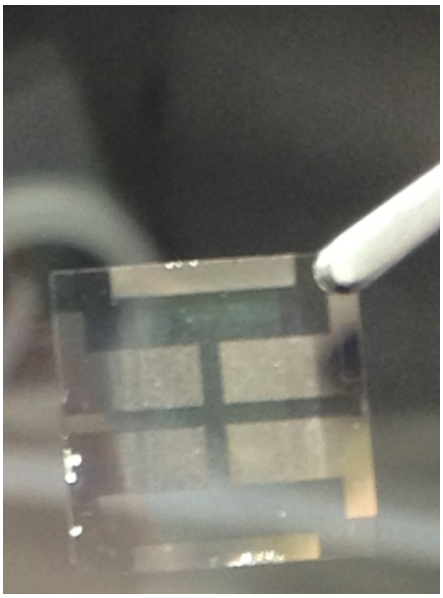

Figure 6.6 QDLED device.

6.4 Results and discussion.

6.4.1 Characterization of the thiol-capped CdTe nanoparticles.

The CdTe nanoparticles were characterized by TEM microscopy and by optic measurements. In figure 6.7 it is possible to observe a TEM micrography with the nanoparticles.

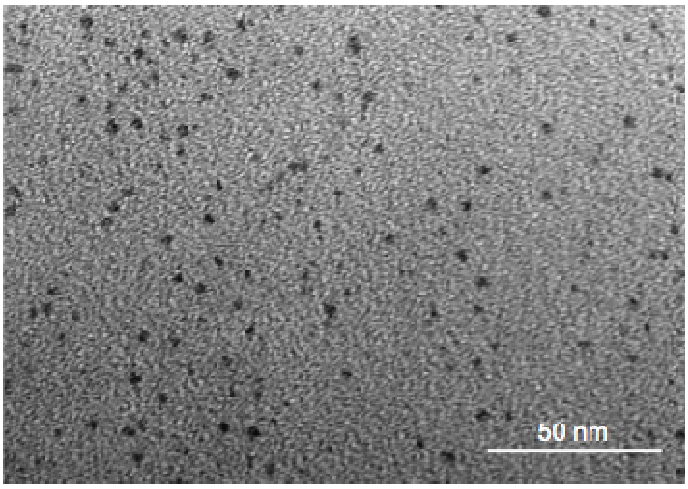

Figure 6.7. TEM micrograph of the thiol-capped CdTe nanoparticles.

The nanoparticles appeared non-aggregated and with a morphology corresponding to the size-dependent properties for red thiol-capped CdTe nanoparticles. Figure 6.8 shows an histogram graph of the size distribution of the nanoparticles. In general, values ranged from 2 to 5 nm.

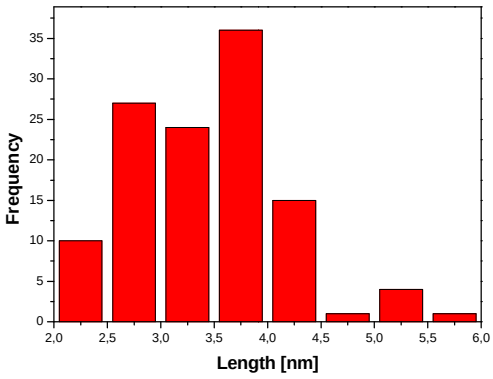

Figure 6.8. Histogram for the thiol-capped CdTe nanoparticles size.

The optic emission and absorption spectra were recorded for the thiol-capped CdTe nanoparticles, shown in figure 6.9.

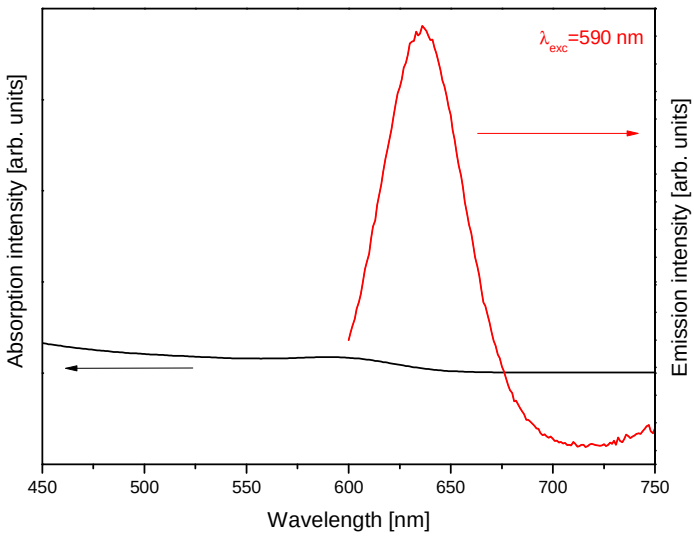

Figure 6.9. Optic characterization of the thiol-capped CdTe nanoparticles. In red, emission spectra, in black absorption spectra.

The emission spectra was centered at 634 nm and the absorption at 570 nm, in well agreement for the emission spectra expected in the red region of the visible spectrum.

6.4.2 Hybrid materials with potential luminescent properties.

CaAl layered double hydroxide with thiol-capped CdTe nanoparticles.

A hybrid CaAl layered double hydroxide was synthesized with thiol-capped CdTe nanoparticles. In figure 6.10 the diffractogram is shown.

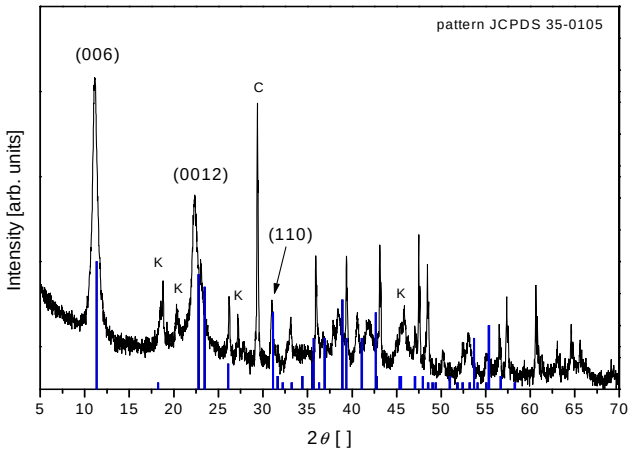

Figure 6.10. XRPD of sample hHC-Cl.

It was possible to identify hydrocalumite phase (JCPDS file 035-0105) which belongs to the trigonal group with space group R3c. Sample hHC-Cl presented cell parameters (a= 5,76 Å and c= 47,4 Å). In the diffractogram, it was possible to observe the calcite phase (JCPDS file 072-1652). The presence of calcite could be associated to some incorporation of CO_2 during the synthesis, even though an inert atmosphere was kept during the process. Katoite phase was identified (JCPDS file 074-3032) as well in the diffractogram. The presence of katoite could be associated to different rates of precipitation. The highest intensities for the peaks that correspond to the stacking direction (006) and (0012) are in agreement with the LDH structure. The (006) reflection appeared at values of 2*θ,* which corresponds to the expected value for chloride CaAl layered double hydroxide. The basal distance is in agreement with size for the chloride anion (7,95 Å). Because of the 2*θ* values for (006) reflection and the basal distance calculated from this reflection we may suggest that thiol-capped CdTe nanoparticles were not incorporated in the interlayer region, but were adsorbed in the external layers of the LDH.

Sample hHC-Cl presents less stacking degree along the ***c*** axis (21,82 nm) compared to the other hydrocalumite-type materials synthesized in this thesis work. In general, sample hHC-Cl shows broad peaks, exhibiting less crystallinity, compared to other chloride hydrocalumites (Chapter 4), which could also appear as a consequence of the aging treatment for this sample (at 323 K for 24 h using conventional heating). As seen previously in this chapter, aging treatments with microwave radiation as a heating source increase the crystallinities of the aged materials.

A representative FT-IR spectrum is showed in figure 6.11 for sample hHC-Cl. The figure is divided in two regions, between 2500 and 4000 cm^{-1} and between 1250 and 1600 cm^{-1}. In the region between 2500 and 4000 cm^{-1} it is possible to observe two bands at 3480 and at 3630 cm^{-1} that are ascribed to the OH-stretching (CaO-H). In the region between 1250 and 1600 cm^{-1} it is possible to observe a small band at around 1380 cm^{-1}, which can be associated to the stretching vibration (COO^-) of the thiol ligands of the nanoparticles [Ontam *et al.* 2012]. Therefore, we can suggest the presence of low amounts of thiol-capped CdTe nanoparticles in the synthesized material.

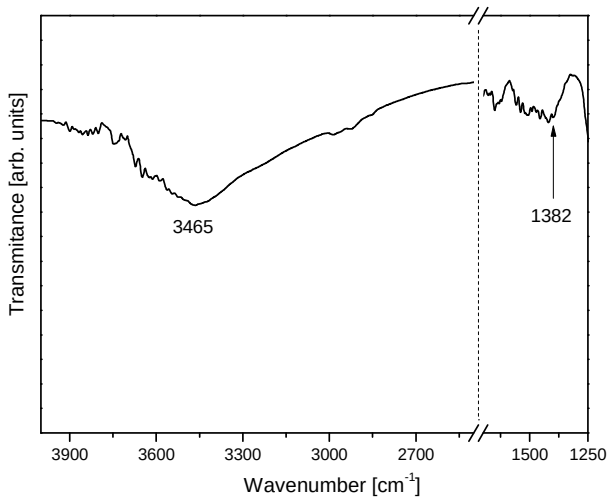

Figure 6.11. FT-IR spectrum of two regions of sample hHC-Cl.

A TEM micrograph of the hybrid CaAl layered double hydroxide is shown in figure 6.12. In general, it is possible to observe differentiated and aggregated lamellae of sizes between 60 and 80 nm and well-oriented. The fact that thiol-capped CdTe nanoparticles were not identified in the TEM micrograph could be related to the disposition of the particles in the micrograph, where the edges are difficult to be observed. In order to test the luminescence properties, the emission spectra was recorded (Fig. 6.13).

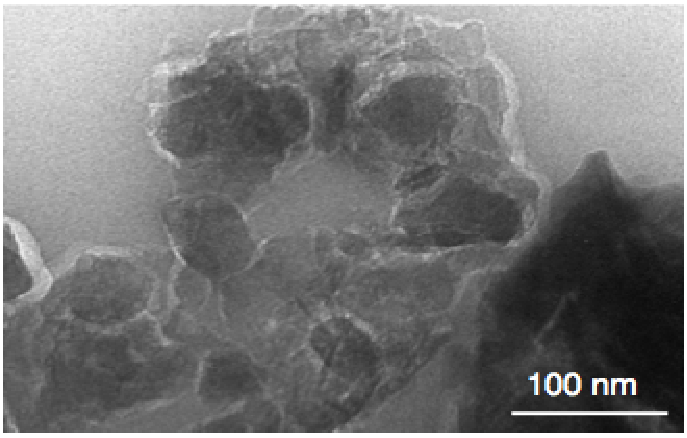

Figure 6.12. TEM micrograph of sample hHC-Cl.

It was possible to detect optic emission in the region of the red (in the visible spectrum), with a peak emission centered at 623 nm. Sample hHC-Cl presented the pick shifted 7 nm from the original emission peak of the nanoparticles (630 nm), which could be associated to some minor evolution of the size during the co-precipitation synthesis of the hybrid caAl layered double hydroxide or during the aging treatment. The presence of thiol-capped CdTe nanoparticles is also corroborated by the stretching band associated to the thiol group (COO^-) in the FT-IR spectrum (Fig. 6.11) at around 1382 cm^{-1}.

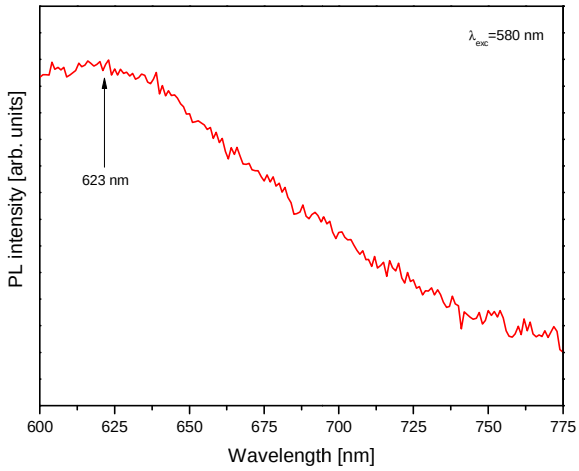

Figure 6.13. Photoluminescence spectra of sample hHC-Cl.

Hybrid saponites with thiol-capped Cdte nanoparticles.

The synthesis of oriented and delaminated saponites was performed following the process proposed in the literature [Trujillano *et al.* 2011, Gebretsadik *et al.* 2014]. The characterization of these samples was described in the corresponding papers. However, we characterized the samples used in this work by TEM microscopy. Oriented saponites, SAP, presented the expected lamellar morphology (Fig. 6.14). In general, the lamellae are oriented and quite aggregated. Their size is between 20 and 40 nm. Regarding delaminated saponites dSAP, its TEM micrograph (Fig. 6.15) shows the expected disorder of the lamellar particles, which were very thin and aggregated. The observed delamination was in agreement with the high value of BET specific surface area of this sample (461 m^2/g).

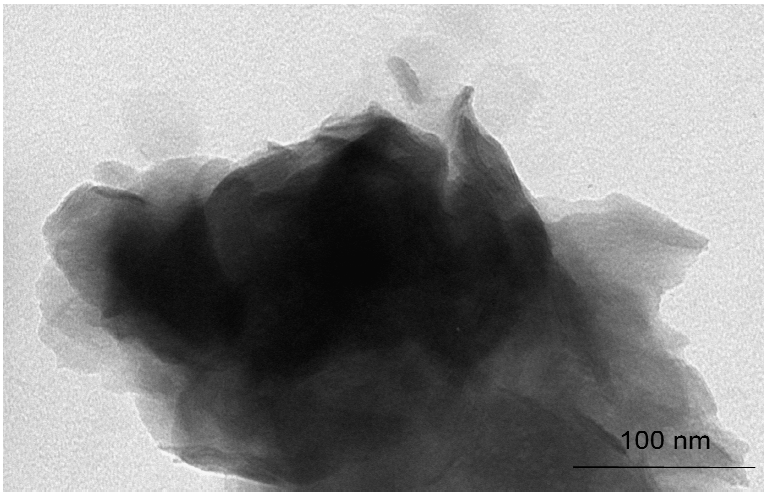

Figure 6.14. TEM micrographs of sample SAP at 300k.

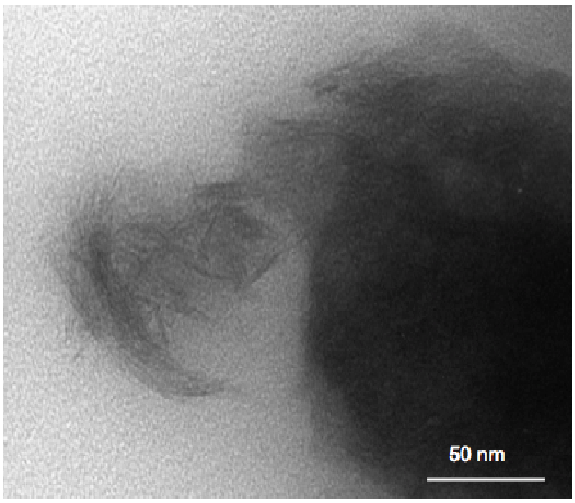

Figure 6.15. TEM micrograph of sample dSAP.

Regarding oriented saponites (SAP) with hexadecyltrimethylamonium bromide (HDTMA) and thiol-capped CdTe nanoparticles, two synthesis were performed with different concentrations of thiol-capped CdTe nanoparticles (with 40 and 2000 µl of the quantum dot solution).

In order to detect the presence of the cationic surfactant and the CdTe nanoparticles, FT-IR spectra were recorded (Fig. 6.16). The figure 6.16A)a shows the spectra for the saponite exchanged with HDTMA. The assignations of the bands for the saponite were done in accordance to other reports [Kloprogge *et al*. 2000]. The broad band around 3400 cm^{-1} is attributed to the O-H stretching; the band around 1000 cm^{-1} is assigned to O-Si-O stretching. The two bands at around 2850 cm^{-1} are attributed to the surfactant. These bands are present in the three spectra (Fig. 6.16A)a-c). Figure 6.16b and 6.16c show the spectra for the HDTMA-saponite with the thiol-capped CdTe nanoparticles. The band associated to the incorporation of the thiol-capped CdTe nanoparticles, attributed to the stretching vibration COO^- of the thiol ligands at 1382 cm^{-1} is difficult to see in sample that was treated with less quantity of thiol-capped CdTe nanoparticles (40 µl) (Fig. 6.16A)b). In contrast, in the IR spectrum this band appeared with a weak intensity in the sample that was treated with a larger quantity of CdTe nanoparticles (2000 µl) (Fig 6.16A)c and Fig 6.16B)). In order to further detect the presence of the nanoparticles, the emission spectra were recorded for these samples. A representative spectra is shown in figure 6.17.

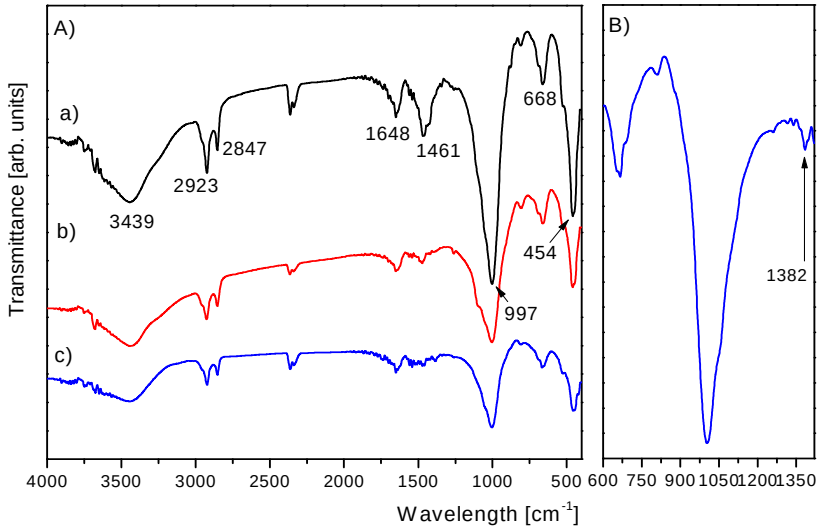

Figure 6.16. A) FT-IR spectra of samples a) SAP-HDTMA, b) SAP-HDTMA-CdTe(A) and c) SAP-HDTMA-CdTe(B). **B)** Detailed spectrum for sample SAP-HDTMA-CdTe(B).

The emission spectrum was recorded at an excitation wavelength of 580 nm and the emission peak was registered at 630 nm, which is in well agreement with the emission for these red thiol-capped CdTe nanoparticles.

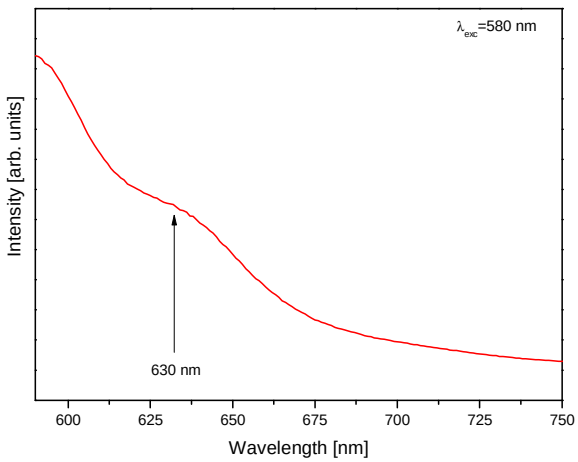

Figure 6.17. Emission spectrum of sample SAP-HDTMA-CdTe(A).

Another saponite, this time delaminated, was exchanged with the cationic polymer poly(diallyldimethylammonium chloride (PDDA) and thiol-capped CdTe nanoparticles. In order to detect the presence of the cationic surfactant and the CdTe nanoparticles, FT-IR spectrum was recorded (Fig. 6.18).

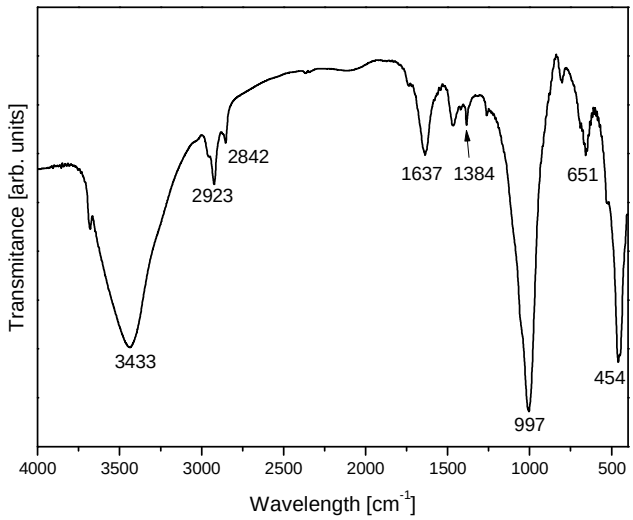

Figure 6.18. FT-IR spectrum of sample dSAP-PDDA-CdTe.

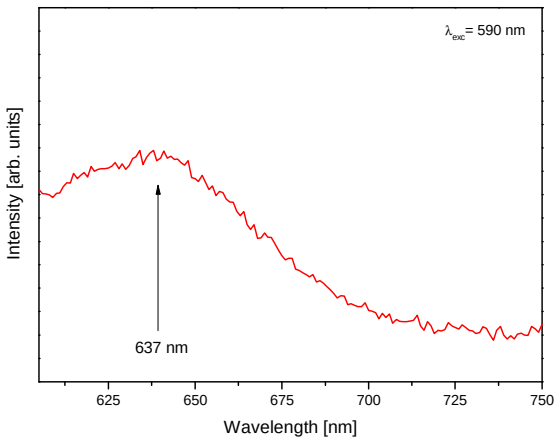

Figure 6.19. Emission spectrum of sample dSAP-PDDA-CdTe.

Because of the appearance of a band at around 1384 cm^{-1} it is possible to assign this band to the stretching vibration of the COO^- group that belongs to the ligands of the thiol-capped CdTe nanoparticles. To further detect their presence, the emission spectrum was recorded with an

excitation wavelength of 580 nm, shown in figure 6.19. The emission peak was registered at 637 nm. This shift from 630 to 637 nm could be a consequence of sample nanoparticle aggregation or evolution of the quantum dot size during the exchange procedure.

6.4.3 Inorganic matrixes for the emissive layer of the luminescent devices.

CaAl layered double hydroxide.

The synthesis and delamination of the nitrate CaAl-LDH, sample HC-NO_3, is explained in Chapter 4 of this thesis.

NiAl layered double hydroxide.

Regarding synthesis and delamination of NiAl layered double hydroxides, sample NiAl-LDH, figure 6.20 shows the XRPD diffractogram. The diffractogram was compared to the JPCDS file [015-0087] that corresponds to nickel aluminum oxide carbonate hydroxide hydrate with formula [$Ni_6Al_2(OH)_{16}(CO_3,OH)\cdot 4H_2O$] that belongs to the trigonal system with space group R-3m and cell parameters *a*=3.03Å and *c*=22.6Å. Because sample NiAl-LDH was synthesized in the presence of nitrate salts and absence of carbonate, the peaks that correspond to the stacking direction (00l) appeared shifted to lower angles. The diffractogram presents similarities to those that correspond to layered double hydroxides, where the peaks with the higher intensities belong to the stacking direction, in this case for reflections (003) and (006).

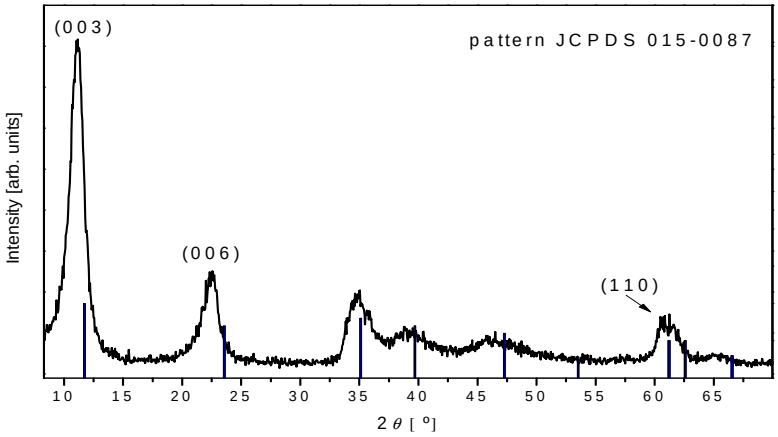

Figure 6.20. XRPD of sample NiAl-LDH.

The value for the FWHM for reflection (003) was 0,394 º and the value for crystallize size 26,54 nm along the stacking direction. This value is the lowest for a crystallite size compared to the

layered double hydroxides used in this thesis [Chapter 4]. In general, the peaks are broad, which could be attributed to the aging treatment used, by agitation and at RT. For the case of hydrocalumites and other layered double hydroxides the use of temperature and microwave irradiation showed improved crystallinities in those materials [Chapter 4, Benito *et al.* 2006]. The peaks between 2θ angle of 60 and 65 º are not well defined, thus, it is not possible to distinguish the peak for reflection (110), in the direction of the lamella, and extract information regarding its crystallite for that reflection.

The morphology of the lamellae was characterized by TEM microscopy (Fig 6.21). In figure 6.21a) it is possible to observe non-aggregated particles of two sizes, the smallest particles ranged between 10 and 15 nm and the larger particles ranged between 25 and 40 nm. In general, the majority of the particles ranged between 10 and 20 nm. The disposition of the lamellae is oriented. By the light colour of the smaller particles it is possible to observe that a few sheets are stacked in the ***c*** crystallographic direction. A detailed micrograph is shown in Fig. 6.21b), where the sizes ranged between 8 and 15 nm.

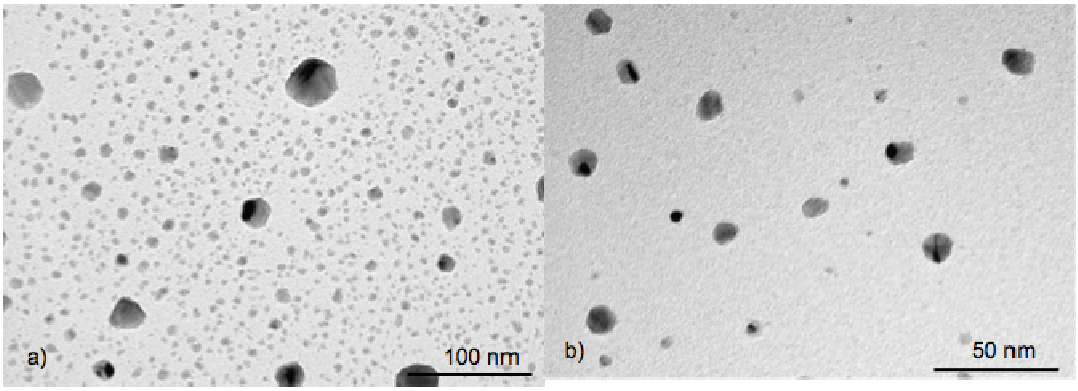

Figure 6.21. a) TEM micrograph of sample NiAl-LDH, b) detailed TEM micrograph of sample NiAl-LDH.

Delamination test was performed as explained in Chapter 4 of this thesis. For this particular sample, delamination was achieved by 5 cycles of 30 min of ultrasounds, in the presence of formamide. Delamination was fast-checked by the Tyndall effect (Fig. 6.22). A transparent colloidal suspension was obtained. It remained stable after 2 weeks, with no particle sedimentation. We could suggest that the swelling capacity for this sample together with the very small particle size favoured delamination process which remained stable for days.

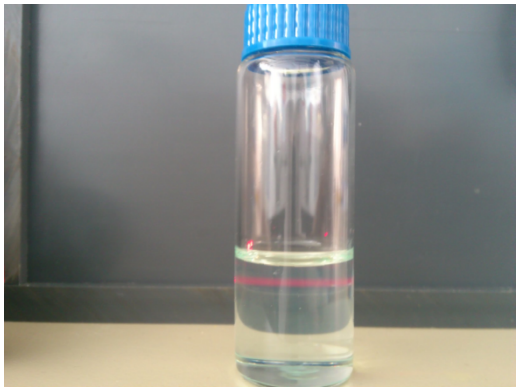

Figure 6.22 Tyndall effect checked for delaminated NiAl-LDH.

Delaminated hectorite.

The synthesis of the delaminated hectorite, sample dHEC, was in agreement with clay materials. The reflection (00l) which is associated to the stacking direction, was not observed, which could be associated to delamination. The surface are for this sample was of 599 m^2/g. The morphology was checked by TEM microscopy, shown in figure 6.23.

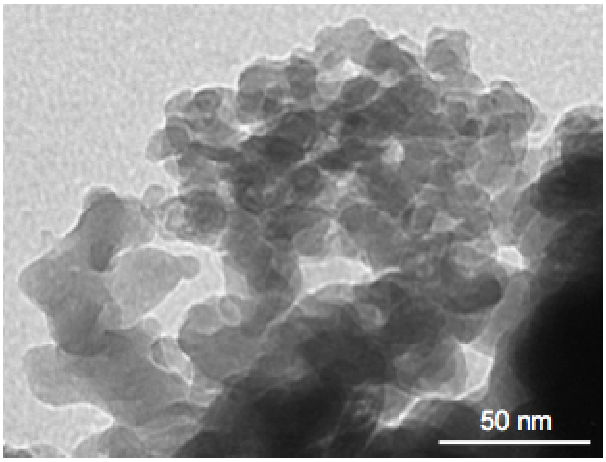

Figure 6.23.TEM micrograph of sample dHEC.

In general, it is possible to observe differentiated lamellae of sized that ranged from 20 to 35 nm. There was some degree of orientation in the particles. The results of characterization are in agreement with that described in the reference paper [Sánchez *et al.* 2013] used for the synthesis of this material.

6.4.4 Assembly of the luminescent devices.

Emissive layers of the devices.

Before the assembly of the device, the layers that form the architecture of the devices were characterized by ESEM microscopy in order to observe the disposition of the particles after spin-coating and to qualitatively determine the roughness. This characterization also contributed to the optimization of the spin-coating parameters that were finally used for the devices. These tests were performed on glass substrates, without the ITO patterned, where the layers where spin-coated.

Figure 6.24 shows three ESEM micrographs of a layer of delaminated hectorite spin-coated on a glass substrate.

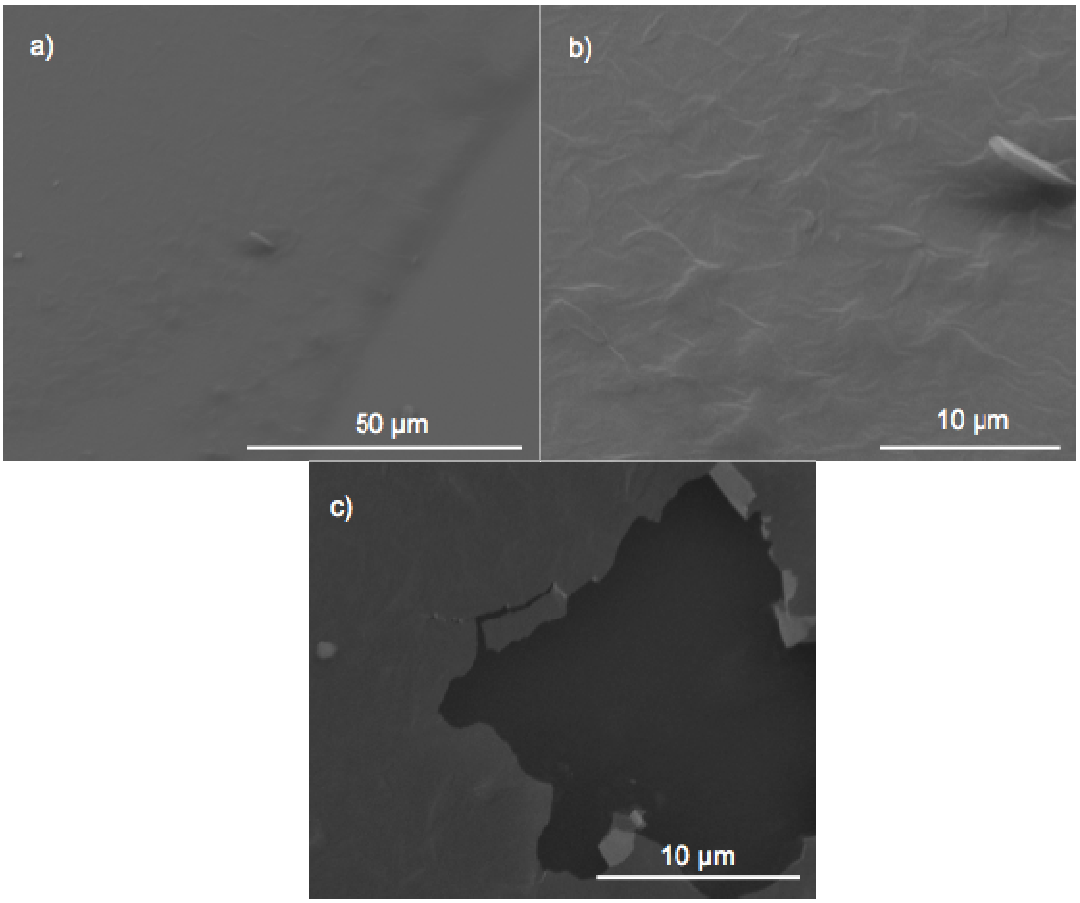

Figure 6.24. ESEM micrographs of a layer of delaminated hectorite spin-coated on a glass substrate, a) magnification 3000x, b) magnification 10000x and c) magnification 12000x.

From micrograph 6.24a it is possible to observe very little roughness in this layer. The particles of delaminated hectorite cover the surface of the glass substrate uniformly. There is no observation of empty spots which could be attributed to a non-successful spin-coating process. A magnification of this region is observed in micrograph 6.24b. It is possible to distinguish the presence of the delaminated hectorite particles. Again, the roughness is very little. In order to qualitatively determine the thickness of this layer, a part of the glass substrate was scratched (Fig. 6.24c). It is possible to observe in the upper part of the micrograph, right corner, that the layer is folded and the thickness is thinner than 50 nm.

Figure 6.25a shows an ESEM micrograph of a layer of delaminated saponite spin-coated on a glass substrate.

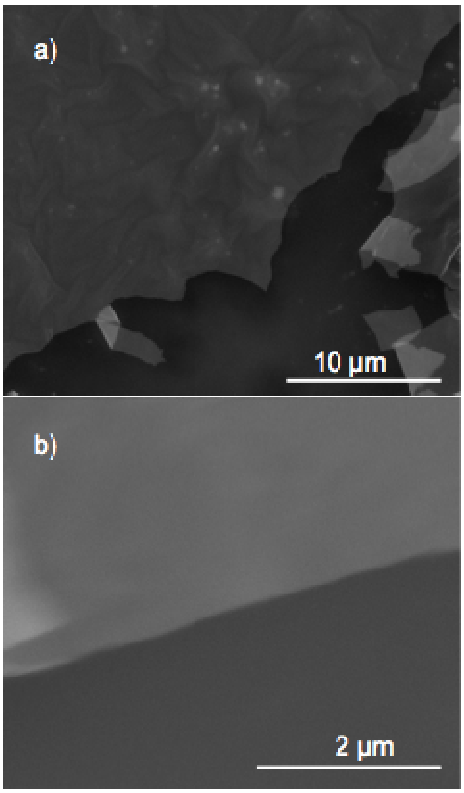

Figure 6.25. ESEM micrographs of a layer of delaminated saponite spin-coated on a glass substrate, a) magnification 10000x, b) magnification 60000x.

The layer appears scratched in the lower part of the micrograph so the layer thickness could be qualitatively determined. In general, it was possible to observe a uniform layer where no clear

spots were observed. The degree of roughness for this layer, compared to the delaminated hectorite layer, was higher, however, it can be attributed to a non-oriented disposition of some particles during the spin coating, presumably, that were aggregated prior to the moment of the deposition on the glass substrate. Thanks to the scratching area it was possible to determine, approximately, that the thickness of the layer was also less than 50 nm thick. It was possible to obtain a magnified micrograph of a folded part of the layer (Fig. 6.25b). The layer obtained was thin enough to be used for the assembly of the devices, as the thickness was determined to be between 20 and 30 nm thick.

In order to optimize the concentrations of the solutions used during the preparation of the emissive layers, ESEM measurements were done in order to determine the lateral thickness of alternated deposited layers. In figure 6.26 it is possible to observe the lateral size of a glass substrate where it was deposited an emissive layer n=1 (of delaminated saponite, PDDA and CdTe) (Fig. 6.26a) and the lateral size of a glass substrate where it was deposited an emissive layer n=2 (of delaminated saponite, PDDA and CdTe) (Fig. 6.26b). The thickness is larger than 200 nm, which is the maximum suggested for this kind of architecture [Bendall *et al.* 2010], as a result of the high concentration of the PDDA solution that in addition provided a certain degree of roughness to the total of the emissive layer. Therefore, the concentration was diluted to obtain layers with less thickness during the preparation of the devices.

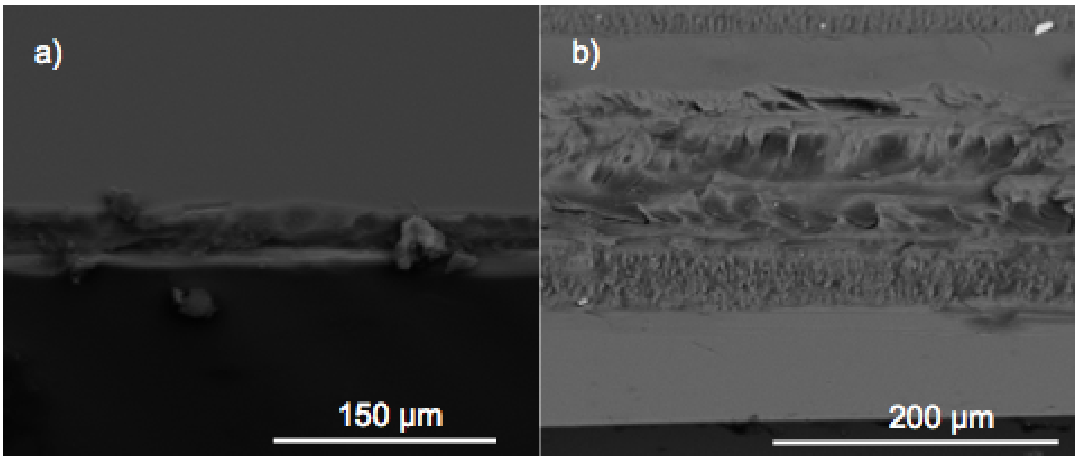

Figure 6.26. ESEM micrographs of the lateral of an emissive layer n=1 (of delaminated saponite, PDDA and CdTe) with magnification 2500x and b) lateral of an emissive layer n=2 (of delaminated saponite, PDDA and CdTe) with magnification of 800x.

Additionally, a representative emission spectrum was recorded for a glass substrate where a layer of delaminated saponite, PDDA and CdTe were spin coated (Fig. 6.27). The emission was recorded with an excitation wavelength of 580 nm. It is possible to observe a broad peak that corresponds to the emission of the CdTe nanoparticles centered at 610 nm. There is a shift of

approximately 20 nm to lower wavelengths. It is not clear if the shift is due to the matrix that surrounds the nanoparticles or to the annealing that was performed prior to the measure that could have affected the nanoparticles size.

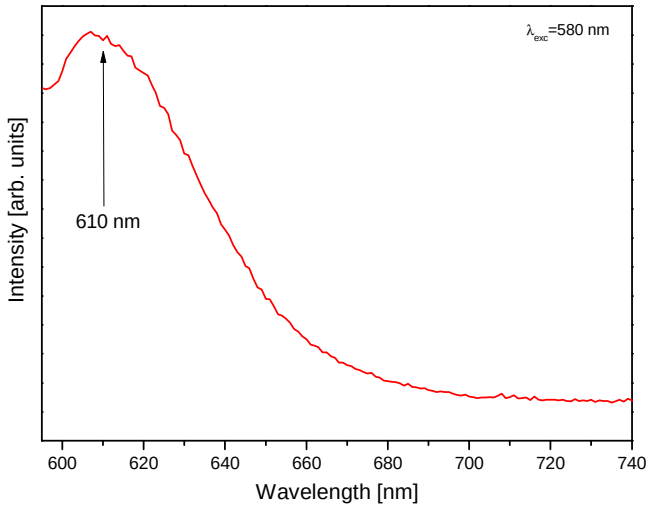

Figure 6.27. Emission spectra of a glass substrate where it was deposited by spin-coating: a layer of delaminated saponite, a layer of PDDA and a layer of CdTe nanoparticles.

Luminescent devices.

A representative picture of an illuminated pixel of a device is shown in Figure 6.28, which corresponds to the device with architecture ITO/PEDOT:PSS/(dHC:CdTe)$_6$/Ca/Ag.

After the devices were built, with the corresponding cathode evaporated (Al or Ca/Ag), they were electrically characterized to determine the I-V characteristics. From the slope of the plot log *V* vs. log *I* it is possible to obtain information about the main conduction mechanism in each region of the curve. The work function of the metals used as cathode are summarized in table 6.4.

Table 6.4. Work functions for the metals used as cathode.

Metal	Work function (eV)
Al	4,08
Ca	2,9
Ag	4,26-4,73[a]

[a]: The value depends on the crystalline face.

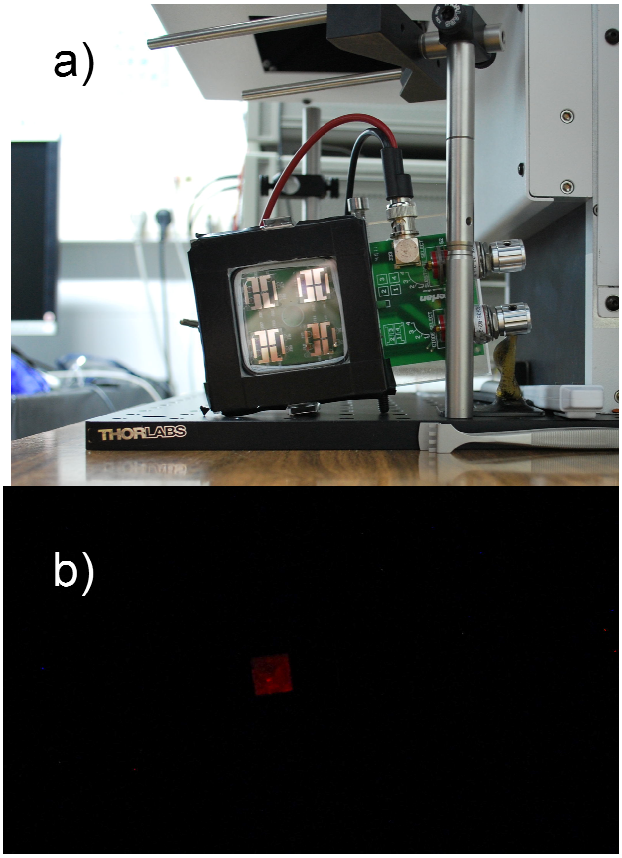

Figure 6.28. a) Device sample holder with 4 devices. b) Illuminated pixel.

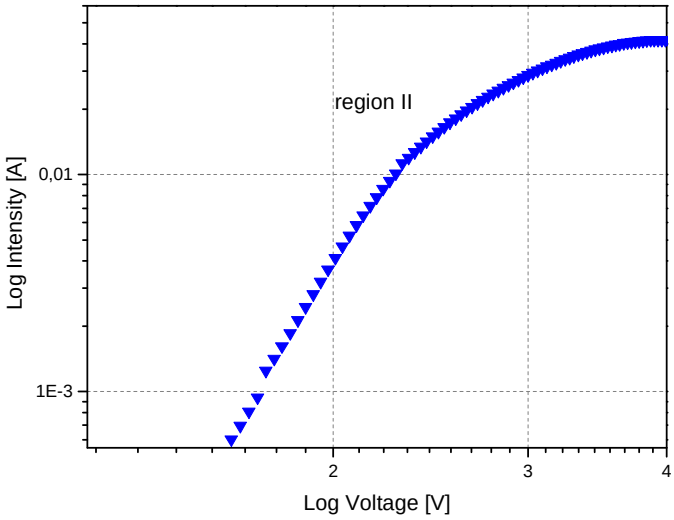

Figure 6.29 Log I-V characteristics for ITO/PEDOT:PSS/(dNiAl-LDH:CdTe)$_1$/Al.

Figure 6.29 shows the log I-V characteristics for a device based on ITO/PEDOT:PSS/(dNiAl-LDH:CdTe)$_1$/Al. Initially, the conduction is governed by ohmic region, at voltages lower than 1,5 V. From the turn-on voltage, around 1,8 V, the main conduction band observed for this device is SCLC. This means that the injected charge density exceeds the intrinsic free carrier density of the material [Joung *et al.*2010]. The nature of the inorganic films could explain this behavior, since amorphous regions there is a large concentrations of traps distributed in the energy band-gap [Wagle *et al.* 2000]. Devices based in delaminated takovite with n>1 alternated depositions did not yield light emission. This could be explained by a low conductivity of the delaminated takovite and an increase in the resistance of the active layer. A decrease in the luminance efficiency of the CdTe nanoparticles caused by the delaminated takovite could be discarded. The rate constant of this process is probably very low in these conditions (solid state of aggregation and especially, low values of takovite absorbance, which is localized at the nickel sites and origins the colour green).

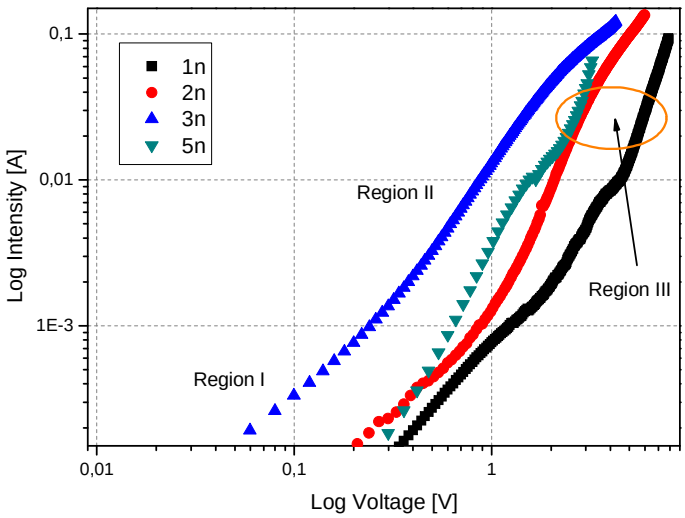

Figure 6.30. Log I-V characteristics for devices based on ITO/PEDOT:PSS/(dHC:CdTe)$_n$/Al.

Figure 6.30 shows the log I-V characteristics for devices based on delaminated HC-NO_3 and the metal Al as cathode. In general, the slopes remained similar independently of the number of alternated layers during the spin-coating. The first region for all the samples corresponds to ohmic conduction, which indicates that the current is directly proportional to the applied voltage [Wagle *et al.* 2000]. Then the main conduction mechanism is SCLC. The third region mainly is explained by exponential distribution of traps. The turn-on voltages were between 0,5 and 2,5 V. Interestingly, for the device with 3 alternated depositions, the turn-on voltage was earlier than the other samples. This behaviour could correspond to a better recombination in the emissive layer. In theory, as the thickness of the device grows, the value of electric field should be higher. However, it is difficult to find a correlation of the thickness of the devices with the current registered at voltages in the range 4-5 V, since the values are similar for devices with 2 and 5 alternated depositions. We may suggest some loss of homogeneity in the layers deposited for the device with 5 alternated depositions which would affect the recombination in the emissive layer. When exponential distribution of traps governs the conduction, the phenomenon can be associated to surface defects and structural disorders [Baidyaroy *et al.* 1972, Joung *et al.* 2010]. These defects could arise in the structures of the emissive layers as the temperature of the devices increase during the measurement of the I-V characteristics.

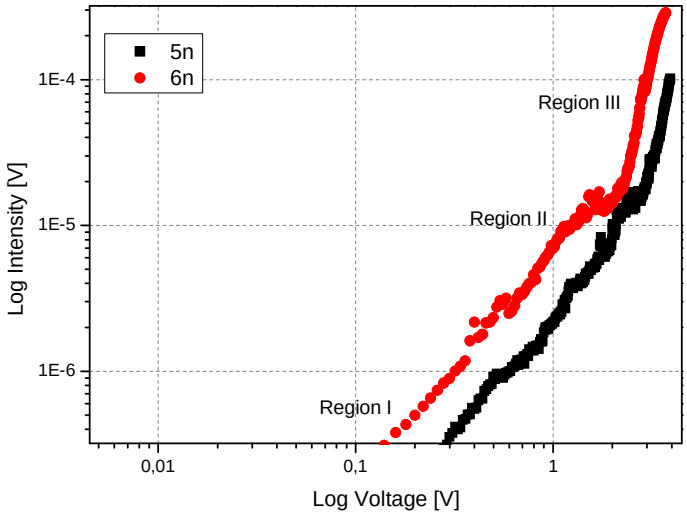

Figure 6.31. Log I-V characteristics for devices based on ITO/PEDOT:PSS/(dSAP:PDDA:CdTe)$_n$/Al.

Figure 6.31 shows the log I-V characteristics for devices based on delaminated saponites with PDDA as inorganic matrix and Al as the metal cathode. For these two samples, interestingly there are three differentiated regions, similarly to devices based on delaminated HC-NO_3. The conduction was governed by ohmic conduction at very low voltages, then there is a transition to SCLC conduction that derives to exponential distribution of traps at higher voltages: the slope of the plot is much larger than 2. We could suggest that the presence of the cationic polyelectrolite PDDA together with the inorganic matrix could favour a conduction where there are different states distribution. The slopes for the two devices are practically identical, the main difference is the number of alternated depositions, however, the influence of the thickness difference is very low since they differ only in one alternated deposition. This would explain that the device with 6 alternated depositions presents a slightly lower turn-on voltage than the device with 5 alternated depositions. The total number of films for devices based on delaminated clays is larger than for devices based on delaminated layered double hydroxides. As the number of film deposition increases, also the chances to lose homogeneity in the films. This would explain the different turn-on voltages for these devices. At higher voltages, disorder in the structure possibly arises and the conduction is governed by exponential distribution of traps.

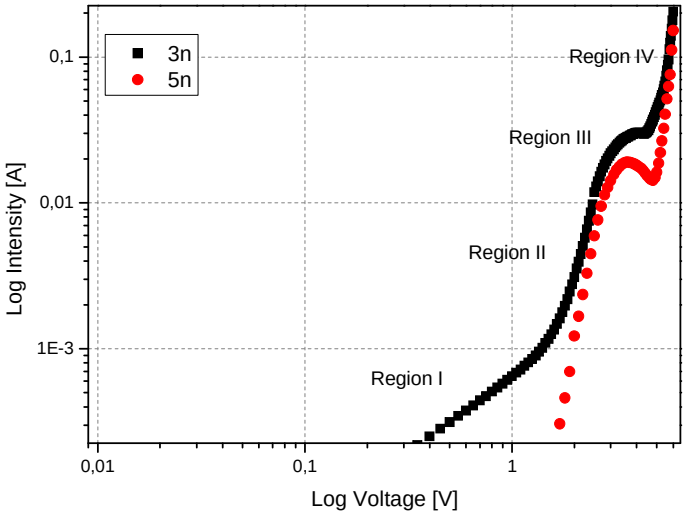

Figure 6.32. Log I-V characteristics for devices based on ITO/PEDOT:PSS/(dHC:CdTe)$_n$/Al with post-annealing.

Figure 6.32 shows the log I-V characteristics of two devices based on delaminated HC-NO_3 and Al as cathode. Additionally, annealing was performed after each deposition of the film of CdTe nanoparticles.

Interestingly, comparing devices based on delaminated HC-NO_3 with and without post-annealing (Fig. 6.30), it is possible to observe that introducing post-annealing changed dramatically the main conduction mechanism, from SCLC to mainly exponential distribution of traps, as seen by the two slopes at voltages higher than 1 V. Introducing post-annealing transformed the structure of the inorganic matrix and favoured this kind of conduction. Probably, it also affected the roughness of the layers, since it is possible to observe that the sample with 3 alternated depositions presents a first ohmic region and it disappeared for the device with 5 alternated depositions. This roughness/loss of homogeneity of the films after heating the device possible transformed the structure and so the main conduction that governs the device: the crystallinity of the inorganic matrix was modified and it could have affected the recombination process.

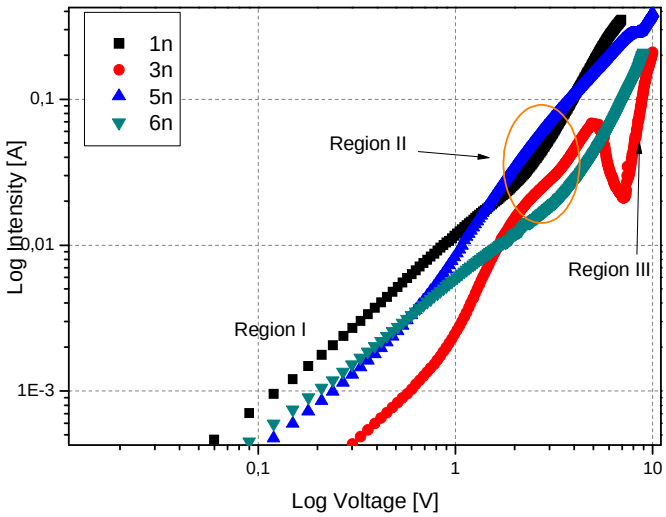

Figure 6.33. Log I-V characteristics for devices based on ITO/PEDOT:PSS/$(dHC:CdTe)_n$/Ca/Ag.

Figure 6.33 shows the log I-V characteristics for devices based on delaminated HC-NO_3 and Ca/Ag as metals. The slopes remained quite similar for these devices. Firstly, they all exhibit ohmic behaviour, which indicates that the current is directly proportional to the applied voltage. Then the main conduction mechanism is SCLC, as expected for these kind of devices. It is difficult to define a correlation with the thickness of the devices, since the currents for devices with 1 and 5 alternated depositions remain very similar in their I-V characteristics, in contrast devices with 3 and 6 alternated depositions presented values of lower currents at the same given voltages, from 4 V. The device based on 3 alternated depositions presented a final region of exponential distribution of traps, which could be explained by a different homogeneity of the layers that compose this device, observing that the device with more alternated depositions (6) does not present this mechanism behaviour. In general, we can suggest that the change in the metal of the cathode favoured the injection of electrons and it affected the main conduction mechanisms that govern these devices (SCLC). This is explained because the work function of Ca is lower than that of Al (Table 6.4). The bilayer Ca/Ag offers high transparency and low resistivity. The layer of Ca, which has a low work-function than Al, makes an easy injection of electrons; the Ag layer improves the lateral electrical conductance of the cathode [Lee *et al.* 2014]. Therefore in devices with Ca/Ag as cathode we could suggest that the carriers could be controlled by electrons rather than by holes.

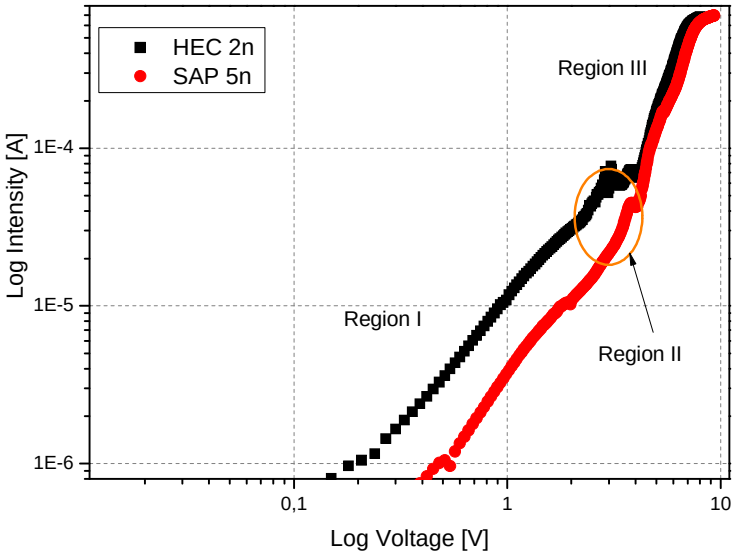

Figure 6.34. Log I-V characteristics for devices based on ITO/PEDOT:PSS/(dSAP:PDDA:CdTe)$_5$/Ca/Ag and ITO/PEDOT:PSS/(dHEC:PDDA:CdTe)$_2$/Ca/Ag.

Figure 6.34 shows the log I-V characteristics for a delaminated hectorite and saponite with Ca/Ag metal cathode. Comparing the behaviour of delaminated clays with Ca/Ag as cathode to those with Al as cathode (Fig. 6.31), it is possible to observe that, because the work function of the metal changes, so the voltage at which the behaviour changes to exponential distribution of traps. For devices with Ca/Ag as cathode this change is done at values of 4 V, approximately, whereas this change was observed before (2 V) for delaminated clays with Al as cathode. Similarly to devices plotted in figure 6.33, with the use of Ca/Ag as cathode, the main conduction mechanism that governs these devices from turn-on voltage is SCLC. It is very difficult to correlate the thickness of these two devices (delaminated hectorite and delaminated saponite) with the I-V characteristics, since the slopes remain quite similar and the differences of current are not important. Actually, the plots overlap from current values of 4V. This could be associated to the recombination process that occurred in the emissive layer. It could have appeared some loss of efficiency in the recombination.

In table 6.5, the different conduction mechanisms are summarized for the devices plotted in figures 6.29-6.33.

Table 6.5. Summary of conduction mechanisms' regions in the different I-V figures.

Figure	Region I	slope Region I	Region II	slope Region II	Region III	slope Region III	Region IV	slope Region IV
6.29	Ohmic	m~1	SCLC	m~2	-	-	-	-
6.30	Ohmic	m~1	SCLC	m~2	EDT-SCLC	m>2	-	-
6.31	Ohmic	m~1	SCLC	m~2	EDT-SCLC	m>2	-	-
6.32	Ohmic	m~1	EDT-SCLC	m>2	SCLC	m~2	EDT-SCLC	m>2
6.33	Ohmic	m~1	SCLC	m~2	EDT-SCLC	m>2	-	-
6.34	Ohmic	m~1	SCLC	m~2	EDT-SCLC	m>2	-	-

SCLC: space charge limited conduction, EDT: exponential distribution of traps. m: slope of the log *V*-log *I* graph ($I=kV^m$)

In order to characterize the emission of these devices, several attempts were made to record the emission spectra and the luminescence. Unfortunately, the fiber spectrophotometer and the luminancemeter instruments could not detect emission because the emission times of the devices were short.

6.5 Conclusions.

In this chapter, several hybrid materials with thiol-capped CdTe nanoparticles were synthesized and characterized (based on layered double hydroxides or clays) in order to have luminescent properties. It was possible to detect optic emission in the red region of the visible spectrum. The thiol-capped CdTe nanoparticles did not change significantly their range of optic emission which implied that they were disposed in the inorganic matrix without important changes on their sizes. Therefore, we could suggest the use of these hybrids materials for photonic applications.

A NiAl layered double hydroxide (NiAl-LDH) was synthesized with small particle sizes, in the range of 10-20 nm and later delaminated. The fact that its particle size was small, together with its swelling capacity, favoured the delamination process. In delaminated form NiAl-LDH was used as inorganic matrix to embed thethiol-capped CdTe nanoparticles in the emissive layer of the light-emitting diodes based on quantum dots (QD-LEDs).

Inorganic matrixes composed by several delaminated CaAl layered double hydroxides (CaAl-LDHs) and delaminated clays (hectorites and saponites) were also used for the assembly of QD-LEDs devices. These devices, together with those based on NiAl-LDH films, were electrically characterized. The parameters of spin-coating and concentration of the different solutions used were optimized in order to have the correct thickness to allow electron-hole recombination in the emissive later. These devices were based on two types: films of delaminated layered double hydroxides (CaAl-LDH and NiAl-LDH) and thiol-capped CdTe nanoparticles and films of delaminated clays (saponites and hectorites), PDDA and thiol-capped CdTe nanoparticles. It was possible to detect red light emission from all these devices.

In the assembly of the devices four parameters were studied: i) the type of inorganic matrix, ii) the number of alternated depositions, iii) the metal cathode evaporated (Al or Ca/Ag) and iv) the use or not of post-annealing. Regarding the number of alternated depositions, when the number was larger than 5, it was difficult to observe differences in their electrical behaviour. Comparing the type of metal used for cathode deposition, because of their different work function of the metals (Al and Ca/Ag), the use of Ca/Al supposed that the change from SCLC to EDT-SCLC appeared at higher voltages. In general, at higher voltages, the conduction was exponential distribution of traps for all devices. Comparing the use of post-annealing in some devices, it was possible to observe that the morphology and crystallinity of the inorganic matrixes could have changed and it led to a change in the conduction mechanism.

In general, the electrical characteristics of these devices were similar, with conductions mechanisms that alternated SCLC (space charge limited conduction) and trap free distribution, expected for these kind of devices. The switch from SCLC to trap-free conduction could be explained by the presence of defects and structural disorders.

References for chapter 6

[Anikeeva *et al.*2008] Anikeeva P. O., Madigan C. F., Halpert J. E., Bawendi M. G. and Bulović V. **2008**, *Electronic and excitonic processes in light-emitting devices based on organicmaterials and colloidal quantum dots*, *Phys. Rev. B*, 78, 085434.

[Baidyaroy *et al.* 1972] Baidyaroy S. and Mark P. **1972**, *Analytical and experimental investigation of the effects of oxygen chemisorptions on the electrical conductivity of CdS*, Surf. Sci., 30, 53-68.

[Belova *et al.* 2009] Belova V., Möhwald H., Shchukin D. G. **2009**, *Ultrasonic intercalation of gold nanoparticles into a clay matrix in the presence of surface-active materials*. *Part II: Negative sodium dodecylsulfate and positive cetryltrimethylammonium bromide*, J. Phys. Chem. C., 113, 6751-6760.

[Bendall *et al.* 2010] Bendall J. S., Paderi M., Ghigliotti F., Li Pira, N., Lambertini V., Lesnyak V., Gaponik N., Visimberga G., Eychmüller A., Sotomayor Torres C. M., Welland M. E, Gieck C. and Marchese L. **2010**, *Layer-by-layer all-inorganic quantum-dot-based LEDs: a simple procedure with robust performance*, Adv. Funct. Mater., 20, 3298-3302.

[Benito *et al.* 2006] Benito P., Labajos F. M., Rocha J. and Rives V. **2006**, *Influence of microwave radiation on the textural properties of layered double hydroxides*, Micropor. Mesopor.Mater., 94, 148-158.

[Bisio *et al.* 2008] Bisio C., Gatti G., Boccaleri E., Marchese L., Superti G. B., Pastore H. O. and Thommes M. **2008**, *Understanding physico-chemical properties of saponite synthetic clays*, Micropor. Mesopor. Mater., 107, 90-101.

[Burrows *et al.* 1994] Burrows P. E., Bulović V., Forrest S. R., Sapochak L. S. and Mccarty D. M. **1994**, *Reliability and degradation of organic light emitting devices*, Appl. Phys. Lett., 65, 2922–2924.

[Cao 2012] Cao Y-C. **2012**, *Preparation of thermally stable well-dispersed water-soluble CdTe quantum dots in montmorillonite clay host media*, J. Colloid Interface Sci., 368, 139-143.

[Carlos *et al*. 2009] Carlos L. D., Ferreira R. A. S, de Zea Bermudez V. and Ribeiro S. J. L. **2009**, *Lanthanide-containing light-emitting organic-inorganic hybrids: a bet on the future*, Adv. Mater., 21, 509-534.

[Caruge *et al.*2008] Caruge J. M., Halpert J. E., Wood V., Bulović V. and Bawendi M. G. **2008**, *Colloidal quantum-dot light-emitting diodes with metal-oxide charge transport layers*, Nature Photon., 2, 247–250.

[Chen *et al.* 2013] Chen C., Yee L. K., Gong H., Zhang Y. and Xu R. **2013**, *A facile synthesis of strong near infrared fluorescent layered double hydroxide nanovehicles with an anticancer drug for tumor optical imaging and therapy*, Nanoscale, 5, 4314-4320.

[Chen *et al.* 2014] Chen J., Zhao D., Li C., Xu F., Lei W., Sun L., Nathan A. and Sun X. W. **2014**, *All solution-processed stable white quantum dot light-emitting diodes with hybrid ZnO@TiO_2 as blue emitters*, Sci. Rep., 4, 4085.

[Chiu 2014] Chiu F. C. **2014**, *A review on conduction mechanisms in dielectric films*, Adv. Mater. Sci. Eng., 578168.

[Cho *et al.* 2012] Cho S. H., Sung J., Hwang I., Kim R. H, Coi Y. S., Jo S. S, Lee, T. W and Park C. **2012**, *High performance AC electroluminescence from colloidal quantum dot hybrids*, Adv. Mater. 24, 4540–4546.

[Cho *et al.* 2013] ChoS., Kwag J., Jeong S., Baek, Y. and Kim S. **2013**, *Highly fluorescent and stable quantum dot-polymer layered double hydroxide composites*, Chem. Mater., 25, 1071-1077.

[Cho *et al.* 2013b] Cho S., Jung S., Jeong S., Bang J., Park J., Park Y. and Kim S. **2013**, *Strategy for synthesizing quantum dot-layered double hydroxide nanocomposites and their enhanced photoluminescence and photostability*, Langmuir, 29, 441-447.

[Coe *et al*. 2002] Coe S., Woo W-K., Bawendl M. and Bulović V. **2002**, *Electroluminescence from single monolayers of nanocrystals in molecular organic devices*, *Nature*, 420, 800-803.

[Colvin *et al.* 1994] Colvin V. L., Schlamp M. C. and Alivisatos A. P.**1994**, *Light-emitting diodes made from cadmium selenide nanocrystals and a semiconducting polymer*, *Nature*, 370, 354-357.

[Ekimov *et al.* 1981] Ekimov A. and Onushchenko A. A. **1981**, *Quantum size effect in three-dimensional microscopic semiconductor crystalls*, *JETP Lett*., 34, 345-349.

[Ferreira *et al.* 2013] Ferreira A. U. C., Poli A. L., Gessner F., Neumann M. G. and Schmitt Cavalheiro C. C. **2013**, *Interaction of Auramine O with montmorillonite clays*, J. Lumin. 136, 63-67.

[Gao *et al.* 2011] Gao F, Lv C., Han J., Li X., Wang Q., Zhang J., Chen C., Li Q., Sun X., Zheng J., Bao L. and Li X. **2011**, *CdTe-Montmorillonite nanocomposites: control synthesis, UV radiation-dependent photoluminescence, and enhanced latent fingerprint detection*, J. Phys. Chem. C., 115, 21574-21583.

[Gaponik *et al.* 2010] Gaponik N. and Rogach A. L. **2010**, Thiol-capped CdTe nanocystals: progress and perspectives of the related research fields, Phys. Chem. Chem. Phys., 12, 8685-8693.

[Gebretsadik *et al.* 2014] Gebretsadik F. B., Salagre P. and Cesteros, Y. **2014**, *Use of polymer as template in microwave synthesis of saponite. Study of several factors of influence*, Appl. Clay Sci., 87, 170-178.

[Joung *et al.*2010] Joung D., Chunder A., Zhai L. and Khondaker S. I. **2010**, *Space charge limited conduction with exponential trap distribution in reduced graphene oxide sheets*, Appl. Phys. Lett., 97, 093105.

[Kamino *et al*. 2013] Kamino B. A. and Bender T. P. **2013**, *The use of siloxanes, silsesquioxanes, and silicones in organic semiconducting materials*, Chem. Soc. Rev., 42, 5119-5130.

[Khaorapapong *et al.* 2010] Khaorapapong N., Ontam A. and Ogawa M. **2010**, *Formation of ZnS and CdS in the interlayer spaces of montmorillonite*, Appl. Clay Sci., 50, 19-24.

[Kim *et al.*2011] Kim T-H., Cho K-S., Lee E. K.,Lee S. J., Chae J.,Kim J. W.,Kim D. H.,Kwon J. Y. , Amaratunga G.,Lee S. Y.,Choi B. L., Kuk Y., Kim J. K. and Kim K. **2011**, *Full-colour quantum dot displays fabricated by transfer printing*, Nature Photon., 5, 176-182.

[Kloprogge *et al.* 2000] Kloprogge J. T. and Frost R. L. **2000**, *The effect of synthesis temperature on the FT-Raman and FT-IR spectra of saponites*, Vib. Spectrosc., 23, 119-127.

[Lee *et al.* 2014] Lee C.-J. and Moon D.-G. **2014**, *Effect of Ag capping layer on the emission characteristics of transparent organic light-emitting devices with Ca/Ag double-layer cathodes*, Trans. Electr. Electron. Mater., 15, 45-48.

[Liang *et al*. 2012] Liang R., Xu S., Yan D., Shi W., Tian R., Yan H., Wei M., Evans D. G., Duan X. **2012**, *CdTe quantum dots/layered double hydroxide ultrathin films with multicolor light emission via layer-by-layer assembly*, Adv. Funct. Mater., 22, 4940-4948.

[Mashford *et al*. 2013] Mashford B. S, Stevenson M., Popovic Z., Hamilton C., Zhou Z., Breen C., Steckel J., Bulovic V., Bawendi M., Coe-Sullivan S. and Kazlas P. T. **2013**, *High-efficiency quantum-dot light emitting devices with enhanced charge injection*, Nature Photon., 7, 407-412.

[Molaei *et al.* 2012] Molaei M., Marandi M., Saievar-Iranizad E., Taghavinia N., Liu B., Sun, H. D. and Sun X. W. **2012**, *Near-white emitting QD-LED based on hydrophilic CdS nanocrystals*, J. Lumin., 132, 467-473.

[Morais *et al*. 1999] Morais T. D. d., Chaput F., Lahlil K. and Boilot J-P.**1999**, *Hybrid organic-inorganic light-emitting diodes*, Adv. Mater., 11, 107-112.

[Mueller *et al*. 2005] Mueller A. H., Petruska M. A., Achermann M., Werder D. J., Akhadov E. A., Koleske D. D., Hoffbauer M. A. and KlimovV. I. **2005**, *Multicolor light-emitting diodes based on semiconductor nanocrystals encapsulated in GaN charge injection layers*, NanoLett. 5, 1039–1044.

[Neumann *et al.* 2002] Neumann M. G., Gessner F., Schmitt C. C. and Sartori R. **2002**, *Influence of the layer charge and clay particle size on the interactions between the cationic dye methylene blue and clays in an aqueous suspension*, J. Colloid Interface Sci., 255, 254-259.

[Ontam *et al.* 2012] Ontam A., Khaorapapong N. and Ogawa M. **2012**, *Immobilization of cadmium telluride nanoparticles on the surface of hexadecyltrimethylammonium-montmorillonite*, J. Mater. Chem., 22, 20001-20007.

[Pandey *et al*. 2011] Pandey S. and Mishra S. B. **2011**, *Sol-gel derived organic-inorganic hybrid materials: synthesis, characterizations and applications*, J. Sol-Gel Sci. Technol., 59, 73-94.

[Qian *et al.*2011] Qian L., Zheng Y., Xue J. and Holloway P. H. **2011**, *Stable and efficient quantum- dot light-emitting diodes based on solution-processed multilayer structures*, Nature Photon., 5, 543–548.

[Sanchez *et al*. 2003] Sanchez C., Lebeau B., Chaput F. and Boilot J-P.**2003**, *Optical properties of functional hybrid organic-inorganic nanocomposites*, Adv. Mater., 15, 1969-1994.

[Sanchez *et al.* 2011] Sanchez C., Belleville P., Popall M. and Nicole L., **2011**, *Applications of advanced hybrid organic-inorganic nanomaterials: from laboratory to market*, Chem. Soc. Rev., 40, 696-753.

[Sánchez *et al.* 2013] Sánchez T., Salagre P. and Cesteros Y. **2013**, *Ultrasounds and microwave-assisted synthesis of mesoporous hectorites*, Micropor. Mesopor. Mater., 171, 24-34.

[Sanchez *et al.* 2014] Sanchez R. S., Binetti E., Torre J. A., Garcia-Belmonte G., Striccoli M. and Mora-Sero I. **2014**, *All solution processed low turn-on voltage near infrared LEDs based on core-shell PbS-CdS quantum dots with inverted device structure*, Nanoscale, 6, 8551-8555.

[Scott *et al*. 2001] Scott B. J., Wirnsberger G., Stucky G. D. **2001**, *Mesoporous and mesostructured materials for optical applications*, Chem. Mater., 13, 3140-3150.

[Stoica *et al.* 2012] Stoica G., Castelló Serrano I., Figuerola A., Ugarte I., Pacios R., Palomares E. **2012**, *Layered double hydroxides as carriers for quantum dots@silica nanospheres*, Nanoscale, 4, 5409-5419.

[Stouwdam *et al*. 2008] Stouwdam J. W. and Janssen R. A. J.**2008**, *Red, green, and blue quantum dot LEDs with solution processable ZnO nanocrystal electron injection layers*, J. Mater. Chem., 18, 1889-1894.

[Sze *et al.* 2007] Sze S. M. and Ng K. K. **2007**, *Physics of Semiconductor Devices*, 3rd ed. Wiley, New York.

[Trujillano *et al*. 2009] Trujillano R., Vicente M. A., Rives V., Korili S. A., Gil A., Ciuffi K. J. and Nassar E. J. **2009**, *Preparation, alumina-pillaring and oxidation catalytic performances of synthetic Ni-saponite*, Micropor. Mesopor. Mater., 117, 309-316.

[Trujillano *et al*. 2011] Trujillano R., Rico E., Vicente M.A., Rives V., Ciuffi K.J., Cestari A., Gil A. and Korili S.A. **2011**, *Rapid microwave-assisted synthesis of saponites and their use as oxidation catalysts*, Appl. Clay Sci., 53, 326–330.

[Wagle*et al.* 2000] Wagle S. and Shirodkar V. **2000**, *Space-Charge-Limited Conduction in thin film Al/$Sb_2Pb_1Se_7$/Al devices*, Braz. J. Phys., 30, 380-385.

[Wood *et al.* 2009] Wood V., Panzer M. J., Halpert J. E., Caruge J.-M., Bawendi M. G. and Bulović V. **2009**, *Selection of metal oxide charge transport layers for colloidal quantum dot LEDs*, ACS Nano 3, 3581–3586.

[Wood *et al*. 2010] Wood V., Panzer M. J., Caruge J.-M., Haplert J. E., Bawendi M. G. and Bulović V. **2010**, *Air-stable operation of transparent, colloidal quantum dot based LEDs with a unipolar device architecture*, NanoLett., 10, 24-29.

[Xie*et al.* 2011] Xie H-Y., Yang J., Yang S-Y., Wang C-F., Chen L. and Chen S.**2011**, *Facile fabrication of CdTe/montmorillonite nanocomposite films with stable photoluminescence properties*, Mater. Lett., 65, 1669-1671.

[Zhang *et al.* 2010] Zhang R., Hummelgård M. and Olin H. **2010**, *Simple synthesis of clay-gold nanocomposites with tunable color*, Langmuir, 26, 5823-5828.

CHAPTER 7

Conclusions

7. Conclusions of this thesis.

During this thesis book, conclusions have been exposed at the end of Chapters 4, 5 and 6. In this Chapter, the final conclusions are summarized.

Synthesis and characterization of CaAl layered double hydroxides & delamination and reconstruction studies.

- Several hydrocalumites, CaAl layered double hydroxides with chloride anion, where synthesized changing two variables, aging treatment by microwave irradiation or conventional heating, and using autoclaves or by refluxing, as recipients. It was found that aging with microwaves irradiation using autoclaves for 1 h at 453 K, decreased aging time and energy costs compared to conventional reported aging techniques (refluxing for 24 h at 333 K). Samples aged with microwave irradiation presented lower values of BET specific surface area and showed better crystallinities compared to samples aged by conventional heating.
- As observed by TEM characterization, samples aged using microwave irradiation presented large particle sizes with defined hexagonal shapes. For the most crystalline sample these values ranged 4000 nm.
- Two kinds of CaAl layered double hydroxides (CaAl-LDH) (with chloride and nitrate anions) were calcined and their reconstruction studied in the presence of different salts. It was possible to obtain the CaAl-LDH phase for all reconstructed samples. There was a preference for anion incorporation, as stated before, by the affinity of chloride vs. nitrate.
- Delamination studies were conducted using the use of ultrasounds and the use of mechanical stirring, with formamide as solvent, on CaAl-LDHs obtained from direct synthesis and reconstruction. The use of ultrasounds was more effective for the delamination of reconstructed CaAl-LDHs. For the case of as-synthesized CaAl-LDHs, the chloride CaAl-LDH could not be delaminated with either of the two techniques. This could be explained by the little swelling capacity for this sample together with the cohesive environment of the chloride anion in the interlayer region for this sample.
- A hybrid CaAl-LDH was reconstructed in the presence of thiol-capped CdTe nanoparticles. The CaAl-LDH phase was reconstructed, as observed by XRD, and the optical emission detected in the red region of the visible spectrum.

Glycerol etherification to short-chain polyglycerols using calcined MgAl and CaAl layered double hydroxides as catalysts.

- Calcined MgAl and CaAl layered double hydroxides (calcined MgAl-LDHs and CaAl-LDHs, respectively) where synthesized and characterized. These catalysts where tested for the etherification reaction of glycerol towards short-chain polyglycerols considering their basic

properties characterized by CO_2-TPD. In general, catalysts presented weak and medium basic sites. For the catalysts calcined at higher temperatures, strong basic sites were detected.

- The highest catalytic yield for a calcined MgAl-LDH (DG+TG 24%) was obtained for sample cHT-mw1(453). The highest catalytic yield for a calcined CaAl-LDH at 723 K (DG+TG 33%) was obtained for sample cHC-mw1(453). For samples calcined at higher temperatures, the catalytic yield for sample cHC-mw1(453)/923 was of 35% (DG+TG+TTG) and for sample cHC-mw1(453)/1073 was of 59% (DG+TG+TTG+PG).
- Correlating the acidic properties with the catalytic results, samples with high acidities led to high conversions and low selectivities to our products of interest. For the case of the basic properties, catalysts with strong sites led to higher selectivities towards our products of interest.
- Catalysts were stable after reaction since glycerolate phase was not detected, by XRD, in any case. Contribution of homogeneous catalysis was discarded.

Quantum dot-LED based on CdTe embedded in layered double hydroxides and clays.

- Several hybrid materials with thiol-capped CdTe nanoparticles were synthesized and characterized (based on layered double hydroxides or clays) in order to have luminescent properties. It was possible to detect optic emission in the red region of the visible spectrum. The thiol-capped CdTe nanoparticles did not change significantly their range of optic emission which implied that they were disposed in the inorganic matrix without important changes on their sizes. Therefore, we could suggest the use of these hybrids materials for photonic applications.
- A NiAl layered double hydroxide (NiAl-LDH) was synthesized with small particle sizes, in the range of 10-20 nm and later delaminated. The fact that its particle size was small, together with its swelling capacity, favoured the delamination process. In delaminated form NiAl-LDH was used as inorganic matrix to embed thethiol-capped CdTe nanoparticles in the emissive layer of the light-emitting diodes based on quantum dots (QD-LEDs).
- Inorganic matrixes composed by several delaminated CaAl layered double hydroxides (CaAl-LDHs) and delaminated clays (hectorites and saponites) were also used for the assembly of QD-LEDs devices. These devices, together with those based on NiAl-LDH films, were electrically characterized. The parameters of spin-coating and concentration of the different solutions used were optimized in order to have the correct thickness to allow electron-hole recombination in the emissive later. These devices were based on two types: films of delaminated layered double hydroxides (CaAl-LDH and NiAl-LDH) and thiol-capped CdTe nanoparticles and films of delaminated clays (saponites and hectorites), PDDA and thiol-capped CdTe nanoparticles. It was possible to detect red light emission from all these devices.
- In the assembly of the devices four parameters were studied: i) the type of inorganic matrix, ii) the number of alternated depositions, iii) the metal cathode evaporated (Al or Ca/Ag) and iv) the use or not of post-annealing. Regarding the number of alternated depositions, when the

number was larger than 5, it was difficult to observe differences in their electrical behaviour. Comparing the type of metal used for cathode deposition, because of their different work function of the metals (Al and Ca/Ag), the use of Ca/Al supposed that the change from SCLC to EDT-SCLC appeared at higher voltages. In general, at higher voltages, the conduction was exponential distribution of traps for all devices. Comparing the use of post-annealing in some devices, it was possible to observe that the morphology and crystallinity of the inorganic matrixes could have changed and it led to a change in the conduction mechanism.

- In general, the electrical characteristics of these devices were similar, with conductions mechanisms that alternated SCLC (space charge limited conduction) and trap free distribution, expected for these kind of devices. The switch from SCLC to trap-free conduction could be explained by the presence of defects and structural disorders.